International Journal of Optics

Photonics Applications in Biomedicine and Human Safety

Lead Guest Editor: Hsiao-Yi Lee
Guest Editors: Cheng-Mu Tsai, Tsair-Fwu Lee, Winston Chen, and Chun-Ming Huang

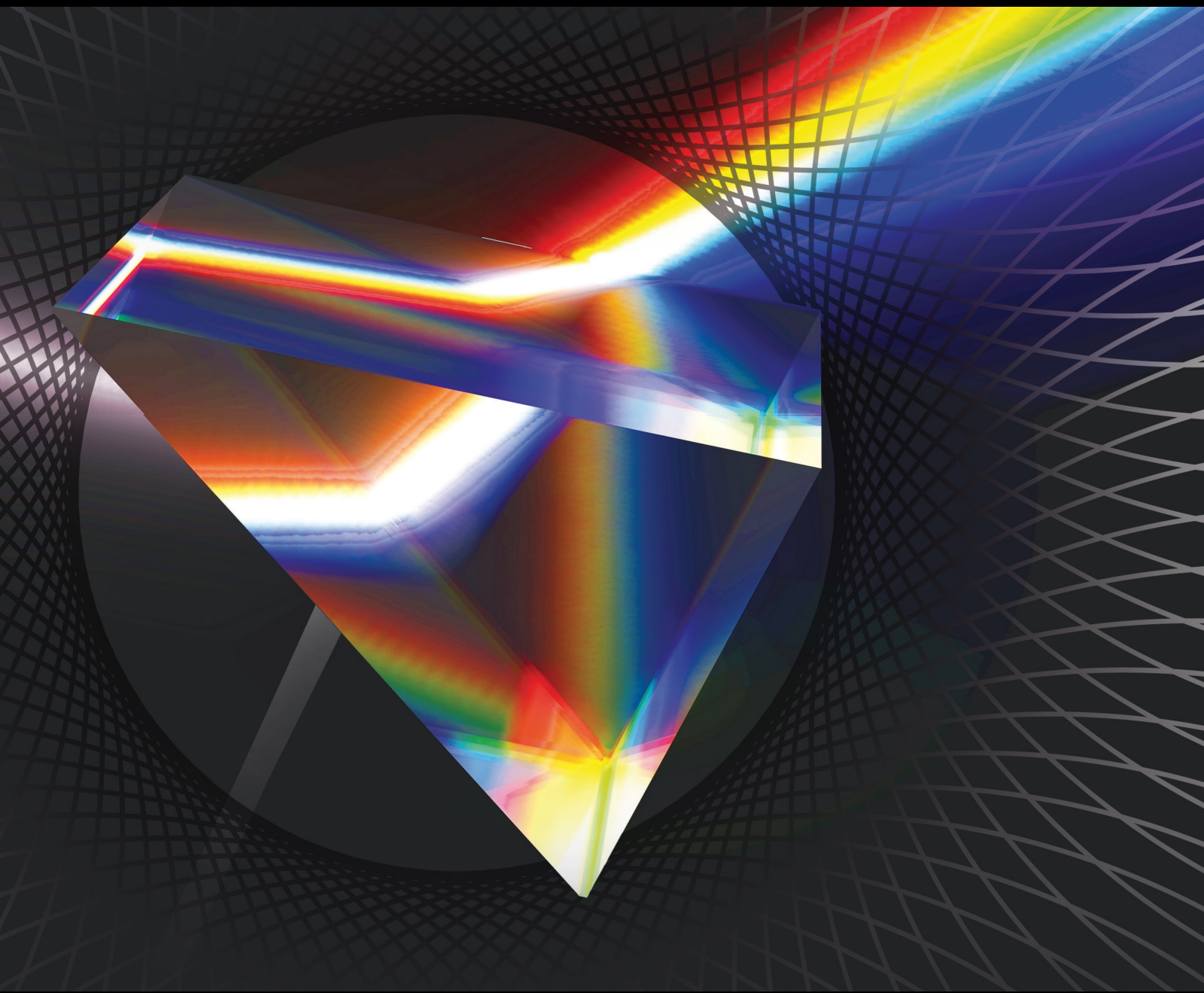

Photonics Applications in Biomedicine and Human Safety

International Journal of Optics

Photonics Applications in Biomedicine and Human Safety

Lead Guest Editor: Hsiao-Yi Lee
Guest Editors: Cheng-Mu Tsai, Tsair-Fwu Lee, Winston Chen, and Chun-Ming Huang

Chief Editor

Academic Editors

Contents

Hindawi
International Journal of Optics
Volume 2020, Article ID 6145638, 9 pages
https://doi.org/10.1155/2020/6145638

Research Article

Design of Counter Beam Tunnel Lights for CIE 88 : 2004 Regulation in Threshold Zone

Ming-Jui Chen,[1] Hien-Thanh Le,[1,2] Lanh-Thanh Le,[1,2] Wei-Hsiung Tseng,[3] Wei-Yang Lee,[1] Si-Yuan Chen,[1] Sheng-Yen Chen,[1] Hsing-Yuan Liao,[1] Yung-Cheng Li,[4] and Hsiao-Yi Lee[1,5]

[1]*Department of Electrical Engineering, National Kaohsiung University of Science and Technology, Kaohsiung 80778, Taiwan*
[2]*Department of Technology, Dong Nai Technology University, Bien Hoa 830000, Dong Nai, Vietnam*
[3]*Department of Aviation & Communication Electronics, Air Force Institute of Technology, Kaohsiung City 820, Taiwan*
[4]*Department of Materials Science and Engineering, National Tsing Hua University, No. 101, Section 2, Kuang-Fu Road, Hsinchu 30013, Taiwan*
[5]*Department of Graduate Institute of Clinical Medicine, Kaohsiung Medical University, Kaohsiung 807, Taiwan*

Correspondence should be addressed to Hsiao-Yi Lee; leehy@nkust.edu.tw

Received 5 December 2019; Revised 27 February 2020; Accepted 3 March 2020; Published 30 March 2020

Academic Editor: Sulaiman W. Harun

To enhance driving safety, a counter beam light is proposed to meet CIE (International Commission on Illumination) specifications for tunnel lighting. The proposed new counter beam light (CBL) acts as a qualified counter beam light to help tunnel road lighting meet the CIE 88 : 2004 regulation standard in the threshold zone in both simulation and in practice. Through appropriate arrangements of the counter beam light and conventional fluorescent lights on the tunnel ceiling, we demonstrate that road tunnel lighting meeting CIE 88 : 2004 standards can be accomplished. Based on LiteStar four-dimensional simulation, the source file created through the measurement of the proposed CBL prototype achieved an average road surface brightness of 121 cd/m^2, which is greater than the minimum regulation level of 105 cd/m^2, a brightness uniformity of 0.88 (minimum regulation level of 0.4), longitudinal brightness uniformity of 0.98 (minimum regulation level of 0.6), a glare factor of 4.41% (maximum level of 15%), and a contrast revealing coefficient of 1.08, which is above the 0.6 minimum level in the threshold zone.

1. Introduction

The main objective of tunnel lighting is to allow traffic to enter, pass through, and exit the enclosed section of the tunnel safely [1–4]. These aims are achieved through the adequate illumination of the tunnel interior, which allows drivers to quickly adjust to the light and identify possible obstacles on the road in tunnels. The threshold zone is the first zone within the actual tunnel that extends for the same length as the stopping sight distance for the design [5–8]. When using the L_{20} method, the target luminance level L_{th} (threshold zone luminance) for this zone is derived from the portal luminance (L_{20}) factored by the k value associated with the class of tunnel [9, 10, 11]. This level is maintained at 100% for the first half of the threshold zone and reduces to 40% by the end of the zone. The k factor is inversely proportional to the contrast revealing coefficient q_c, so if q_c can be elevated, the required L_{th} can be decreased, which can provide the necessary lighting conditions for the tunnel road while decreasing the consumed electrical power and the maintenance cost of lighting. However, since the new CIE 88 : 2004 regulation was published, updating tunnel lights to achieve a high contrast revealing coefficient is rarely performed, so few commercial tunnel lights are qualified as counter beam lights [12, 13, 7]. Many newly built tunnels, such as the Conway Eastbound tunnel on the A55 in the U.K., adopt symmetrical lights in threshold zone, guaranteeing a q_c of only more than 0.2 [14, 15, 16]. To decrease the

L_{th} level and follow the CIE 88 : 2004 regulation and as counter beam lights can guarantee a q_{c} higher than 0.6, they are always considered for tunnel lighting.

In this study, a freeform surfaced luminaire is proposed to handle 400 W high-pressured sodium lamps to act as the counterbeam lights for CIE 88 : 2004 tunnel road lighting. The efficiency and lifespan of white light emitting diodes (LEDs) have improved, but the golden light of high-pressured sodium lamps has the specific advantage of high fog permeability and low insect attraction, which increase driver safety in the threshold and exit zones, where the dangerous black-hole effect or white hole effect need to be addressed. As a result, lights with high-pressured sodium lamps are still commonly used in the entrances and exits of tunnels. The proposed counterbeam light was prototyped and its intensity distribution was measured using a goniophotometer to obtain its far field data. By importing the data into tunnel lighting analysis software, we found that the counter beam light combined with conventional fluorescent lights can meet tunnel road lighting CIE 88 : 2004 regulations in the threshold zone, yielding an average road surface luminance L_{av} of 130 cd/m^2, which is greater than the minimum regulation level of 105 cd/m^2, a luminance uniformity U_{o} of $0.89 > 0.4$ (minimum regulation level), a longitudinal luminance uniformity U_{L} of $0.99 > 0.6$ (minimum regulation level), a glare factor T_{I} of 5.5% < 15% (maximum level), and a contrast display factor q_{c} of $1.24 > 0.6$ (minimum level) in the threshold zone.

2. Principles

The major difference between tunnel lighting and conventional road lighting is in the need for lighting by day [17, 18, 19]. A driver needs to be able to see a certain distance ahead so that if an unexpected hazard appears, the driver can react and stop within that distance. When this distance extends into a tunnel, the lighting level inside should be sufficiently high to maintain visibility. If the lighting level is not high, the driver will be unable to see into the tunnel, which is called the black-hole effect. During approach and entry into a tunnel, drivers' eyes adapt to the darker surroundings. This adaptation is a continuous process, so the further into the tunnel the driver travels, providing the tunnel is of sufficient length, the lighting level may be steadily reduced until it reaches a constant level in the tunnel interior zone. On emerging from a tunnel into daylight, the eye adapts far more quickly to the higher luminance level. The lighting of a tunnel should be sufficient to prevent the black-hole effect when a driver is unable to see into the tunnel. As such, tunnel road lighting must satisfy some stringent requirements, such as the CIE 88 : 2004 regulation.

In order to avoid encountering the black-hole effect when approaching the portal of a tunnel and to help drivers adapt to the lighting environment in a tunnel, there are five lighting zones distributed throughout a tunnel such as access zone, threshold zone, transition zone, interior zone, and exit zone. The transition zone is given by

$$L_{tr} = L_{th} \times (1 \cdot 9 + t)^{-1,4}, \tag{1}$$

where L_{tr} is the road surface luminance in the transition zone, L_{th} is the road surface luminance in the threshold zone, and t is the driving time in seconds. The necessary driving time in the transition zone t_{tr} is then given by

$$\text{t}_{\text{tr}} = \left(\frac{L_{in}}{L_{th}}\right)^{-0.714} - 1.9 \text{ seconds}. \tag{2}$$

The threshold zone is the first inner region encountered when entering a tunnel and where the black-hole effect critically dominates. Based on the CIE 88 : 2004 regulation, the threshold zone luminance is usually set to be higher than L_{th}.:

$$L_{th} = \frac{L_m}{1/C_m(\rho/\pi \ . \ q_c - 1) - 1}, \tag{3}$$

where $L_m = (\tau_{\text{ws}} \times L_{\text{atm}} + L_{\text{ws}} + L_{\text{seq}})/(\tau_{\text{ws}} \times \tau_{\text{atm}})$, C_{m} is the minimum required perceived contrast (–0.28), ρ is the reflectance factor of the target (0.2), τ_{ws} is the windscreen transmission factor (0.8), τ_{atm} is the atmosphere transmission factor (1.0), $L_{\text{seq}} = 5.1 \times 10^{-4} \Sigma \, \text{L}_{\text{ije}}$ with $L_{ije} = (\tau_{\text{ws}} \times L_{ij}) + \text{L}_{\text{ws}}$ is the equivalent veiling luminance, L_{ije} is the luminance of each section in front of the eye (cd/m^2), L_{ij} is the average luminance of each section measured outside the car in front of the windscreen (cd/m^2), L_{atm} is the atmospheric veiling luminance (200 cd/m^2, medium veiling level), L_{ws} is the windscreen veiling luminance (100 cd/m^2, medium veiling level), and q_{c} is the contrast revealing coefficient (≥0.2 for symmetrical light systems or ≥0.6 for counterbeam light systems).

Based on the Holladay–Stiles formula, the equivalent veiling luminance L_{seq} can be determined busing a graphical method to identify L_{th}. The equivalent veiling luminance L_{seq} is found from $L_{\text{seq}} = 5.1 \times 10^{-4} \Sigma \ L_{ije}$ with $L_{ije} = (\tau_{\text{ws}} \times L_{ij}) + L_{\text{ws}}$. The contrast revealing coefficient ($q_{\text{c}} = L/\text{E}_{\text{v}}$) is the ratio between the luminance of the road surface and the vertical illuminance Ev at a specific location in the tunnel. C_{m} is the minimum required perceived contrast, where 28% is recommended. This contrast is mostly negative (for any q_{c} greater than 0.06 with a reflectance factor of the target equal to 0.2). To determine the threshold road luminance, the designer should start from the standardized figures for the contrast revealing coefficient (either 0.2 for symmetrical light systems or 0.6 for counterbeam light systems). To identify a more precise threshold luminance value, an iterative process is necessary. After selecting an initial estimated figure for the average q_{c} of the installation and calculating the correlated L_{th}, the real average q_{c} of the installation may need to be calculated to verify initial assumptions. In general, the atmospheric transmissivity (τ_{atm}) for design purposes is assumed to be 1.0 and the transmission factor for the windscreen (τ_{ws}) is assumed to be 0.8. Disability glare reduces visibility and shall be minimized. If disability glare is controlled under tunnel lighting conditions, then discomfort glare will also be controlled. Disability glare effects shall be quantified by means of threshold increment (T_{I}). Good uniformity of luminance must be provided on the road surface. The recommended minimum to the average value of the luminance on the road surface in

clean conditions of the tunnel is 0.4. A longitudinal uniformity of 0.6 along the center of each lane is recommended for the road. It is recommended that these values are independently reached on the length of the step. The values of 0.4 and 0.6 are those corresponding to the values for normal road lighting provided in CIE 115-1995 [7, 13].

Asymmetrical directional lighting, such as counterbeam and probeam lighting, distributes patterns in only one direction, either with or against traffic. Counterbeam lighting directs the maximum optical intensity against traffic along the driver's line of vision, creating a high negative contrast. By minimizing glare, drivers can clearly see the contours of the vehicle ahead. Probeam lighting directs the maximum candlelight with the traffic away from the driver, providing high object luminance and low road luminance, creating a positive contrast. This system operates by minimizing luminaire glare and increasing distance visibility.

3. Experimental Setup and Results

The tunnel for the study is located in the eastern part of Taiwan, and its entrance is shown in Figure 1. The geometry of the tunnel is shown in Figure 2, and its details are as follows: motorway tunnel, 2 unidirectional bores; two traffic lanes, 3.75 m each; total width, 10 m; ceiling height, 8.05 m; and length of tunnel, >500 m. The tunnel orientation is south to north.

The amount of lighting required within a tunnel is dependent on the level of ambient lighting at which visual adaptation for the driver is possible on the tunnel approach and inside the tunnel. To achieve this, the lighting of a tunnel is divided into specific zones; the threshold zone and the transition zone are shown in Figure 3. Using the Holladay–Stiles formula, the equivalent veiling luminance Lseq can be determined using a graphical method embedded in LiteStar4D software (OxyTech, Milan, Italey), as shown in Figure 4. The overlay lines and segments are related to the Holladay–Stiles formula [1], which results in a luminance reduction curve and $L_{th} = 178\ \text{cd/m}^2$, as shown in the green curve of Figure 5. In the threshold zone, considering the daylight shining into the tunnel, the minimum average road surface brightness L_{av} due to tunnel light greater than $105\ \text{cd/m}^2$ is sufficient. Based on CIE 115-1995, the brightness uniformity U_{o} and the longitudinal brightness uniformity U_{L} should be higher than 0.4 and 0.6, respectively; the glare factor T_{I} needs to be larger than 15%; and the contrast revealing coefficient must be larger than 0.6 for economic reasons.

The criteria of the tunnel lighting design are as follows:

(1) The speed limit of approach road = 70 km/h

(2) Stopping distance = 49.4 m

(3) Tunnel Class 2, one-way traffic, motorized only

(4) Traffic flow rate: 500–1000 vehicles per hour per lane during peak hour

To meet the abovementioned targets, counterbeam lights (CBLs) with one OSRAMVIALOX Nav-T Super 400 W/56,500 lumen sodium lamp and linear symmetrical lights

Figure 1: The entrance to the studied tunnel.

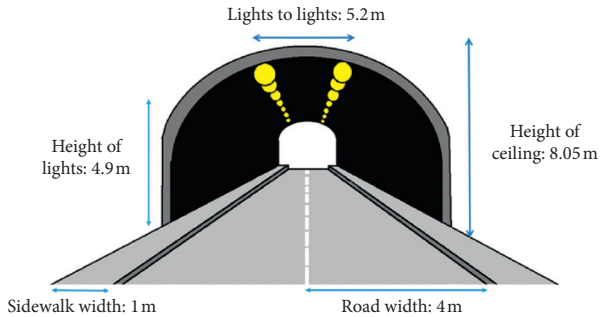

Figure 2: The configuration of the trial tunnel geometry.

with two T5 MASTER TL5 HE 35 W/840 SLV/20 fluorescence tubes with efficacy of 94 lumen/W were arranged regularly in the threshold zone. The layout of the lighting design is shown in Figure 6. The spacing of the lights was set to 1.6 m with one linear light followed by three counterbeam lights in, and then repeating the same arrangement until the end of the zone. For the experiments, the design process of the proposed CBL with sodium lamps is presented. The CBL was prototyped to demonstrate its feasibility for tunnel road lighting for CIE 88 : 2004.

The new CBL is composed of a freeform surfaced reflector and one 400 W ORSAM high-pressured sodium lamp. With the aim of achieving a contrast revealing coefficient qc higher than 0.6, the new CBL model was built using SolidWorks (DASSAULT SYSTEMES, USA) mechanical software, analyzed using TracePro (Lambda Research, USA) optical software, and optimized with LightTools (Synopsys, USA) software. The design workflow is shown in Figure 7.

During the design process, the optical models of the lamp and reflector were built first, as shown in Figures 8(a) and 8(b), respectively. To determiend the accuracy of the lamp model, the model file was imported into TracePro software for evaluation. Then, we connected the lamp model to the reflector model in TracePro and LightTools as the complete counterbeam light, as shown in Figure 9, to conduct ray tracing analysis and optimization, respectively. The initial reflector model was built, as shown in Figure 10(a), in which surface radii R_1 and R_2 were set to 137 and 115 mm, respectively, and the lamp position was set to $(49, -36{,}100)_{xyz}$.

Using TracePro, the intensity distribution of the CBL was analyzed, as shown in Figure 10(b), and its far field source file was obtained. However, based on the geometry of the trial tunnel and the criteria of the tunnel lighting design, after importing the source files of CBL and the T5 fluorescence light into LiteStar 4D for tunnel road lighting

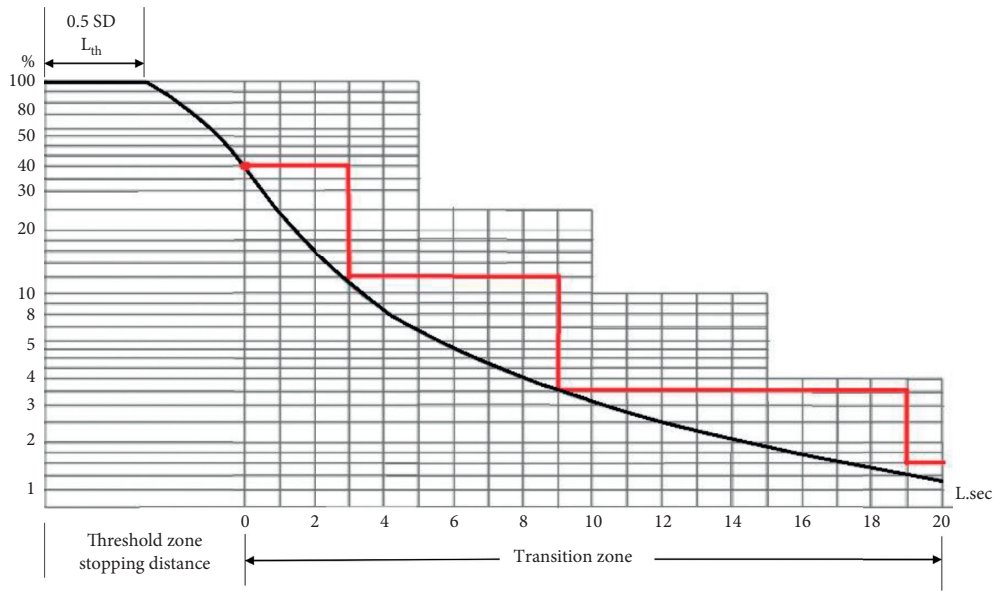

Figure 3: The black line is the luminance reduction curve for CIE 88 : 2004 standard. The length of threshold zone = 0.5 SD, where L_{th} is 100 %. Threshold zone length = stopping distance (SD). The red lines indicate the target luminance in the zones of tunnels.

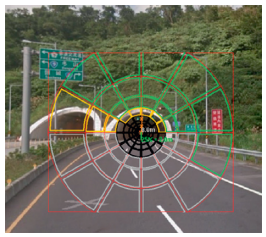

Figure 4: L_{seq} evaluation diagram of the trial tunnel.

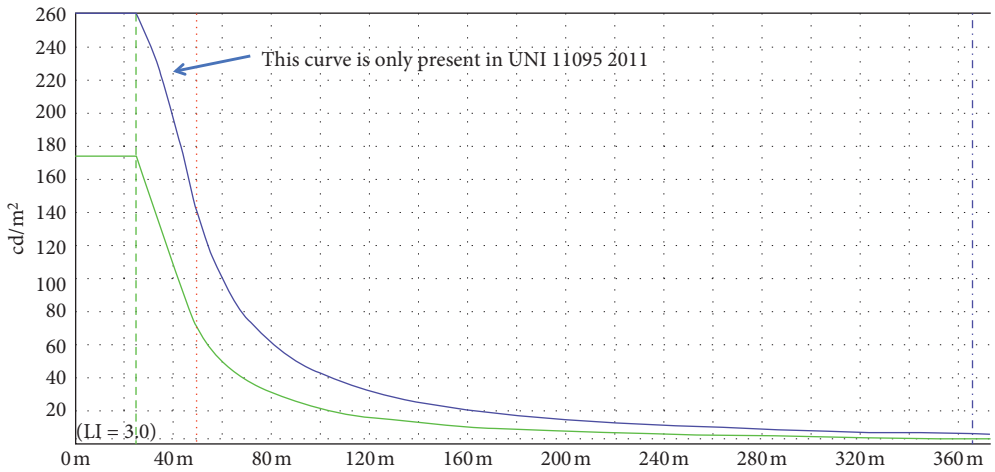

Figure 5: The luminance reduction curve, which indicates the minimum required luminance for accomplishing the standards for the trial tunnel generated by LiteStar 4D software (green curve: CIE 88 : 2004 standar, blue curve: UNI 11095.

simulation, the output report showed that its contrast revealing coefficient q_c was 0.24, which is less than 0.6. That means that the initially designed CBL was insufficient. Therefore, the CBL model was optimized using LightTools with the target of a q_c larger than 1.0 in the threshold zone. Through the global searching method with reflector surface radius and lamp position acting as the variables, the CBL was optimized, as shown in Figure 11(a). Its intensity

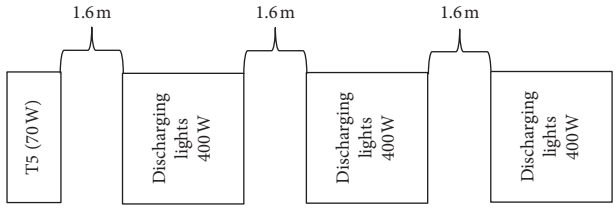

Figure 6: The tunnel lighting configuration of one 75 W T5 fluorescence light followed by three 400 W discharging lights with sodium lamp for each traffic lane is repeated from the entry to the end of threshold zone.

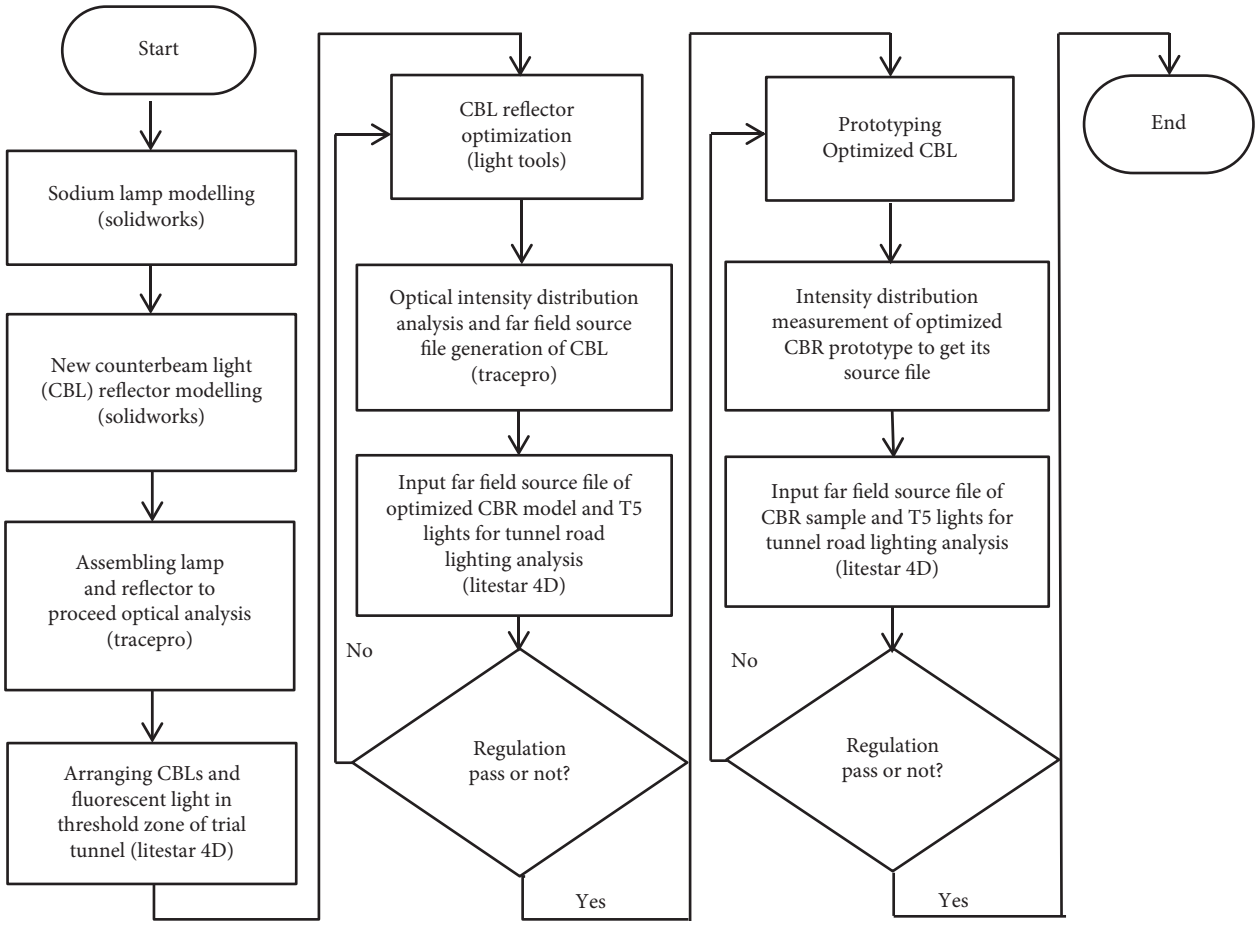

Figure 7: The workflow of optimizing counter beam light to accomplish CIE 88 : 2004 tunnel lighting design.

distribution is shown in Figure 11(b). After optimization, the CBL had an R_1 of 1000 mm and R_2 of 85 mm, and the lamp position shifted to $(74, -65, 90)_{xyz}$ from $(49, -36, 100)_{xyz}$. We input the far field source of the optimized CBL into LiteStar 4D; the output report showed that its contrast revealing coefficient q_c was 1.11, which is above 0.6, indicating that the new design would qualify as a counterbeam light. The tunnel road lighting performance evaluation items, including average road surface luminance L_{av}, brightness uniformity U_o, longitudinal brightness uniformity U_L, glare factor T_I, and q_c of the initial and final designs of the new CBL are listed in Table 1 for comparison.

To show that the optimized CBL allows the tunnel lighting to meet CIE 88 : 2004 specifications, a reflector composed of stainless steel was prototyped for optical analysis, as shown in Figure 12. The new CBL fixture installation with the 400 W sodium lamp with 56,500 lumens is shown in Figure 13, which was measured by imaging goniophotometers (Radiant Imaging Co. Ltd.) to obtain its intensity distribution (Figure 14) and its far field source file, which shows the fixture output power was 37,054 lumens. Therefore, the efficacy was calculated as 37,054/400 = 93 lumen/W. Therefore, after the source file of the optimized CBL sample was loaded in LiteStar 4D, the output report showed that its q_c was 1.19 (>0.6), which means that the optimized CBL could act as a counterbeam light for tunnel lighting in practice. The tunnel lighting evaluation items, including average road surface luminance L_{av}, brightness

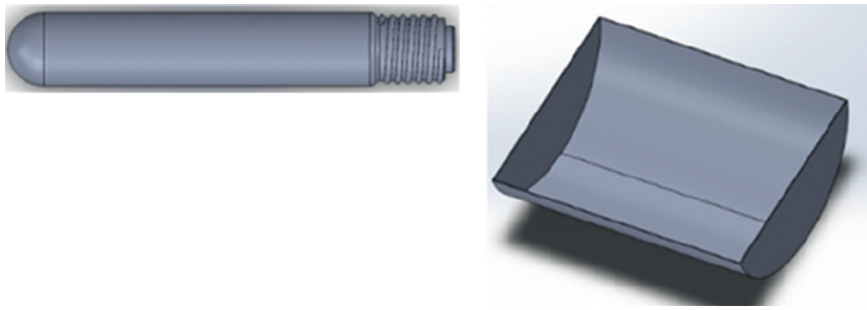

(a) (b)

Figure 8: (a) Model of ORSAM VIALOX NAV-T SUPER 4Y series 400 W sodium lamp; (b) model of the initial designed reflector of the proposed counterbeam light.

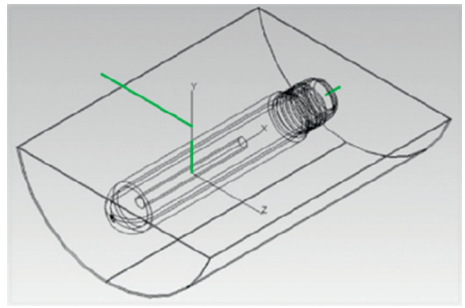

Figure 9: The model of the new counterbeam light.

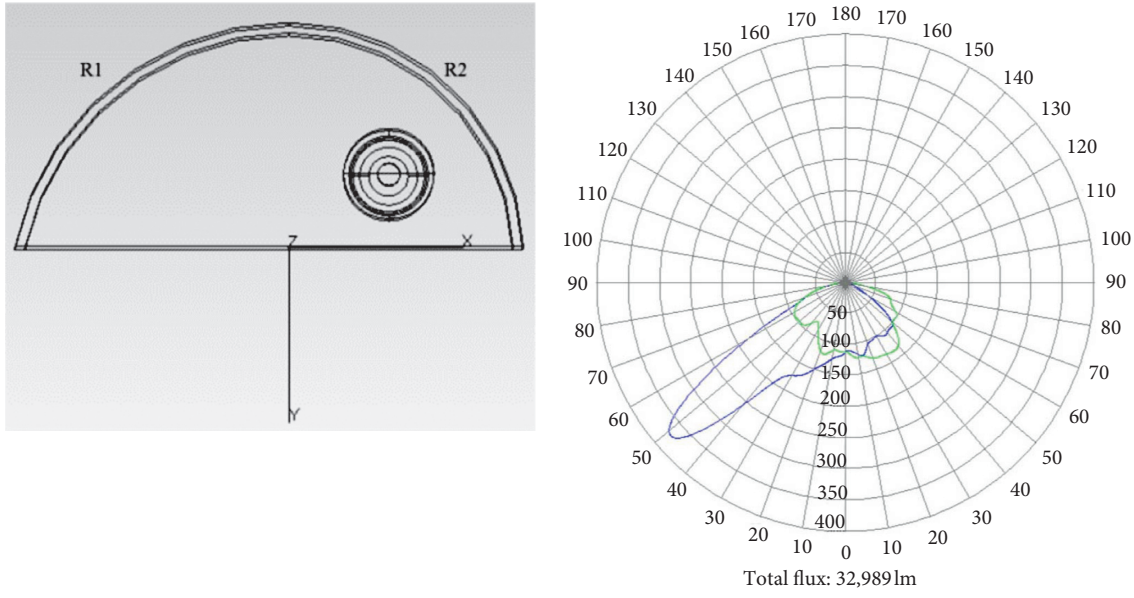

(a) (b)

Figure 10: (a) The side view of the the new counterbeam light before optimization; R1 and R2 are the surface radius of the light. (b) The simulated intensity distribution of the new counterbeam light before optimization.

uniformity U_o, longitudinal brightness uniformity U_L, glare factor T_I, and q_c of the optimized CBL design and the measurements from the sample are both listed in Table 2 to compare the performance differences.

To demonstrate the advantage of the optimized new CBL, the 400 W sodium lamp tunnel light GE17734 (General Electric Co., Ltd.), broadly used in tunnels, was used to compare their performance in the threshold zone. The

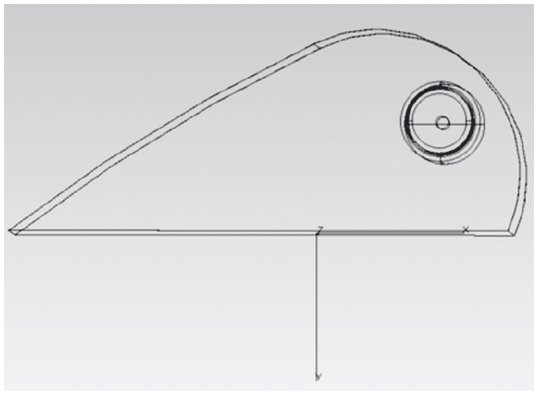

(a)

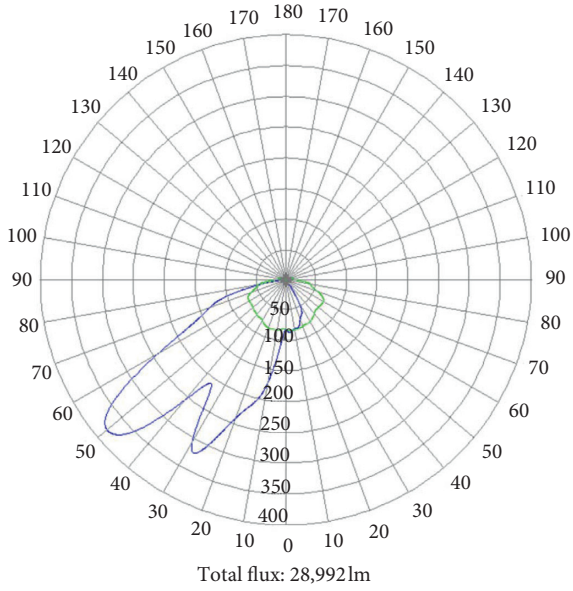

(b)

Figure 11: (a) The side view of the new counterbeam light after optimization; (b) the simulated intensity distribution of the optimized CBL with a 400 W sodium lamp.

Table 1: The comparison of lighting performance between the initially designed new CBL and the new optimized CBL for the tunnel threshold zone.

Variable	Before optimization	After optimization	CIE standard
L_{av} (cd/m^2)	121 (pass)	123 (pass)	**>105**
U_o	0.87 (pass)	0.84 (pass)	**>0.4**
U_L	0.98 (pass)	0.97 (pass)	**>0.6**
T_I	3.6% (pass)	10.41% (pass)	**<15%**
q_c	0.26 (failed)	1.19 (pass)	**>0.6**

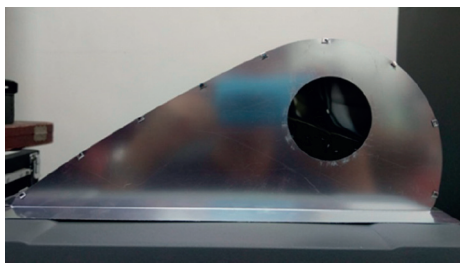

Figure 12: The prototype of the optimized CBL reflector.

Figure 13: The prototype of the optimized CBL light.

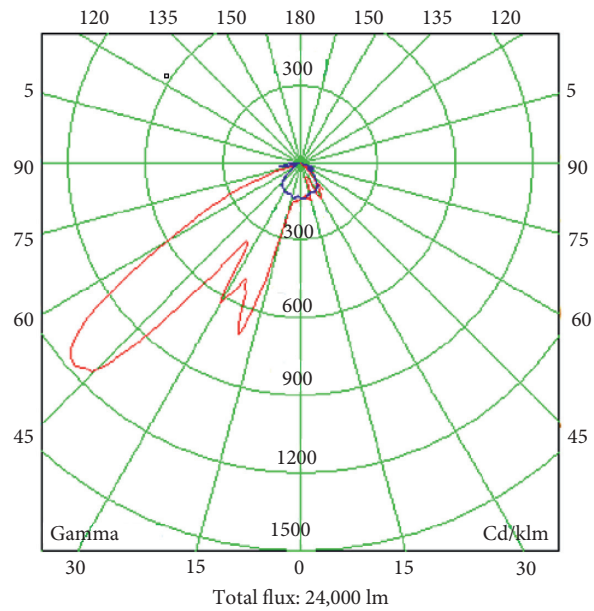

Figure 14: The measured intensity distribution of the optimized CBL with the 400 W sodium lamp.

measured intensity distribution of the GE17734 (General Electric Co., Ltd.) is shown in Figure 15; the output power was 36,865 lumens, and the efficacy was calculated as 36,865/400 = 92 lumen/W. The lighting performance between the optimized new CBL and the GE17734 (General Electric Co. Ltd.) in threshold zone of tunnel is compared in Table 3. The q_c of GE17734 was 0.55, which is below the standard and much smaller lower than that (1.08) of the optimized CBL.

Table 2: Comparison of lighting performance between the optimized new CBL design and prototype sample measurements in threshold zone of a tunnel.

Variable	Simulation model of the optimized new CBL	Prototyped sample of the optimized new CBL	CIE standard
L_{av} (cd/m2)	123 (pass)	121 (pass)	**>105**
U_o	0.84 (pass)	0.88 (pass)	**>0.4**
U_L	0.97 (pass)	0.98 (pass)	**>0.6**
T_I	10.41% (pass)	4.41% (pass)	**<15%**
q_c	1.19 (pass)	1.08 (pass)	**>0.6**

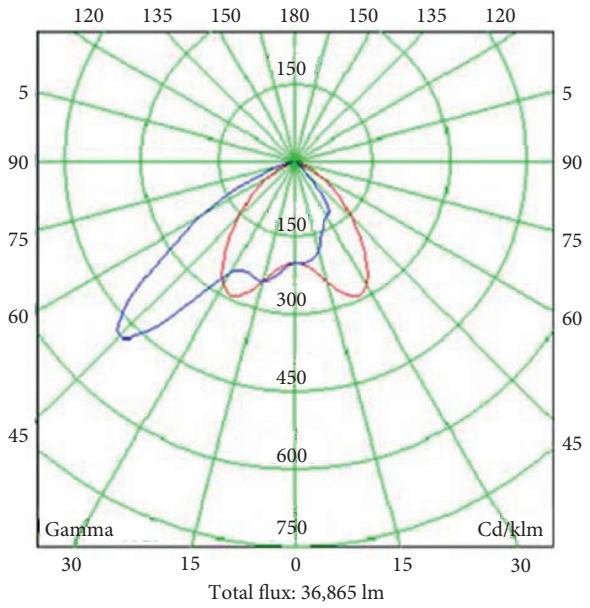

Figure 15: The measured intensity distribution of the GE17734 CBL (General Electric Co. Ltd.) with the 400 W sodium lamp.

Table 3: Comparison of the lighting performance between the GE17734 sodium tunnel light and the optimized new CBL.

Parameter	GE17734 sodium tunnel light	Prototyped sample of the optimized new CBL	CIE standard
L_{av} (cd/m2)	139 (pass)	121 (pass)	**>105**
U_o	0.82 (pass)	0.88 (pass)	**>0.4**
U_L	0.98 (pass)	0.98 (pass)	**>0.6**
T_I	1.55 % (pass)	4.41% (pass)	**<15%**
q_c	0.55 (failed)	1.08 (pass)	**>0.6**

4. Discussion and Conclusions

To improve driving safety, a new counterbeam light (CBL) was proposed to meet CIE 88 : 2004 regulations for tunnel lighting. Using appropriate arrangements of the counterbeam light and conventional fluorescent lights on the ceiling of a tunnel, we demonstrated that road tunnel lighting with CIE 88 : 2004 regulations can be accomplished in the LiteStar 4D simulation environment. Based on the simulated physical source model, the new counterbeam can produce an average road surface brightness of 123 cd/m^2 (minimum regulation level = 105 cd/m^2), a brightness uniformity U_o of 0.84 (minimum regulation level = 0.4), a longitudinal brightness uniformity U_L of 0.97 (minimum regulation level = 0.6), a glare factor T_I of 10.41% (maximum level = 15%), and a contrast revealing coefficient q_c of 1.19 (minimum level = 0.6) in the threshold zone. For demonstrating the feasibility of the new CBL in tunnels, a prototype was constructed and measured using an imaging goniophotometer. Based on LiteStar 4D simulation, the source file created through the measurement of the new CBL sample achieved an average road surface brightness L_{av} of 121 cd/m^2 (minimum regulation level = 105 cd/m^2), a brightness uniformity U_o of 0.88 (minimum regulation level = 0.4), a longitudinal brightness uniformity U_L of 0.98 (minimum regulation level = 0.6), a glare factor T_I of 4.41% (maximum level = 15%), and a contrast revealing coefficient q_c of 1.08 (minimum level = 0.6) in the threshold zone. As a result, we concluded that the proposed CBL can act as a qualified counterbeam light to help tunnel road lighting meet CIE 88 : 2004 standards both in simulation and in practice.

We compared the performance of the GE17734 tunnel light and the new CBL before and after optimization. The experimental results (Tables 1–3) showed that the road luminance produced by the optimized new CBL is the lowest but has the highest q_c, which means cars, people, or other objects observed on road are the most contrasted, revealed by the optimized CBL. The results shown in Figures 15, 10(b), and 11(b) show that the optimized new CBL has a weaker light intensity at 40°–45°, meaning light dominates the road luminance of drivers, so the optimized new CBL cannot provide as much luminance as the other fixtures.[20]

Data Availability

No data were used to support this study.

Conflicts of Interest

The authors declare that they have no conflicts of interest.

Authors' Contributions

The authors contributed equally to all parts of this study.

References

[1] R. H. Simons and A. R. Bean, *Lighting Engineering: Applied Calculations*, Routledge, Abingdon, UK, 2008.

[2] J. A. Vrooman, *Crossing the Threshold: Nabi Depictions of Masculinity in Public, Private, and Performative Spaces of Fin-De-SiècleParis*, Dissertation, New York University, New York, NY, USA, 2017.

[3] M. Rea, J. Bullough, and Y. Akashi, "Several views of metal halide and high-pressure sodium lighting for outdoor applications," *Lighting Research & Technology*, vol. 41, no. 4, pp. 297–320, 2009.

[4] M. S. Rea, A. Bierman, T. McGowan, F. Dickey, and J. A. Havard, "Eld study comparing the eŒectiveness of metal halide and highpressure sodium illuminants under mesopic

conditions," in *Proceedings of the Visual Scales: Photometric and Colorimetric Aspects*, London, UK, March 1997.

[5] Guide for the Lighting of Road Tunnels and Underpasses, 2nd EdCIE 088-1990, 1990.

[6] J. Da Silva FM, H. M. Bártolo, P Bártolo et al., *Challenges for Technology Innovation: An Agenda for the Future: Proceedings of the International Conference on Sustainable Smart Manufacturing (S2M 2016)*, CRC Press, Lisbon, Portugal, 2017.

[7] J. E. M. Teoh, C. K. Chua, Y. Liu, and J. An, "4D printing of customised smart sunshade: a conceptual study," *Challenges for Technology Innovation: An Agenda for the Future*, vol. 105, no. 108, pp. 105–108, 2017.

[8] P. R. Boyce, N. H. Eklund, B. J. Hamilton, and L. D. Bruno, "Perceptions of safety at night in different lighting conditions," *Lighting Research and Technology*, vol. 32, no. 2, pp. 79–91, 2000.

[9] W. V. Bommel, *Road Lighting: Fundamentals, Technology and Application*, Springer, Berlin, Germany, 2014.

[10] S. W. Smith and M. S. Rea, "Relationships between office task performance and ratings of feelings and task evaluations under different light sources and levels," in *Proceedings of the19th Session of Commission Internationale de l'Éclairage*,Kyoto, Japan, 1980.

[11] Y. Akashi, M. S. Rea, and J. D. Bullough, "Driver decision making in response to peripheral moving targets under mesopic light levels," *Lighting Research & Technology*, vol. 39, no. 1, pp. 53–67, 2007.

[12] Z. Feng, Y. Luo, and Y. Han, "Design of LED freeform optical system for road lighting with high luminance/illuminance ratio," *Optics Express*, vol. 18, no. 21, pp. 22020–22031, 2010.

[13] Commission Internationale de l'Éclairage, *Lighting of Roads for Motor and Pedestrian Traffic: CIE 115*, CIE, Peter Blattner; Switzerland, 2010.

[14] C. Knight, "Field surveys of the effect of lamp spectrum on the perception of safety and comfort at night," *Lighting Research & Technology*, vol. 42, no. 3, pp. 313–329, 2010.

[15] S. Fotios and R. Gibbons, "Road lighting research for drivers and pedestrians: the basis of luminance and illuminance recommendations," *Lighting Research & Technology*, vol. 50, no. 1, pp. 154–186, 2018.

[16] A. Scott, "White light-the UK balance sheet," *Lighting Journal*, vol. 70, no. 1, 2005.

[17] S. Hecht, C. Haig, and A. M. Chase, "The influence of light adaptation on subsequent dark adaptation of the eye," *The Journal of General Physiology*, vol. 20, no. 6, pp. 831–850, 1937.

[18] B. Ahmed, *Road Lighting*, 2017.

[19] P. R. Boyce, *Lighting for Driving: Roads, Vehicles, Signs, and Signals*, CRC Press, Boca Raton, FL, USA, 2008.

[20] P. R. Boyce and L. D. Bruno, "An evaluation of high pressure sodium and metal halide light sources for parking lot lighting," *Journal of the Illuminating Engineering Society*, vol. 28, no. 2, pp. 16–32, 1999.

Hindawi
International Journal of Optics
Volume 2020, Article ID 8652108, 6 pages
https://doi.org/10.1155/2020/8652108

Research Article

The Influence of LED Lighting on Attention and Long-Term Memory

Chung Won Lee [1] **and Jin Ho Kim** [2]

[1]*Kyungwoon University, Gumi, Republic of Korea*
[2]*Kongju National University, Gongju, Republic of Korea*

Correspondence should be addressed to Jin Ho Kim; kjh@kongju.ac.kr

Received 14 October 2019; Revised 5 February 2020; Accepted 27 February 2020; Published 23 March 2020

Guest Editor: Tsair-Fwu Lee

The fact that the illuminance of LED lights affects human attention and long-term memory has been verified through various studies, but there are no consistent research results about what level of illuminance is effective. The aims of this study were to systematically verify the effects of LED lighting on attention and long-term memory. The experiment was designed with four illuminance levels—300 lx, 400 lx, 500 lx, and 1,000 lx—as experimental conditions to determine the effects of LED lights on attention and long-term memory. Participants in the experiment were 18 college students. The attention task was performed using a handmade attention measuring instrument. Long-term memory was measured by the word fragment completion (hereinafter, referred to as "WFC") task on the memory retention volume of the learning task that was learned exactly 24 hours before. Of the total 20 tasks, the ratio of correctly retrieval tasks was used as a dependent variable. As a result, attention showed the highest performance with a mean performance of 19.39 (SD = 3.78) at 1,000 lx. A statistically significant difference was also found between the 1,000 lx and 300 lx conditions ($p = 0.01$). On the contrary, long-term memory showed the highest retrieval rate at an average of 58.06% (SD = 22.57) at 400 lx, and long-term memory performance was better in the order of 500 lx (mean = 48.89, SD = 20.33), 1,000 lx (mean = 45.83, SD = 23.53), and 300 lx (Mean = 43.33, SD = 19.10). Statistically, there was a significant difference between 300 lx and 400 lx ($p = 0.01$), 400 lx and 1,000 lx ($p = 0.01$). Through this study, it was verified that the effects of attention and long-term memory are different according to the illuminance of LED lighting, and these results can be important data to clarify the influence of light on human memory in the future.

1. Introduction

Light affects the 24-h circadian rhythm and is accepted as the main cause of activity and acute alerting [1, 2]. In particular, the illumination of light has been reported to affect cognitive functions such as attention, working memory, and long-term memory [3–8]. However, research findings on the effects of light have not always been consistent. Though some studies have suggested that a relatively bright light produces psychological alertness and that the effect leads to improved attention and cognitive performance, other studies have failed to find improved cognitive performance or have even found lower performance in the bright light condition [9–11]. For example, in the study by Kretschmer et al. [12], the correct response performance of the working memory task was statistically much better in the bright condition (3,000 lx) than in the dim condition (300 lx), but the false response performance did not show a significant difference in both conditions. And, sustained attention did not show any significant difference in both bright light and dim light conditions [12]. This inconsistent aspect of the light effect can cause a lot of confusion in the use of light in real scenes.

One of the reasons for the inconsistency between the results of illuminance and cognitive performance is that the illuminance conditions are often designed by binominal approach of bright light vs. dim light. This type of comparison is bound to have a clear limit to determine the effect of light on cognitive performance. This is because the result

may vary depending on how "bright light" is defined. For example, Campbell and Dawson [13] studied the effect of ambient light on alertness and cognitive performance in night workers and set the three illuminance conditions of 10~20 lx, 100 lx, and 1,000 lx as experimental conditions. As a result, they reported that participants exposed to ambient light of 1,000 lx were significantly improved in alertness and cognitive performance compared to other conditions [13]. Similarly, in the study by Badia et al. [6], they measured alertness and behavior task performance for night workers and reported that bright light was effective in improving alertness and performance [3]. However, the experimental illuminance conditions were set to bright condition (5,000 lx) and dim condition (50 lx), unlike the condition of Campbell and Dawson [13]. In this experiment, the illuminance difference between dim condition and bright condition was 4950 lx. The experimental results of both studies were similar, but there was a significant difference between the bright and dim light they defined. In the abovementioned study by Kretschmer et al. [12], the bright illuminance condition and the dim illuminance condition were 3,000 lx and 300 lx, respectively. The dim illuminance condition defined in this study, 300 lx, was applied to the study by Campbell and Dawson [13], but was it really a dim illumination condition? Of course, the above studies may be meaningful in that they searched that bright light conditions have a positive aspect to alertness and cognitive performance compared to dim conditions, but there clearly was a limit in drawing conclusions as to which illuminance has a positive effect on the actual scene. This is because it is not possible to completely exclude the presence of other illuminance conditions that are excellent in alertness and cognitive performance, and that bright and dark conditions are relative rather than absolute.

Therefore, the study to explore the effects of light illuminance requires a more continuous approach than a binominal approach such as bright light conditions and dim light conditions.

In addition, previous studies on the relationship between light illuminance and cognitive performance focused mainly on working memory, including arousal and attention. But memory does not just mean working memory. According to the multistore model by Atkinson and Shiffrin [14], memory can be divided into sensory memory, short-term memory or working memory, and long-term memory [14].

Long-term memory is a large-capacity repository with no capacity limitations compared to sensory or working memory and can store information for a longer period of time than other memory repositories. The rehearsal information from the working memory is transferred to the long-term memory; the necessary information can be obtained from the working memory retrieved from the long-term storage, and cognitive performance is achieved. In general, the term "remember" which is commonly used in daily life means most of the long-term memory. However, most of the studies between light and memory focus on attention and working memory.

Many studies have been conducted on the effect of light on working memory. The central aspect of working memory is attention, which affects all major processes in memory. As mentioned earlier, many studies on attention and working memory have suggested that working memory is activated at a relatively high illuminance. However, little research has been done as to whether the high illuminance of light is good for the long-term memory. The study by Jung et al. [8] would be the only one that has studied the relationship between light illuminance and long-term memory. They experimented with the superiority of long-term memory at 400 lx, 700 lx, and 1,000 lx using LED lighting. As a result, they claimed that long-term memory was best at 400 lx, a relatively dim condition, unlike working memory [8]. However, their research has not been repeatedly validated by other studies, and there is a limit because long-term memory measurements were made after too short a time (after 5 minutes) after the task was performed. Spaces that are too short after task performance can obscure the boundaries between working memory and long-term memory.

Thus, this study was performed to systematically verify the differences between attention and long-term memory aspects by supplementing the limitations of previous studies. Under this objective, first, the study reverified the previous studies and designed the experiment using a greater spectrum of illuminance than the bright-dim binominal design to determine the optimal illuminance to use in real-life settings. Specifically, the study used 300 lx, 400 lx, 500 lx, and 1000 lx as experimental conditions. These experimental conditions were distributed around 400 lx, the most effective condition for long-term memory according to Jung et al. [8]. Second, in the study, long-term memory was measured 24 hours after the learning task to clearly distinguish long-term memory from working memory and empirically verify the effects of light on long-term memory. Finally, the study included measurements of both attention and long-term memory to gain clear understanding of the performance difference between attention and long-term memory according to illuminance.

2. Materials and Methods

2.1. Participants. The experiment was conducted with 18 adults (5 men and 13 women) with no cognitive impairment and a mean age of 23.3 (SD = 1.14). The recruitment of the experiment participants was done through K University's online bulletin board, and the participants were all students at the university. The recruited experiment participants were given orientation to explain the experiment schedule and method, and only those who successfully performed the task by performing a simple experiment task were selected as the experiment participants. Participants were asked to consume no alcohol or caffeine and to get enough sleep prior to the experiment to prevent negative effects on cognitive performance, and only the participants who agreed to the requirements signed the consent form and participated in the experiment.

2.2. Experiment Environment. The experiment was designed with four illuminance levels (300 lx, 400 lx, 500 lx, and

(a) (b)

Figure 1: LED light (GM10743).

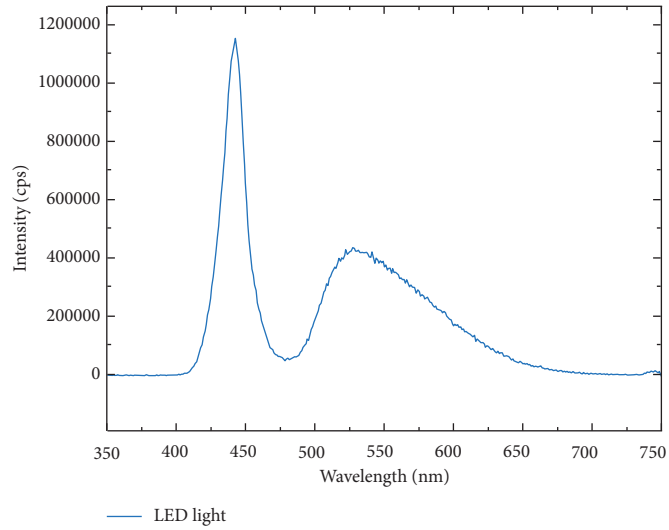

Figure 2: Spectral power distribution.

1000 lx) as experimental conditions to determine the effects of LED lights on attention and long-term memory. The color temperature was 5500 K for all four conditions, which were the same for all variables except the illuminance level. The lighting used in the experiment is a GM10743 model manufactured by Ningbo Golmore Industries, as shown in Figure 1. The product was 9 cm in diameter and contained 5 small LED bulbs. Illuminance was manipulated using 12 lights. In addition, the spectral power distribution of the light used in the experiment is shown in Figure 2.

An experiment environment such as Figure 3 was formed for this study. In the lab, light from other sources was blocked using a light-blocking curtain. The experimental laboratory temperature was maintained at 24°C ± 4°C and 50% ± 10% humidity to meet PMV conditions of ASHRAE standards.

2.3. Attention Measurement. A response measuring device was prepared and used to measure attention. The device consists of 10 symbols (e.g., ∧, ⊂, and Z) and 10 corresponding keys as shown in Figure 4; a user pressed the keys that corresponded to consecutively displayed symbols. The device was set up in such a way that if the user tried to press a button that did not match the displayed symbol, the button could not be pressed down, and the display did not move to the next symbol. In other words, a user had to press the correct button to proceed to the next symbol. The performance of attention task was measured by counting the number of symbols for which the user pressed the correct keys for a minute.

2.4. Long-Term Memory Measurement. Long-term memory was measured by using the WFC task. WFC is a method of measuring long-term memory indirectly by completing the nonsense syllable already learned [15–17]. This study refers to previous studies that applied the WFC task to long-term memory and measured it in accordance with long-term memory. The nonsense syllable task was to learn 20 items per one illuminance condition; 5 items of 4 words, 5 items of 5 words, 5 items of 6 words, and 5 items of 7 words were constructed to minimize the effect of difficulty. Participants learned the nonsensical words and performed the WFC task

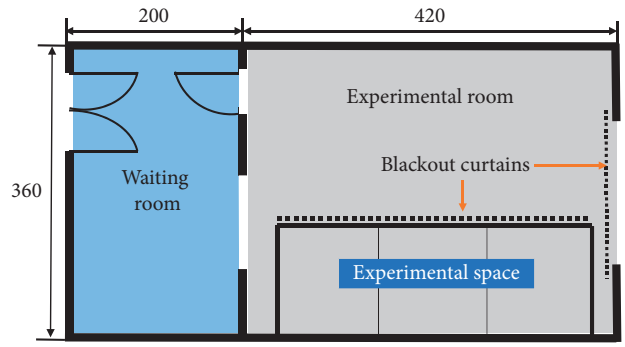

Figure 3: Interior structure of experimental laboratory.

Figure 4: Attention measuring device.

in precisely 24 hours by completing two blank letters in each word (e.g., _ff_ and ry_d_). The performance of the long-term memory task was measured by obtaining the proportion of the correctly completed words out of the twenty words.

2.5. Experiment Procedure. In this study, all participants were randomly allocated to all four conditions of 300 lx, 400 lx, 500 lx, and 1,000 lx through a repetitive measurement experiment design. Prior to each learning task per condition, participants underwent the two-minute dark and light adaptation periods, respectively. Over the next 10 minutes, participants learned about 20 nonsense syllables. After 10 minutes of the learning, the participants soon completed the working memory task. In the attention task, where performance was measured using a cognitive response measuring device, the number of correctly responded symbols in one minute was counted for use as a dependent variable. Subsequently, the participants returned to the experimental laboratory exactly 24 hours later and performed a long-term memory task of 20 items based on previous learning. The long-term memory was measured using the WFC task, and the proportion of the correctly recognized items out of the 20 items was obtained for use as a dependent variable. The specific experimental procedure is shown in Figure 5.

2.6. Statistical Analysis Method. Descriptive statistics were calculated for all the variables. Difference verification between attention and long-term memory according to the

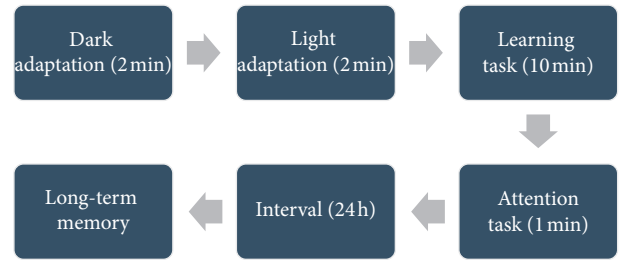

Figure 5: Experimental procedure.

Table 1: Descriptive statistics of attention and long-term memory according to illuminance of LED lighting.

Illuminance levels (lux) (lx)	Attention (a number of times)		Long-term memory (%)		N
	Mean	SD	Mean	SD	
300	16.22	3.78	43.33	19.10	18
400	17.50	5.54	58.06	22.57	18
500	18.00	5.18	48.89	20.33	18
1000	19.39	5.42	45.83	23.53	18

Table 2: ANOVA results of attention and long-term memory according to illuminance of LED lighting.

	DF	SS	MS	F	p
Attention	3	92.56	30.85	3.39	0.025*
Long-term memory	3	2234.72	744.91	3.21	0.031*

* $p < 0.05$.

illuminance of LED lighting was made through a repeated measure ANOVA through SPSS 20.0 (SPSS Inc., Chicago, IL, USA). Post hoc analysis was performed using the LSD method. Significance was defined as $p < 0.05$.

3. Result and Discussion

The descriptive statistics of attention and long-term memory according to illuminance conditions are shown in Table 1. The mean score for attention was the highest (at 19.39) in the 1000 lx condition and the lowest (at 16.22) in the 300 lx. However, the mean recognition rate for long-term memory was the highest (at 58.06%) in the 400 lx condition and the lowest (at 43.33%) in the 300 lx condition.

ANOVA was performed to verify whether the attention and long-term memory were significantly different according to the illuminance level. As shown in Table 2, the experimental results showed that there was a statistically significant difference at 95% confidence level in both attention ($F = 3.39$, $p = 0.025$) and long-term memory ($F = 3.21$, $p = 0.031$).

After this, the post hoc test was conducted to specifically find out the difference according to the illuminance level. The test results showed that there was a statistically significant difference in attention between 300 lx and 1000 lx conditions (mean difference = −3.17, $p = 0.012$). The result

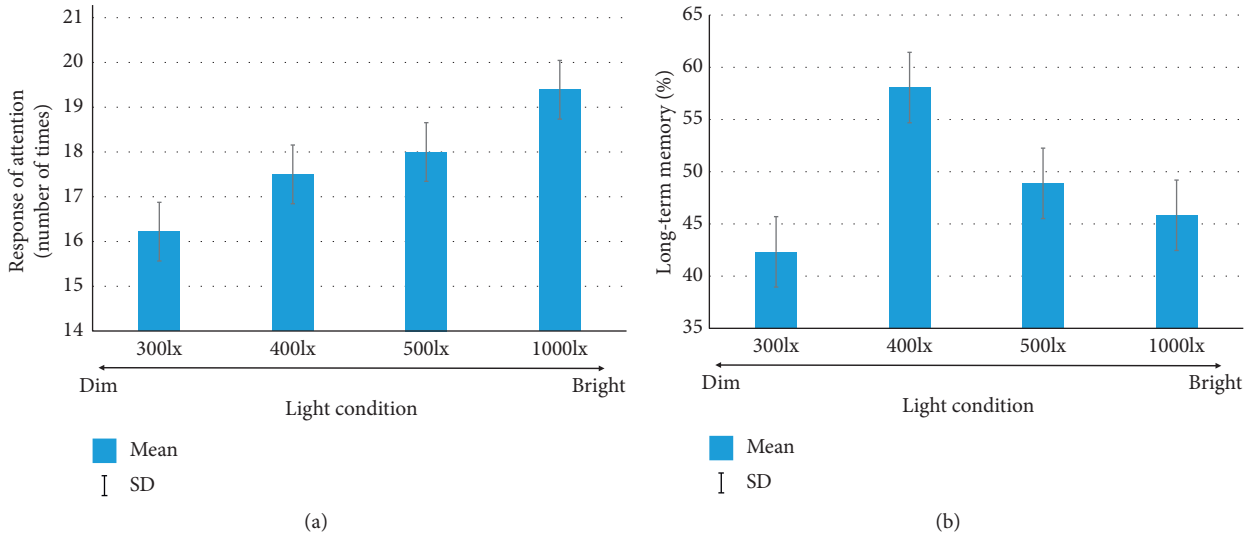

Figure 6: Difference between attention (a) and long-term memory (b) according to illuminance of LED lighting.

suggests that attention functions the best in the relatively high illuminance level of the 1000 lx condition and the worst in the lowest level of the 300 lx. This result is consistent with the studies by Smolder and Smolder [9] and Rüger et al. [11] that attention is excellent under bright light conditions.

On the other hand, the post hoc analysis results of long-term memory showed statistically significant differences between the 300 lx condition and the 400 lx condition (mean difference = –14.72, $p = 0.014$) and between the 400 lx condition and the 1000 lx condition (mean difference = 12.22, $p = 0.011$). The result suggests that the recognition rate for long-term memory is the best at 400 lx, followed by the order of 500 lx, 1000 lx, and 300 lx. This result is consistent with a study by Jung et al. [8] that long-term memory is superior in 400 lx relatively dim condition.

In summary, as shown in Figure 6, attention tended to be linearly activated as the illuminance increased, whereas long-term memory showed the lowest performance at 300 lx, the highest performance at 400 lx, and the inverted U shape, which progressively decreased performance.

4. Conclusion

The purpose of this study was to supplement the limitations of the existing studies, to reverify the existing studies' results that the long-term memory was the best at 400 lx, and to find out the optimal illuminance level at the same time. In addition, the study showed that long-term memory performed the best at 400 lx when compared with 300 lx, 500 lx, and 1,000 lx conditions. These results support Jung et al.'s [8] finding that working memory is excellent at 400 lx. Retrieval of long-term memory was the lowest at 300 lx and then steeply inclined to 400 lx, followed by a gradual decline as illuminance further increased. And the attention showed the lowest performance at 300 lx, which is the darkest condition in this experiment, and the attention was also linearly activated as the illuminance became bright. These results support previous studies that have previously addressed the relationship between light and attention. However, the fact that attention is excellent in bright light does not mean that bright light conditions are always good for cognitive performance. In this experiment, long-term memory retrieval was the best at 400 lx apart from light and darkness of light. Rather, the long-term memory retrieval at 1,000 lx condition, which is the best condition for the performance of attention, was not significantly better than the 400 lx condition. These results suggest that the optimized illuminance for memory should be considered separately from attention and long-term memory. Attention is activated as the light becomes brighter, but long-term memory is the most active near 400 lx. And, it can be concluded that 300 lx illuminance condition in attention and long-term memory is the worst condition because this illuminance shows the poorest performance and retrieval. In addition, this study can provide an issue that attention and long-term memory may differ in the active process. This is because the attention and long-term memory are activated differently according to the illuminance of the LED lighting. This should be verified through further studies.

This study is meaningful in that it clarified the difference by verifying the effect of illuminance, especially LED lighting, on attention and long-term memory more clearly and systematically. In addition, this study is significant in that it suggested optimized illuminance of attention and long-term memory; attention is the best at 1000 lx, a relatively bright light condition, and long-term memory is the best at 400 lx condition.

Data Availability

The data used to support the findings of this study are included within the supplementary information file.

Conflicts of Interest

The authors declare that they have no conflicts of interest.

Acknowledgments

This work was supported by the research grant of the Kongju National University in 2018.

Supplementary Materials

Attention and long-term memory data for each illuminance condition. Attention is the number of successful attention tasks in one minute, and long-term memory is the percentage of successful retrieval tasks. (*Supplementary Materials*)

References

[1] C. Cajochen, "Alerting effects of light," *Sleep Medicine Reviews*, vol. 11, no. 6, pp. 453–464, 2007.

[2] S. L. Chellappa, M. C. M. Gordijn, and C. Cajochen, "Can light make us bright? Effects of light on cognition and sleep," *Progress in Brain Research*, vol. 190, pp. 119–133, 2011.

[3] C. Cajochen, J. M. Zeitzer, C. A. Czeisler, and D.-J. Dijk, "Dose-response relationship for light intensity and ocular and electroencephalographic correlates of human alertness," *Behavioural Brain Research*, vol. 115, no. 1, pp. 75–83, 2000.

[4] A.-M. Chang, N. Santhi, M. St Hilaire et al., "Human responses to bright light of different durations," *The Journal of Physiology*, vol. 590, no. 13, pp. 3103–3112, 2012.

[5] L. M. Huiberts, K. C. H. J. Smolders, and Y. A. W. de Kort, "Shining light on memory: effects of bright light on working memory performance," *Behavioural Brain Research*, vol. 294, pp. 234–245, 2015.

[6] P. Badia, B. Myers, M. Boecker, and J. Culpepper, "Bright light effects on body temperature, alertness, EEG and behavior," *Physiology & Behavior*, vol. 50, no. 3, pp. 582–588, 1991.

[7] B. L. Myers and P. Badia, "Immediate effects of different light intensities on body temperature and alertness," *Physiology & Behavior*, vol. 54, no. 1, pp. 199–202, 1993.

[8] H.-C. Jung, J.-H. Kim, and C.-W. Lee, "The effect of the illuminance of light emitting diode (LED) lamps on long-term memory," *Displays*, vol. 49, pp. 1–5, 2017.

[9] K. C. H. J. Smolders and Y. A. W. de Kort, "Bright light and mental fatigue: effects on alertness, vitality, performance and physiological arousal," *Journal of Environmental Psychology*, vol. 39, pp. 77–91, 2014.

[10] K. C. H. J. Smolders, Y. A. W. de Kort, and P. J. M. Cluitmans, "A higher illuminance induces alertness even during office hours: findings on subjective measures, task performance and heart rate measures," *Physiology & Behavior*, vol. 107, no. 1, pp. 7–16, 2012.

[11] M. Rüger, M. C. M. Gordijn, D. G. M. Beersma, B. de Vries, and S. Daan, "Time-of-day-dependent effects of bright light exposure on human psychophysiology: comparison of daytime and nighttime exposure," *American Journal of Physiology*, vol. 290, no. 5, pp. 1413–1420, 2006.

[12] V. Kretschmer, K.-H. Schmidt, and B. Griefahn, "Bright light effects on working memory, sustained attention and concentration of elderly night shift workers," *Lighting Research & Technology*, vol. 44, no. 3, pp. 316–333, 2012.

[13] S. S. Campbell and D. Dawson, "Enhancement of nighttime alertness and performance with bright ambient light," *Physiology & Behavior*, vol. 48, no. 2, pp. 317–320, 1990.

[14] R. C. Atkinson and R. M. Shiffrin, "Human memory: a proposed system and its control processes," *Psychology of Learning and Motivation*, vol. 2, pp. 89–195, 1968.

[15] E. Tulving, D. L. Schacter, and H. A. Stark, "Priming effects in word-fragment completion are independent of recognition memory," *Journal of Experimental Psychology: Learning, Memory, and Cognition*, vol. 8, no. 4, pp. 336–342, 1982.

[16] D. L. Nelson, J. J. Canas, M. T. Bajo, and P. D. Keelean, "Comparing word fragment completion and cued recall with letter cues," *Journal of Experimental Psychology: Learning, Memory, and Cognition*, vol. 13, no. 4, pp. 542–552, 1987.

[17] M. J. Soler, J. C. Ruiz, M. Vargas, C. Dasí, and I. Fuentes, "Perceptual priming in schizophrenia evaluated by word fragment and word stem completion," *Psychiatry Research*, vol. 190, no. 2-3, pp. 167–171, 2011.

Hindawi
International Journal of Optics
Volume 2020, Article ID 1519205, 8 pages
https://doi.org/10.1155/2020/1519205

Research Article

An Intelligent Model for Facial Skin Colour Detection

Chih-Huang Yen, Pin-Yuan Huang, and Po-Kai Yang

Minnan Normal University, Zhangzhou City, Fujian, China

Correspondence should be addressed to Chih-Huang Yen; jordan_yan@hotmail.com

Received 30 October 2019; Revised 29 January 2020; Accepted 3 February 2020; Published 17 March 2020

Guest Editor: Cheng-Mu Tsai

There is little research on the facial colour; for example, choice of cosmetics usually was focused on fashion or impulse purchasing. People never try to make right decision with facial colour. Meanwhile, facial colour can be also a method for health or disease prevention. This research puts forward one set of intelligent skin colour collection method based on human facial identification. Firstly, it adopts colour photos on the facial part and then implements facial position setting of the face in the image through FACE^{++} as the human facial identification result. Also, it finds out the human face collection skin colour point through facial features of the human face. The author created an SCE program to collect facial colour by each photo, and established a hypothesis that uses minima captured points assumption to calculate efficiently. Secondly, it implements assumption demonstration through the Taguchi method of quality improvement, which optimized six point skin acquisition point and uses average to calculate the representative skin colour on the facial part. It is completed through the Gaussian distribution standard difference and CIE 2000 colour difference formula and uses this related theory to construct the optimized program FaceRGB. This study can be popularized to cosmetics purchasing and expand to analysis of the facial group after big data are applied. The intelligent model can quickly and efficiently to capture skin colour; it will be the basic work for the future fashion application with big data.

1. Introduction

Many studies on skin colour focus on face recognition or try to determine the typology of people [1]. However, the cosmetic market may need to assist people in finding the right make-up colours for different conditions. However, determining a person's skin colour is also a large issue in cosmetic research. The main purpose of this study is to use females as an example to determine colour modes using an innovative method to extract features.

1.1. Skin Color Collection. There are many relevant software of screen collecting color, such as Just Color Picker, ColorPic, and ColorSPY to expert mapping software Photoshop; all have functions of collecting image and screen website color, merits of software such as Just Color Picker and ColorPic except to support color codes such as HTML, RGB, HEX, HSB/HSV, HSL, HSL(255), and HSL(240), even it provides simple palette tools, which can make us manually make the desired colors. Photoshop uses graphic expression to convey dye absorption and makes function of color filling, which indicates digitalized collected color and makes more users quickly get their desired referential color; although it is quick and convenient, it does not represent that the used software can precisely collect color; this is related to the used software in market which usually makes collection by pixel, which indicates that the chosen image area is not large-scale visual color seen by people, so choosing color does not mean the representative color of this image. Hsiao et al. put forward fuzzy relation matrix calculation program of the fuzzy method to implement; the aim lies in reducing color and converting image into color and chooses representative color of this area, which uses related concept of absorbing image color [1–3].

Soriano et al. put forward that skin color indicates different colors under different environments; scholars record skin color trace by using a digital camera and present color range of skin color by skin color space, establishment of skin color point will be affected by distance of human eyes

seeing image skin color by establishing image skin color point, which indicates perception of human eyes is color of even skin color [4].

1.2. Outline of This Study. The purpose of this research mainly focuses on the facial skin colour; this is the extensive research based on human face identification, suppose image human face detection can use the minimum colour point as representative skin colour symbol, and through calculation of skin colour model and Taguchi method, it can minimize the colour point to 6 point and has representativeness. This application can make accumulation and calculation of plenty of data in the future, and it can be the base of big data analysis and expert system establishment for human skin colour. Figure 1 describes research structure and process.

2. Literature Review

2.1. RGB and CIELAB Conversions. Since RGB colour models are device-dependent, there is no simple formula for conversion between RGB values and $L^*a^*b^*$. The RGB values must be transformed via a specific absolute colour space. This adjustment will be device-dependent, but the values resulting from the transform will be device-independent. After a device-dependent RGB colour space is characterized, it becomes device-independent. In the calculation of sRGB from CIE, XYZ is a linear transformation, which may be performed by a matrix multiplication. Referring to equations (1) and (2), it presents that these linear RGB values are not the final result as they have not been adjusted for the gamma correction. sRGB was designed to reflect a typical real-world monitor with a gamma of 2.2, and the following formula transforms the linear RGB values into sRGB. Let C_{linear} be R_{linear}, G_{linear}, or B_{linear}, and C_{srgb} be R_{srgb}, G_{srgb}, or B_{srgb}. The sRGB component values R_{srgb}, G_{srgb}, and B_{srgb} are in the range 0 to 1 (a range of 0 to 255 can simply be divided by 255.0).

$$C_{\text{linear}} = \begin{cases} \dfrac{C_{\text{srgb}}}{12.92}, & C_{\text{srgb}} \le 0.04045, \\ \left(\dfrac{C_{\text{srgb}} + a}{1 + a}\right)^{2.4}, & C_{\text{srgb}} > 0.04045, \end{cases} \tag{1}$$

where $a = 0.055$ and C is R, G, or B.

It is followed by a matrix multiplication of the linear values to get XYZ:

$$\begin{bmatrix} X \\ Y \\ Z \end{bmatrix} = \begin{bmatrix} 0.4124 & 0.3576 & 0.1805 \\ 0.2126 & 0.7152 & 0.0722 \\ 0.0193 & 0.1192 & 0.9505 \end{bmatrix} \begin{bmatrix} R_{\text{linear}} \\ G_{\text{linear}} \\ B_{\text{linear}} \end{bmatrix}. \tag{2}$$

These gamma-corrected values are in the range 0 to 1. If values in the range 0 to 255 are required, the values are usually clipped to the 0 to 1 range. This clipping can be done before or after this gamma calculation [5].

2.2. Taguchi Method. The Taguchi method is used to make the designed product to have stable quality and small fluctuation and makes the production process insensitive to every kind of noise. In the product design process, it uses relations of quality, cost, and profit to develop high-quality product under condition of low cost. The Taguchi method thinks the profit of product development can use internal profit of enterprise and social loss to measure, enterprise internal profit indicates low cost under condition with the same functions, and social profit uses effect on human after product entering consumption field as the measurement index. This research uses the Taguchi method, and its main aim is to find out the optimization of skin colour point because point distribution has many probabilities, and it can find out the optimal point model through calculation of the Taguchi method.

Taguchi's designs aimed to allow greater understanding of variation than a lot of the traditional designs from the analysis of variance. Taguchi contended that conventional sampling is inadequate here as there is no way of obtaining a random sample of future conditions. In Fisher's design of experiments and analysis of variance, experiments aim to reduce the influence of nuisance factors to allow comparisons of the mean treatment effects [6]. Variation becomes even more central in Taguchi's thinking. The Taguchi approach provides more complete interaction information than typical fractional factorial designs that its adherents claim. Followers of Taguchi argue that the designs offer rapid results and that interactions can be eliminated by proper choice of quality characteristics. However, a "confirmation experiment" offers protection against any residual interactions. If the quality characteristic represents the energy transformation of the system, then the "likelihood" of control factor-by-control factor interactions is greatly reduced, since "energy" is "additive" [7].

2.3. Ellipsolid Skin-Colour Model. Zeng and Luo conducted the studies in human skin colour luminance dependence cluster shape discussed in the Lab colour space. The cluster of skin colours may be approximated using an elliptical shape [8]. Let $X1, \ldots, Xn$ be distinctive colours (a vector with two or three coordinates) of a skin colour training data set and $f(X\_i) = f\_i(i = 1, \ldots, n)$ be the occurrence counts of a colour, Xi. An elliptical boundary model $\Phi(X) = (X, \Psi, \Lambda)$ is defined as

$$\Phi(X) = [X - \Psi]^T \Lambda^{-1} [X - \Psi], \tag{3}$$

where Ψ and Λ are given by

$$\Psi = \frac{1}{n} \sum_{i=1}^{n} X_i, \tag{4}$$

$$\Lambda = \frac{1}{n} \sum_{i=1}^{n} f_i (X_i - \mu)(X_i - \mu)^T, \tag{5}$$

where $N = (1/n) \sum_{i=1}^{n} f_i$ is the total number of occurrences in a training data set and $\mu = (1/n) \sum_{i=1}^{n} f_i X_i$ is the mean of colour vectors. To consider the lightness dependency of the shape of skin cluster, the cluster of skin colours in a lightness-chrominance colour space may be modeled with

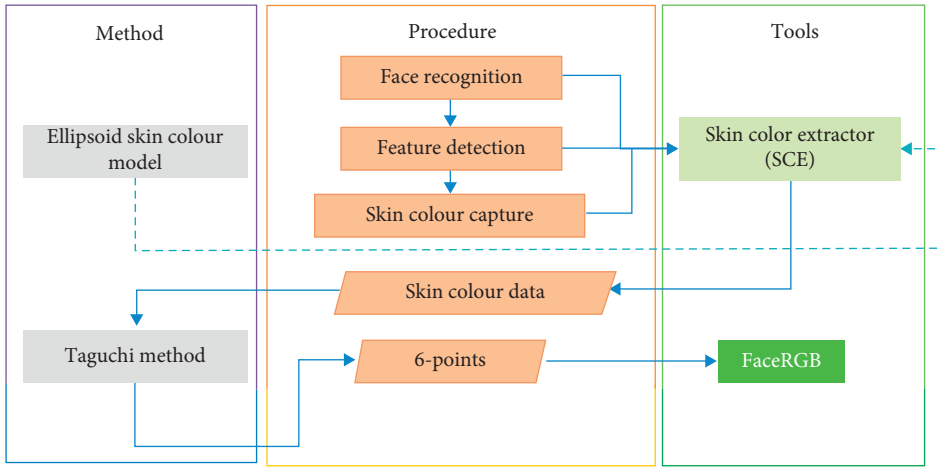

Figure 1: From Ellipsolid theory, make the SCE program to detect facial colour by each photo; Through the Taguchi method, get the 6-points captured method and make FaceRGB.

an ellipsoid. In a three-dimensional (3D) colour space, X is expressed as

$$X = \begin{pmatrix} x \\ y \\ z \end{pmatrix}, \tag{6}$$

and Λ^{-1} is represented in a matrix form

$$\Lambda^{-1} = \begin{pmatrix} \lambda_{00} & \lambda_{01} & \lambda_{02} \\ \lambda_{10} & \lambda_{11} & \lambda_{12} \\ \lambda_{20} & \lambda_{21} & \lambda_{22} \end{pmatrix}. \tag{7}$$

$\Phi(x)$ in equation (3) can be reorganized as

$$\begin{aligned} \Phi(x,y,z) = {} & \lambda_{00}(x-x_0)^2 + (\lambda_{01}+\lambda_{10})(x-x_0)(y-y_0) \\ & + (\lambda_{02}+\lambda_{20})(x-x_0)(z-z_0) + \lambda_{11}(y-y_0)^2 \\ & + (\lambda_{12}+\lambda_{21})(y-y_0)(z-z_0) + \lambda_{22}(z-z_0)^2. \end{aligned} \tag{8}$$

According to equation (5),

$$\Lambda = \frac{1}{n}\sum_{I=1}^{N} f(x_i,y_i,z_i) \times \begin{pmatrix} (x_i-x_0)^2 (x_i-x_0)(y_i-y_0) (x_i-x_0)(z_i-z_0) \\ (x_i-x_0)(y_i-y_0) (y_i-y_0)^2 (y_i-y_0)(z_i-z_0) \\ (x_i-x_0)(z_i-z_0) (y_i-y_0)(z_i-z_0) (z_i-z_0)^2 \end{pmatrix}. \tag{9}$$

Comparing equations (8) and (9), $\lambda_{01} = \lambda_{10}$ and $\lambda_{21} = \lambda_{12}$ The ellipsoid function (12) can be written as

$$\begin{aligned} \Phi(x,y,z) = {} & u_0(x-x_0)^2 + u_1(x-x_0)(y-y_0) \\ & + u_2(y-y_0)^2 + u_3(x-x_0)(z-z_0) \\ & + u_4(y-y_0)(z-z_0) + u_5(z-z_0)^2, \end{aligned} \tag{10}$$

where $u_0 = \lambda_{00}$, $u_1 = \lambda_{01} + \lambda_{10}$, $u_2 = \lambda_{11}$, $u_3 = \lambda_{02} + \lambda_{20}$, $u_4 = \lambda_{12} + \lambda_{21}$, and $u_5 = \lambda_{22}$.

$$\begin{aligned} \Phi = {} & \lambda_{00}(r-r_0)^2 + (\lambda_{01}+\lambda_{10})(r-r_0)(g-g_0) \\ & + (\lambda_{02}+\lambda_{20})(r-r_0)(b-b_0) + \lambda_{11}(g-g_0)^2 \\ & + (\lambda_{12}+\lambda_{21})(g-g_0)(b-b_0) + \lambda_{22}(b-b_0)^2, \end{aligned} \tag{11}$$

$$\begin{aligned} \Phi(r,g,b) = {} & u_0(r-r_0)^2 + u_1(r-r_0)(g-g_0) + u_2(g-g_0)^2 \\ & + u_3(r-r_0)(b-b_0) + u_4(g-g_0)(b-b_0) \\ & + u_5(b-b_0)^2 = \rho. \end{aligned} \tag{12}$$

3. Implementation Method

FOn the basis of human face identification, it uses characteristic point to make setting of the relative position, applies skin colour ellipse model and CNN of human face identification, and uses Java program to compile skin colour extractor, and its short form is SCE.

3.1. The Instruction Operation for Skin Colour Extractor (SCE). Figure 2 is the operation instruction of SCE, click (1) to open file, insert file, will see (2) figure display area indicates this file image and (3) file name, click (4) Detect Feature option on button area, image will automatically generate blue line, which indicates it has detected colour point of right cheek of human, left cheek, chin and forehead, it can input Need (6) on the left corner and finally push (7) Generate Result, which is indicted by Figure 3, which indicates (8) red collection point of input value, skin colour ellipse will display this (9) ellipse and input (10) L illumination to observe its changes, and stores some skin colour RGB and Office Excel file of Lab.

3.2. Taguchi Method Finds Optimization. Figure 4(a) indicates detection and positioning of human face is completed and connection line way by point to point. It makes division for the right eye corner, left eye corner, middle of the right eyebrow, left eyebrow, left mouth corner, and right mouth corner. Figure 4(b) may be the area of producing skin colour point, so Figure 4(c) indicates the probable colour point; this research sets every inserted photo is 300×600 pixel, of which the pixel value of connection line, the maximum point of pull-up radian is 50 point, equivalent connection line of point to point is 25 point, the minimum pull-up radian is 3 point. Radian direction is, respectively, represented by -1, 0, and 1. For example, the minimum pull-up position of the right mouth corner and left mouth corner will reach the chin of mouth and shadows, this radian direction cannot construct area block which conforms to skin colour, so it need not be listed into calculation.

Apply the Taguchi method to get the optimization from the distribution possibility for input in SCE. Figure 5 shows the study divides face into 4 blocks; they are, respectively, the forehead, left cheek, right cheek, and chin. It chooses proper factor as the design level. One block, respectively, has factors (radian and point number), it totally has 8 factors, 3 grades, so it chooses the L_{18} orthogonal table.

Based on the 4 areas defined, Table 1 shows the control factor table to clarify all parameters, and will follow the Taguchi method to do the test. It uses characteristics of orthogonal table to reduce test times from 4,374 times to 18 times, it greatly simplifies test times and calculates S/N proportion, standard difference, and average, it presents the result by inputting into the table, through conversion of the Taguchi method S/N proportion, which makes test data to conform to the additive model (addition characteristic), and calculates level effect of every factor, and gets factor reaction table of quality characteristic, which is indicated in Table 2.

From action table, we can clearly see the effect result of quality characteristic because S/N proportion belongs to projection characteristics, and it can easily find the optimized result of every group in the table. Firstly, in the part of Significant in Table 3, can see B D F H, it is yes, and representative has reaction and effect. They are respectively: optimal combination of collection point is {BFHD}. It can also find factor significance sequence under quality characteristic, the optimized efficiency is $B > F > H > D$, referred factor characteristic result figure from Tables 2 and 3. Fraction of Rank, the first one is B, ranging from -4~1.7, the range value of carry number is about 6, so the optimal collection point is 6 point.

4. Result and Discussion

From the analysis result, it is found that importance sequence will change according to the quality characteristic, and it is mainly because the Taguchi method belongs to the optimal method of single quality characteristic and then uses this to program correction base, which can make program of this research quickly calculate the optimized result of skin colour collection.

4.1. Verification for 6 Points to Detect Facial Color. In the course of the study, it is assumed that the typical image processing software (eg., Photoshop and CorelDraw) is as shown in different steps in Figure 6. There is a step-by-step procedure, Figure 6(a), which means that the file has been read. As for Figure 6(b), it shows that the background has been cut out and completely ensured the face shape. User could capture the skin colour manually. Most of the positions are decided relying on the intuition. So, Figure 6(c) presents the 6 point on the face, and the results of colour detected would be shown as the number by each in Figure 6(d). Then, the average values of the 6 data could be calculated as shown in Figure 6(e). The flow chart is the foundation of the FaceRGB program.

Six points may have come from part of the hair or shadow, since they are in the range of identification colour values but with different variations of brightness. For debugging efficiently, beside the limited value, the Gaussian distribution concept and standard deviation of the outliers are also removed. Figure 7 describes how to define and find the outlier from six points. The procedure of the FaceRGB program is as follows.

4.2. FaceRGB Program. The procedure of the FaceRGB program is as follows.

(1) Calculate Faceskin data. All points of the average distance to FaceLABavg (ΔEavg) and standard deviation σ

(2) Outlier is far from the distance of FaceLABavg (Distanceavg + 2σ)

(3) Refer to equation (13). According to CIE2000 [9], the formula is

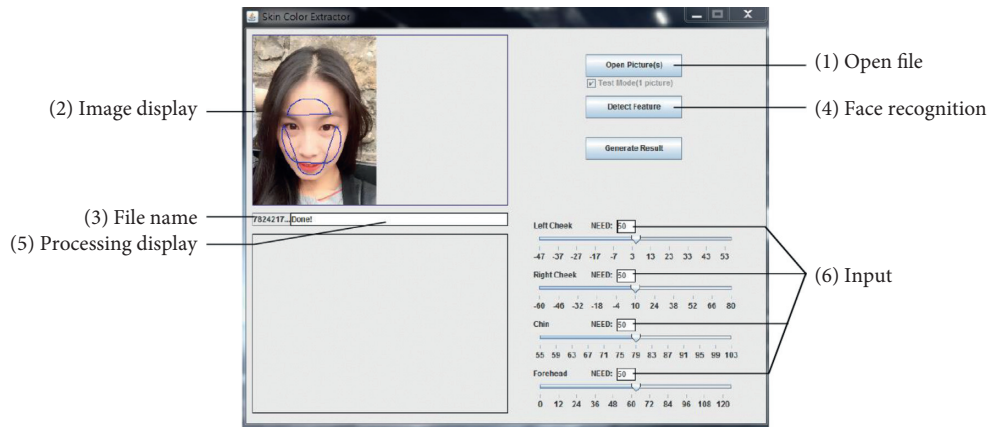

Figure 2: Instruction for SCE operation.

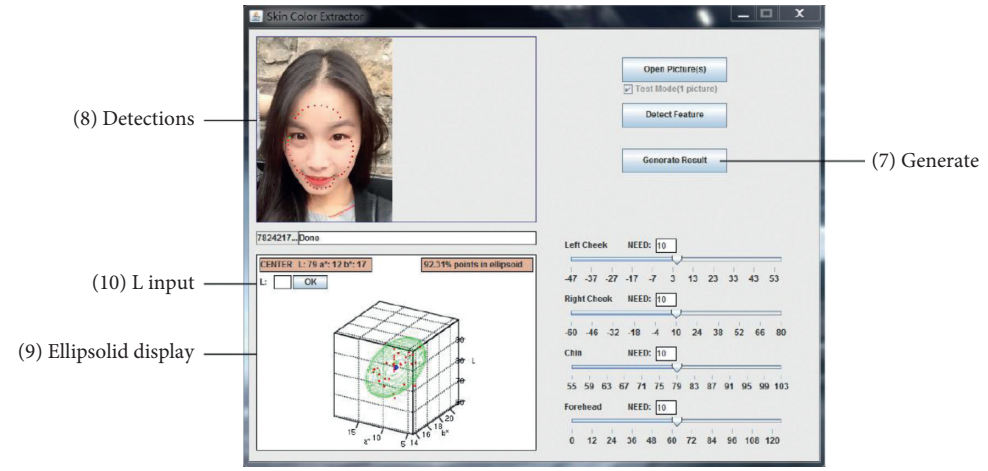

Figure 3: Processing by single image.

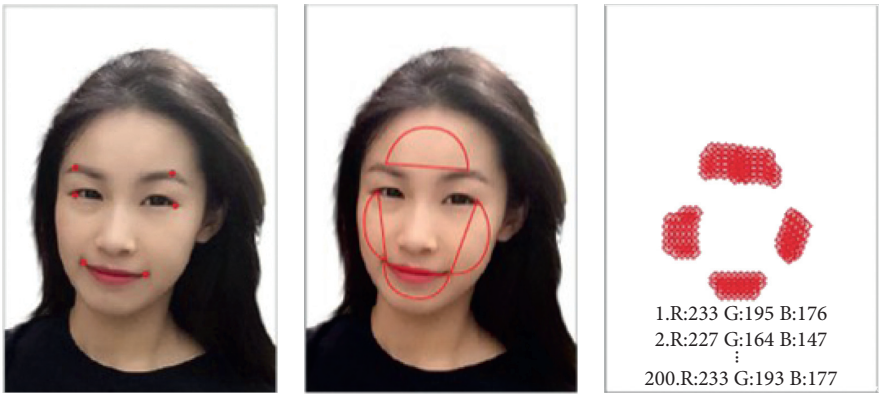

Figure 4: The distribution possibility for input in SCE.

$$\Delta E_{00}^{*} = \sqrt{\left(\frac{\Delta \acute{L}}{k_L S_L}\right)^2 + \left(\frac{\Delta \acute{C}}{k_C S_C}\right)^2 + \left(\frac{\Delta \acute{H}}{k_H S_H}\right)^2 + R_T \frac{\Delta \acute{C}}{k_C S_C} \frac{\Delta \acute{H}}{k_H S_H}}. \tag{13}$$

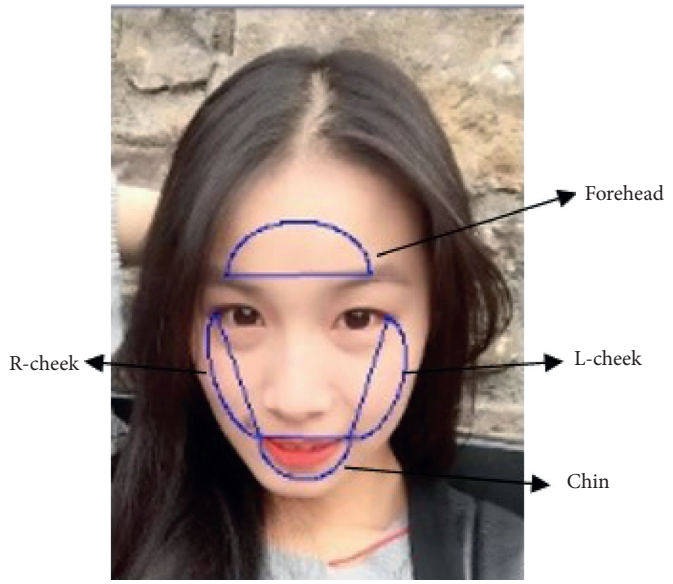

Figure 5: The distribution possibility for input in SCE.

Table 1: A control factor table that may be generated for the colour detection.

Level of control factors		Level	Level 1	Level 2	Level 3
Chin	Radian	A	−1	0	
	Points	B	3	25	50
R-cheek	Radian	C	−1	0	+1
	Points	D	3	25	50
L-cheek	Radian	E	−1	0	+1
	Points	F	3	25	50
Forehead	Radian	G	−1	0	+1
	Points	H	3	25	50

Table 2: Factor reaction table.

Exp	*A*	*B*	*C*	*D*	*E*	*F*	*G*	*H*	*P*1	*P*2	*P*3	Ave.	*S*	*S*/*N*
1	1	1	1	1	1	1	1	1	98	97.5	98	97.83	0.289	50.6
2	1	1	2	2	2	2	2	2	94	93.8	94.2	94	0.2	53.4
3	1	1	3	3	3	3	3	3	95	94.5	96.2	95.23	0.874	40.7
4	1	2	1	1	2	2	3	3	96.7	96	95	95.9	0.854	41
5	1	2	2	2	3	3	1	1	94	95	94	94.33	0.577	44.3
6	1	2	3	3	1	1	2	2	94.4	94	94.5	94.3	0.265	51
7	1	3	1	2	1	3	2	3	96.2	96	96.5	96.23	0.252	51.7
8	1	3	2	3	2	1	3	1	96	96.5	96	96.17	0.289	50.5
9	1	3	3	1	3	2	1	2	96	96	95	95.67	0.577	44.4
10	2	1	1	3	3	2	2	1	95.4	95.4	96.7	95.83	0.751	42.1
11	2	1	2	1	1	3	3	2	95	94.5	95.2	94.9	0.361	48.4
12	2	1	3	2	2	1	1	3	96	95.1	96	95.7	0.52	45.3
13	2	2	1	2	3	1	3	2	95.4	94	96.1	95.17	1.069	39
14	2	2	2	3	1	2	1	3	96	94	95	95	1	39.6
15	2	2	3	1	2	3	2	1	95.1	96.7	96	95.93	0.802	41.6
16	2	3	1	3	2	3	1	2	95	94.5	95.8	95.1	0.656	43.2
17	2	3	2	1	3	1	2	3	94.5	96.6	96.5	95.87	1.185	38.2
18	2	3	3	2	1	2	3	1	96.7	94.5	96	95.73	1.124	38.6

(4) Delete the outlier from the six points

The FaceRGB program is described individually as follows:

(1) Open the program, the title indicates FaceRGB.

(2) When the file has been read, the image will appear in this picture window; it includes big data read or

Table 3: Factor characteristics result table.

	A	B	C	D	E	F	G	H
Level 1	44.0	46.8	44.6	44.0	46.6	46.0	44.6	46.0
Level 2	41.8	42.7	45.7	42.0	45.8	43.2	44.0	44.0
Level 3		44.4	43.6	41.0	45.0	42.0	43.0	42.7
$E^{1\text{-}2}$	−2.2	−4.0	1.1	−2.0	−0.8	−2.8	−0.6	−2.0
$E^{2\text{-}3}$		1.7	−2.1	−1.0	−0.8	−1.2	−1.0	−1.3
Range	2.2	5.7	2.2	3.0	1.6	4.0	1.6	3.3
Rank	5	1	6	4	7	2	8	3
Significant	No	Yes	No	Yes	No	Yes	No	Yes

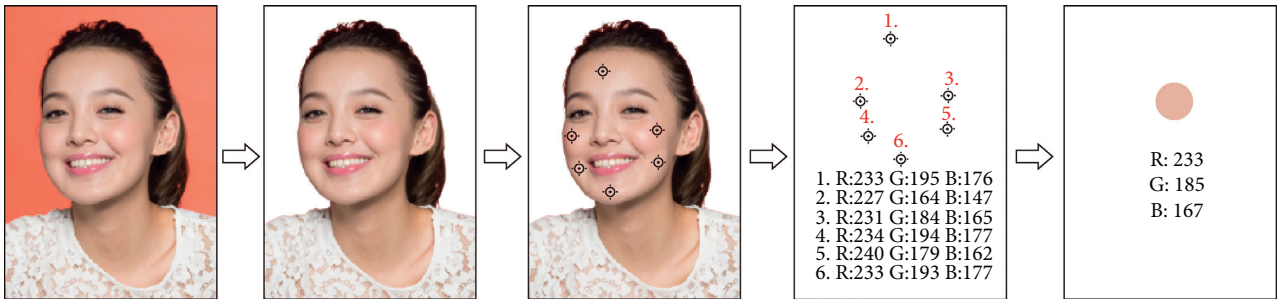

Figure 6: The traditional procedure to capture skin colour.

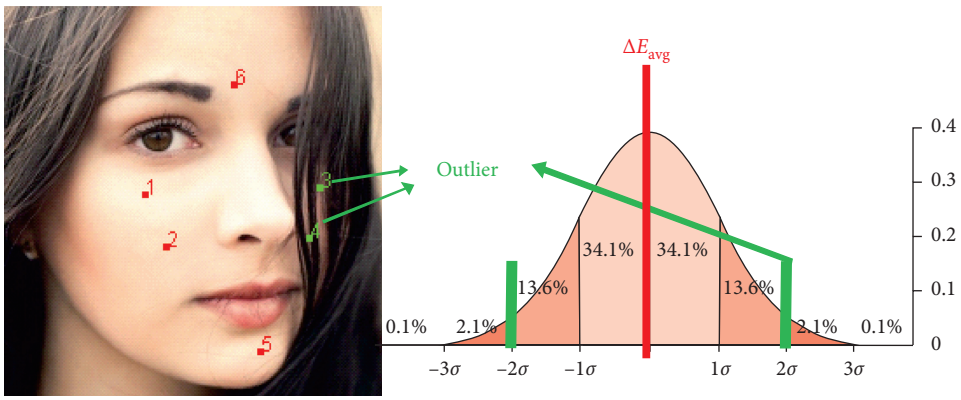

Figure 7: The Gaussian distribution concept and standard deviation.

operation. There is instant synchronization status presenting in the window.

(3) Spreadsheet progress strip windows, the situation will progress to the long schedule for a presentation to show they reached results.

(4) For big data, create four computation channels in the program, and it will be dealing with huge data in the same time. Figure 8 shows the situation as it is working.

(5) Option is designed to be read as a single image or input for only one time.

(6) This is a single image processing result, including the colour, RGB values, and LAB values. Figure 9 presents the example.

4.3. Conclusion. This research has created programs to detect the facial colour. They can calculate huge amount of data and even complicated issues by the intelligent method. This colour selecting method can be accumulated for calculating huge data. Therefore, trend for skin colour can be derived from the obtained data. The purpose of this study is to propose a model and procedure for the investigation. Moreover, the process is more important than the result. In addition, the study anticipates that this expert system could be applied into big data type and IOT (internet of things) in the future.

Users will gain their skin colour and the colour location of the face region, which can assist them to select the right colour to match their skin. With it, it will be easier for females to find out their skin colour grouping. Furthermore,

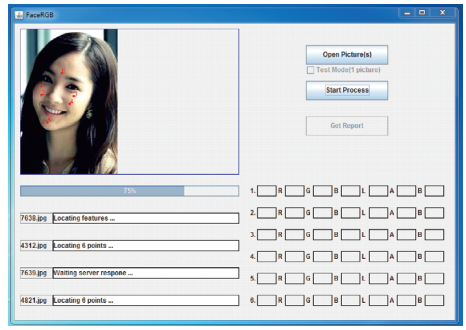

Figure 8: Processing with four computation channels.

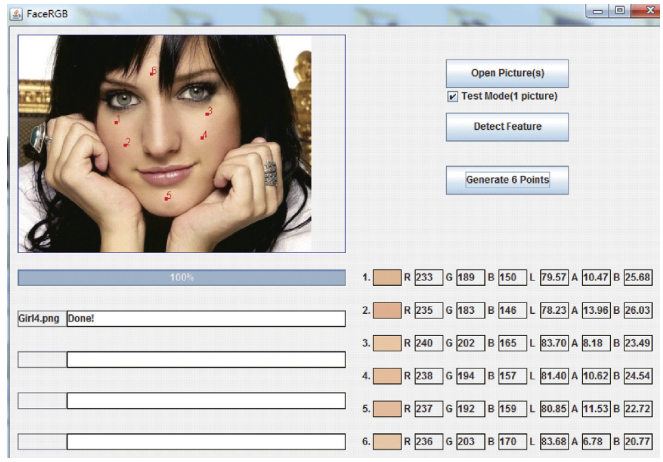

Figure 9: The result of FaceRGB from one image.

after colour harmony and applied aesthetics, every result can be the fashion trend in cosmetics. The expert system can be implemented to develop colour cosmetics; besides, it can be made in the future. Finally, if this system can be applied in the make-up market, it will make a considerable contribution and value.

Data Availability

The optimization data (through the Taguchi Method) used to support the findings of this study are included within the article.

Conflicts of Interest

The authors declare that they have no conflicts of interest.

Acknowledgments

The authors are grateful to The Institute of Minnan Culture Innovation Design & Technology Research, Minnan Normal University, for supporting this research under Grant no. 2018ZDJ03010004.

References

[1] S.-W. Hsiao and C.-J. Tsai, "Transforming the natural colors of an image into product design: a computer-aided color planning system based on fuzzy pattern recognition," *Color Research & Application*, vol. 40, no. 6, pp. 612–625, 2015.

[2] S.-W. Hsiao, "A systematic method for color planning in product design," *Color Research & Application*, vol. 20, no. 3, pp. 191–205, 1995.

[3] S. W. Hsiao and M. S. Chang, "A semantic recognition-based approach for car's concept design," *International Journal of Vehicle Design*, vol. 18, pp. 53–82, 1997.

[4] M. Soriano, B. Martinkauppi, S. Huovinen, and M. Laaksonen, "Adaptive skin color modeling using the skin locus for selecting training pixels," *Pattern Recognition*, vol. 36, no. 3, pp. 681–690, 2003.

[5] P. Green, W. Lindsay, and M. Donald, *Colour Engineering: Achieving Device Independent Colour*, John Wiley & Sons, Hoboken, NJ, USA, 2002.

[6] R. H. Hardin and N. J. A. Sloane, "A new approach to the construction of optimal designs," *Journal of Statistical Planning and Inference*, vol. 37, no. 3, pp. 339–369, 1993.

[7] P. Friedrich, *Optimal Design of Experiments*, SIAM, Pittsburgh, PA, USA, 2006.

[8] H. Zeng and R. Luo, "Skin color modeling of digital photographic images," *Journal of Imaging Science and Technology*, vol. 55, no. 3, Article ID 030201, 2011.

[9] G. Sharma, W. Wu, and E. N. Dalal, "The CIEDE2000 color-difference formula: implementation notes, supplementary test data, and mathematical observations," *Color Research & Application*, vol. 30, no. 1, pp. 21–30, 2005.

Hindawi
International Journal of Optics
Volume 2020, Article ID 1370917, 13 pages
https://doi.org/10.1155/2020/1370917

Research Article

Optimal Lighting of Optical Devices for Oral Cavity

Chia Hung Yeh,[1] **Liang Gie Huang**,[1,2,3] **and Man Yee Chan**[2,4]

[1]*Department of Industrial Engineering and Enterprise Information, Tunghai University, Taichung City 407, Taiwan*
[2]*Department of Stomatology, Taichung Veterans General Hospital, Taichung City 407, Taiwan*
[3]*Department of Oral Hygiene, Hsin Sheng Junior College of Medical Care and Management, Taoyuan City 325, Taiwan*
[4]*School of Dentistry, College of Oral Medicine, Chung Shan Medical University, Taichung City 402, Taiwan*

Correspondence should be addressed to Chia Hung Yeh; chy@thu.edu.tw

Received 7 November 2019; Accepted 18 December 2019; Published 30 January 2020

Guest Editor: Cheng-Mu Tsai

Oral surgery mainly provides surgical scope illumination by doctors wearing headlamps, but there are still clinical restrictions on use. The limitations are (1) due to the angle of the head swing and the shadow of the visual field during the operation and (2) due to projection of the light source being worn on the doctor's head and the length of the wire, and the fiber-optic wire will affect the relative position of the surgical instrument and limit the scope of the doctor's activity. This study will focus on the development of oral lighting optical microstructure devices to solve and improve the abovementioned clinical use limitations. The production method is to make an oral lighting mold by 3D printing technology and use the polydimethylsiloxane (PDMS) of liquid silicone material to make an oral lighting device with mold casting technology. The results show that the optical simulation achieves the target light distribution by optimizing the three geometric reflection surfaces combined with the lens design by the optimization method, and the maximum illumination value can reach 5102 lux. According to the measurement results of mold casting technology, the average errors of the profile of the 3D printing finished product and the PDMS finished product of the oral device structure are about 1.4% and 16.9%, respectively. Because the contour of the PDMS finished product's error caused the light to shift by 0.5~3 mm distance, the light is still concentrated in the range of the tonsils, so this study can be defined as within the acceptable range of within 16.9% of the intra lighting error. The development of oral lighting devices in this study will reduce the burden on physicians in nonprofessional fields, reduce the time of surgery for patients to maintain the health of doctors, and rise the level of medical equipment to increase surgical safety.

1. Introduction

As the society's awareness of medical health, medical rehabilitation, green environmental protection, and energy conservation rises, the LED industry has become the focus of various professional fields. Among them, the LED light source is suitable for medical illumination because it meets the requirements of high reliability, long life, and low cost and is the best solid light source to replace the current halogen lamp, mercury lamp, and xenon lamp. In addition, the LED is small enough in size to form any geometric shape and any size of point, line, and surface. The light source can also be miniaturized. The LED is very suitable for medical lighting, and domestic LED medical lighting is becoming more common. It can be used in a wide range of applications, such as combing LED with surgical equipment in various operating rooms to develop its operating room-specific lighting devices, which is why LED lighting is expected to be widely used in the medical field.

This study is aimed at the illumination of the scope of the internal part of the oral cavity. At present, the surgical illumination of the internal oral cavity is mainly provided by the surgeon wearing a fiber-optic projection lamp, but there are still clinical restrictions on use. The main limitation is the scope of surgery. Lighting needs to be oscillated by the doctor's head to achieve better illumination range. The physician must focus on the surgical procedure and also control the angle of the light source. Therefore, the shadow

obstacle caused by the poor swing angle of the head or the dead angle of the visual field is often caused by the poor illumination of the surgical area, and the interference affects the operation. At present, most of the literature or patents focus on single use. According to the results of the literature, there are many methods for discussing oral lighting. For example, when using the principle of geometric reflection combined with photodynamic therapy (PDT) to treat the oral cavity, it is not necessary to cover the entire oral cavity to make the oral cavity evenly illuminated. The average illuminance produced was 50 mW/cm [1].

Another option is to use an oral lighting patch. One side of the patch is a light-transmissive layer, and the other side is viscous for fixing. There are two cavities between the two sides. The cavity was filled with a chemical substance, and the space in between has two chambers that need to be folded before use. The substance produces a chemical reaction that excites a chemical photoreaction and is emitted by the light-transmissive layer to achieve the function of oral lighting. However, this patent has safety concerns about the luminescence persistence being low and the chemical being at risk of leaking [2]. Part of the light generated by the light source illuminates the surface of the tooth by means of an optical conduit, and the other part of the light is guided by the reflector to a predetermined place. When the light is reflected from the surface of the tooth, the reflected light is received to form a shadow. However, the patent is more suitable for use in taking images. When used in surgery, the doctor needs to take the surgical instrument in one hand, and the other hand takes the product, which is inconvenient, and the product is large in size and easily interferes with the operation when used [3].

When an external light source is directed onto the light guide metal plate, the light is reflected inside the oral cavity to achieve the function of illumination. The disadvantages of this research device are poor light source efficiency and poor lighting performance [4]. The structure is designed as a U-shaped sheet, and a rectangular portion is, respectively, arranged on each of two ends of the U-shaped sheet; a plurality of LEDs are arranged on the side of each rectangular portion, and a power supply line is arranged at the closed end of the U-shaped sheet. This illuminating device has flexibility and also has the function of a mouth opener. This patent can be used for tonsillectomy, but the light supply is insufficient, the surgical field of view is reduced, and it does not provide tongue protection [5]. The oral lighting device developed by Isoite Medical Company from the United States can be used for illumination during dental examinations. However, if it is applied to the removal of tonsils, it will obscure the area of the tonsils inside the mouth and affect the operation. Therefore, it is not applicable [6]. The product launched by American Medical Company eBite, the buccal oral lighting device, has the function of illumination and can be used for illumination in dental and laryngological examinations. However, if used in tonsillectomy, the physician must hold the illumination device and the tongue fixation tool simultaneously. The appliance not only causes difficulty in operation but also affects the surgical field of view and thus is not suitable for use in oral surgery [7].

Based on the patents' literature above, it is found that the problem of obscuring shadows caused by the poor head swing angle or dead angle of view is seldom discussed. In view of this, the research will be discussed for the oral cavity with innovative design and optical simulation software analysis to develop oral lighting devices with high illumination.

With the development of various miniaturized processing technologies, in recent years, in addition to the requirements of high electro-optical transmission rate, high brightness, and longevity, the development of various optoelectronic device products also has the goal of power saving, energy saving, and miniaturization. Under this trend, the development of optical devices is also moving toward miniaturization, array, and integration, and low cost and high efficiency have become one of the research goals in this field. In order to achieve miniaturization of the system, micro-optical devices have become indispensable, and the importance of micro-optical systems has gradually increased, hoping to improve what conventional optical devices cannot achieve.

In terms of mass production of optical devices, the main production technology is mold casting, which can be used to manufacture glass and plastic materials. However, due to the low cost of plastic materials, the ease of processing complex devices, and the short processing time, many photovoltaic devices have been gradually replaced by plastic materials such as imaging lenses, illumination devices, projection lenses, and lens arrays. Different process methods will affect the structural characteristics of the entire microlens, which will affect its optical quality. For example, the radius of curvature of the lens will affect the size and and dimension; the surface roughness will affect the quality of the entire optical output.

This study will combine 3D printing technology with mold casting technology, hoping to use this novel process to partially replace the previous micro-optical device manufacturing technology. Among them, polydimethylsiloxane (PDMS) of liquid silicone material is often used to fabricate the micro-optical structure. In 2014, Liu et al. [8] produced a microlens array by a lithography process combined with a mold turning technique and a hot pressing method. The circular groove is made by the photoresist. The upper PDMS is formed into a circular arc surface by suction, and the UV glue is copied to form a convex spherical shape mold. The UV plastic mold is turned into a concave spherical surface with PDMS as a material, and finally a microlens array of a PC substrate is produced by hot pressing of PDMS. The situation in which the PDMS forms a concave curved surface is calculated and controlled in an analog manner. In 2007, Yang et al. [9] used a lithography process and combined it with microfluidic technology to make a cylindrical shape with double exposure, and then PDMS was used to spin coat the PDMS-tunable thin film wafer. The pressure that causes film undulation to change the contact angle was measured. The volume of the injected liquid and the measurement of the contact angle result are controlled, and the effect of changing the lens to the curvature is easily controlled. In 2006, Ren et al. [10] used PDMS polymer plastic

material as the elastic film, and rubber was used to seal the fluid. The pressure was applied to the rubber from the outside to make the upper PDMS film convex into a lens shape, and the change of the contour and the focal length was observed. In 2004, Jeong et al. [11] produced a curved lens that can be biconvex or biconcave with a lithography process and used PDMS rolled mold to obtain a microlens with a fixed curvature on one side; they completed the PDMS lens with one side curved and the other side swirled. A layer of PDMS film is applied to change the surface of the lens to a meniscus or biconvex shape by changing the volume of the liquid in the liquid lens. In 2003, Chronis et al. [12] used a lithography process to form a photoresist into a cylindrical shape and then flipped the PDMS microlens film. The microfluidic injection liquid filled the PDMS film, changing the volume of the hydraulic fluid to fine-tune the focal length using ANSYS software. The film was subjected to force deformation analysis to observe the shape change of the PDMS film and to explore the relationship between pressure, radius of curvature, and focal length.

According to the above literature, PDMS is a thermosetting elastomer material due to its material property, which has good tactile sensation and does not cause harm to the human body. It has better translucency, replication, and flexibility than general polymer thermoplastic polymerization. The product has better stability and heat resistance and has gradually become an indispensable material in medical supplies, diving equipment, and automobile and motorcycle industries. Therefore, this study uses PDMS as materials for oral lighting structural devices. The advantages of this process can reduce cost and production time, replacing expensive equipment, and mass production constraints. Therefore, measurement and experimentation are used to explore process results in this research process.

There are currently two types of 3D printed biocompatible materials on the market: Stratasys MED610 and Formlabs Form 2 Dental SG. These two materials are widely used in clinical medicine, but the two materials harden due to chemical reactions after molding and solidifying, which do not meet the design requirements of this study. Therefore, this study did not directly use 3D printed products to put into the oral cavity. In view of this, this research uses reverse engineering technology to make molds, pours PDMS materials into the molds, and finally obtains the finished product. Polydimethylsiloxane (PDMS) is a kind of high-molecular organosilicon compound, usually called organosilicon, which is inert, nontoxic, and nonflammable. PDMS is the most widely used silicon-based organic polymer material, which is used in microfluidic systems, caulks, lubricants, and contact lenses in biological microelectromechanical systems. PDMS in solid form is a silicone, nontoxic, hydrophobic, inert, nonflammable, and transparent elastomer. The manufacturing process of PDMS is simple and fast, the material cost is much lower than that of silicon wafers, and it has good light transmission, good biocompatibility, easy to join with many materials at room temperature, and structural flexibility caused by low Young's modulus. PDMS is a very safe substance. It does not react to the immune system and is not swallowed by cells. It does not breed bacteria or react with chemicals, so there are no commonly believed side effects. This safety data can be obtained from various manufacturers. At the same time, silicone rubber can be developed and produced for skin wounds, which can be used to protect wounds. It is a very safe material and is licensed by health authorities in various countries.

The original design of this study is mainly for the surgical auxiliary lighting of the tonsils to solve clinical problems, and it is not necessary to adjust the angle of the light while performing surgery. It is not intended to replace all headlights, but to design from the perspective of "auxiliary lighting." In addition to the auxiliary lighting for tonsil surgery, the auxiliary lighting device developed in this research can also be used in the following occasions: (1) operating room where headlights cannot be adjusted by hand and is susceptible to interference. (2) When the oral surgery is deep, the oropharynx and hypopharynx will have dead corners if the spreader cannot be opened enough. (3) Where the oral cavity has undergone radiation therapy or suffers from oral submucosal fibrosis, which prevents the oral cavity from opening.

2. Materials and Methods

The limitation of the research scope will be mainly for the removal of inflammation of the tonsils in the oral cavity. The main research focus is to design the oral lighting devices, explore the illuminance by optical simulation analysis, and obtain the prototype design parameters of the lighting devices to facilitate the subsequent process production, measurement analysis, and verification. The oral lighting device design and optical simulation analysis of the tonsil removal procedure are as follows: first, the oral lighting devices are constructed. Second, defining the relative position of the oral tonsil gland and the oral lighting element. Third, using optical simulation analysis to design high-illumination oral lighting devices. Fourth, the process of making the oral lighting devices and measurement verification.

2.1. Oral Lighting Structure Design. The structural design requirements of this study are based on the current state of clinical surgery and are set to meet the following requirements: (1) open the mouth to facilitate the doctor to perform surgery; (2) fix the tongue in order to avoid it interfering with the operation because if the tongue is lifted, it will block the sight; (3) add lighting function to help doctors avoid the lack of light during surgery; and (4) reduce the equipment required before surgery, such as oral spreaders, lighting equipment, tongue depressors, and other medical equipment. The oral lighting structure designed in this study (see Figure 1).

2.2. Define the Relative Position of the Tonsil and the Oral Lighting Devices. Figure 2 clearly shows the relative position of the tonsils and uvula in the oral cavity, that is, the lymphoid tissues located on both sides of the oropharynx. The most common medical problems encountered are

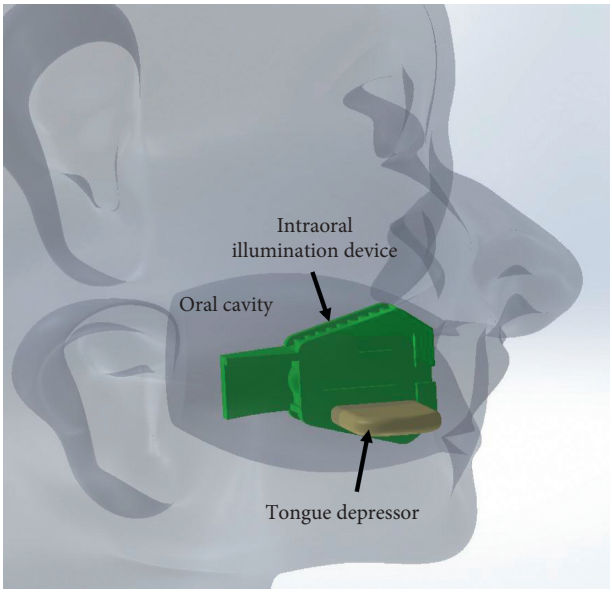

Figure 1: Oral lighting structure design schematic diagram.

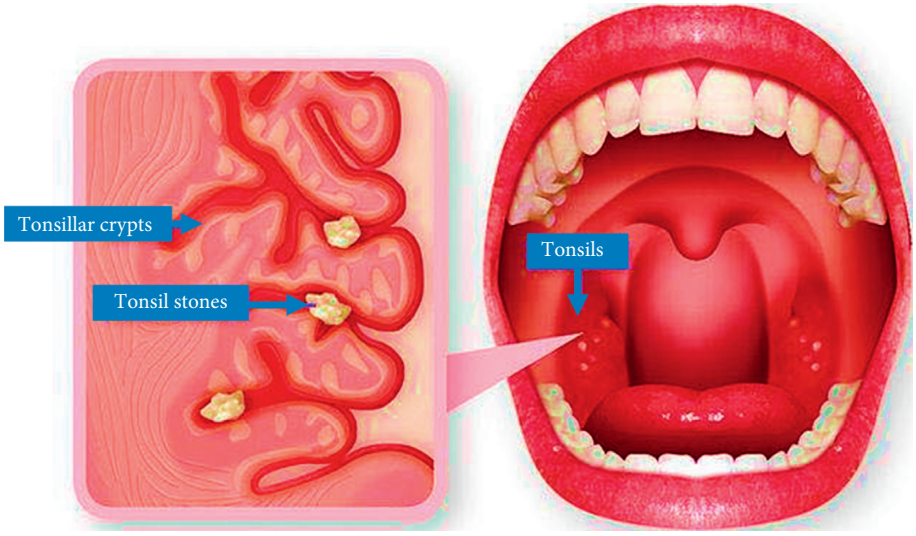

Figure 2: Location of the tonsil in the oral cavity.

obstructive hypertrophy or infection. Hypertrophy of the tonsils is often caused by increased immune activity. Hypertrophy itself is not a disease, but when the tonsils are obviously too large, it will lead to obstructive respiratory arrest; the surface of the tonsils can easily hide food debris, pathogenic bacteria, and so on, due to many glandular fossae that may cause infections. Generally, antibiotics will be used first. If there is a recurrent tonsil inflammatory disease, further surgery will be considered. In this study, the relative positional dimension of the light surface of the tonsil and the oral lighting structure is 20 mm × 15 mm × 30 mm (front × height × width) (see Figures 3 and 4). Focusing the light source on the tonsils, with cross emission provided by light sources on the left and right side of the tonsils, can prevent the doctor from reducing the brightness by blocking the light source during the operation. The definition of the relative position of the optical simulation in the oral cavity is as follows (see Figure 5).

2.3. Oral Illumination Specification. Illuminance is the luminous flux of visible light absorbed per unit area of the surface of the object, and the light used for the incident surface is in Lux. Every place with a different purpose of use should have its appropriate illumination to match the actual needs. This study will use the two commercially available products as a reference to set the illuminance target value. The first is ebite2 for dentistry, and the second is for surgical headless lamps. According to the two products, the first commercial product ebite2 [7] has an illumination range of

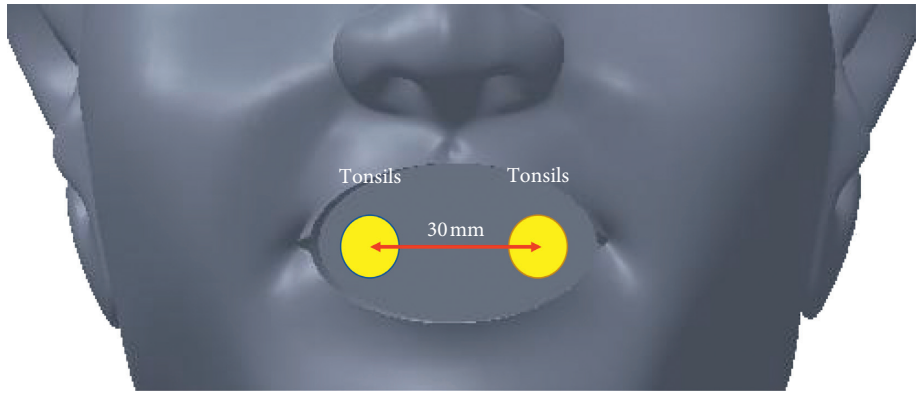

Figure 3: Schematic diagram of the definition of the tonsil in the oral cavity.

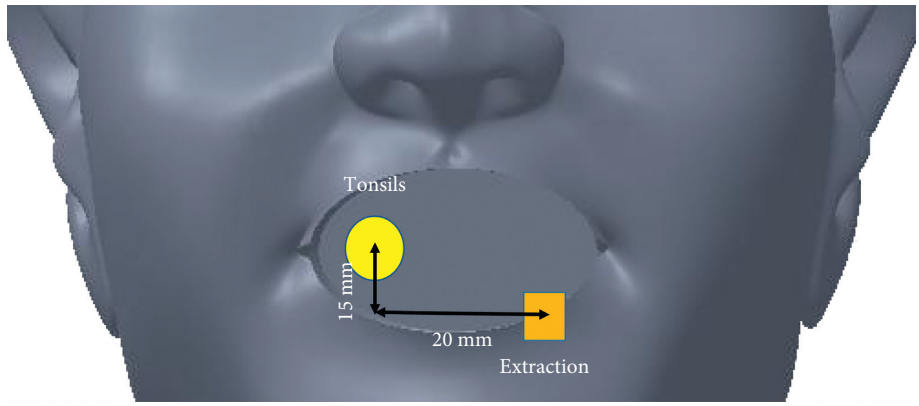

Figure 4: Schematic diagram of the relative position of the tonsil gland and the illuminating surface.

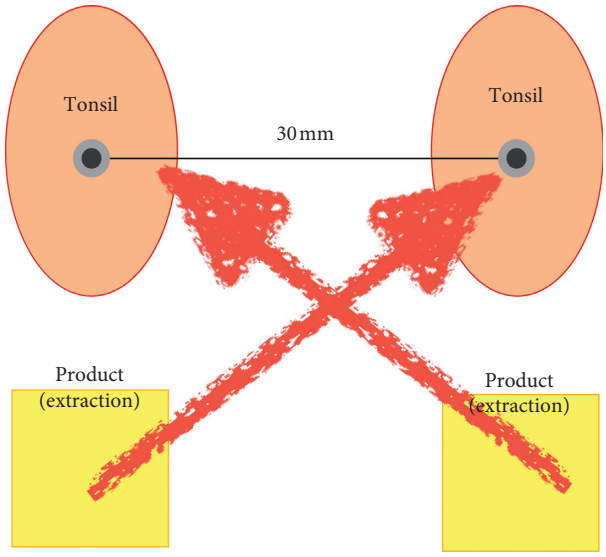

Figure 5: Relative position definition of oral optical simulation.

4200 lux to 9000 lux and is used to illuminate the entire mouth. This study is only for the tonsils, but this lighting interval is still available as a reference interval. The second headless lamp illumination [13] is as high as 50000 lux, but the working distance is 250 mm. The distance between the study products is 25 mm from the tonsil, the working distance is 10 times that. The calculation is based on the ratio and shows the illumination target is 5000 lux. The lighting range of 5000 is also met in the first item ebite2. Therefore, after the literature patent basis and after discussion with the clinician, the target illuminance was confirmed to be 5000 lux.

3. Simulation Results

In order to illuminate the obliquely diagonal area of the tonsil, it was necessary to refract the light. Therefore, a lens was designed to concentrate on the light source. After the experiment, we found that the geometric refraction surface was divided into three segments. It would achieve the optimization of the current illumination, so we divided the refraction angle into three refraction surfaces, which made the best use of the light in each segment and achieved the light intensity required for tonsil surgery. The structure is shown (see Figure 6).

3.1. Simulation Results of Oral Lighting Reflective Surface Design. The design of the single-angle reflecting surface reveals that the light cannot be completely projected onto the receiving surface (the area of the tonsil). This study is going to talk about the change to three angular reflecting surface design structures (see Figure 7). From the simulation results

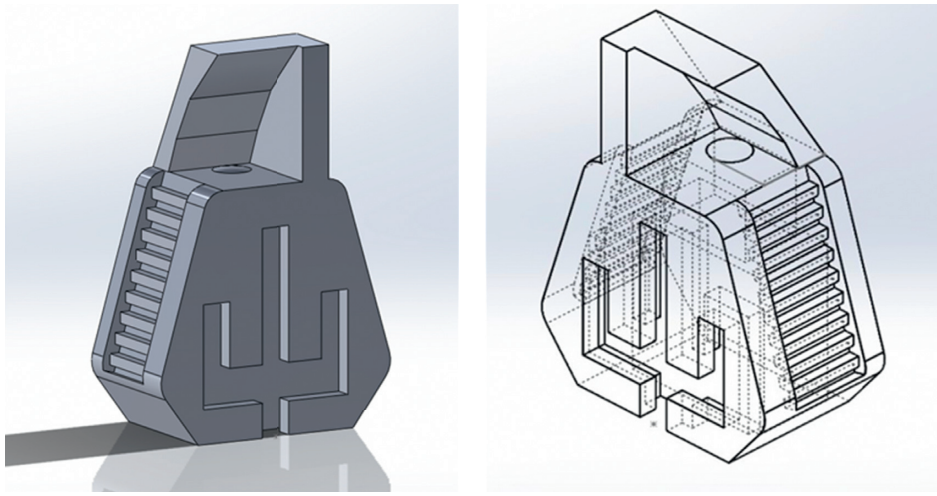

(a) (b)

Figure 6: Schematic diagram of oral lighting structure.

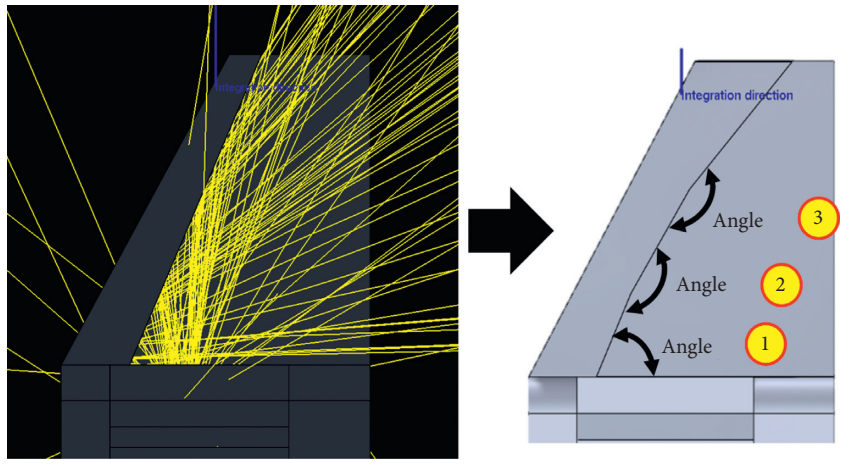

Figure 7: Schematic diagram of the geometric bevel angle of the oral lighting structure.

of the reflection surface angle 1, it can be found that the maximum simulated illumination value can reach 1419 lux when the angle is 67 degrees (see Figure 8). The simulation results of the angle of reflection 2 show that the maximum simulated illumination value can reach 4066 lux at an angle of 173 degrees (see Figure 9). The simulation results of the angle of the reflection surface 3 show that the highest simulated illumination value can reach 5029.19 lux when the angle is 171 degrees (see Table 1 and Figures 10 and 11).

3.2. Simulation Results of Oral Lighting Lens Design. The structural design of the lens is mainly to completely collect the LED light, improve the light utilization rate, and obtain various results with the different curvature radius of the lens. Figure 12 shows the light intensity result obtained by the actual simulation, which clearly shows that the optimum radius of curvature is 41 degrees, and the illuminance can reach 5102 lux. It can be seen from Figure 13 that the light has been clearly focused on the opposite receiver, and the target value of the oral lighting has been reached.

4. Manufacturing Process and Measurement

The mold is designed according to the optimal simulation design structure parameter value, the complex prototype mold is quickly printed by 3D printing technology, and then the oral lighting devices is transformed by reverse engineering and mold casting technology. Finally, the mold dimensions and optical characteristics are measured. The production process is shown in Figure 14.

4.1. Mold Design and 3D Printing. Subverting the traditional mold precision mechanical production method to adopt 3D printing technology to make the mold core, the model of this research has high complex characteristics, which is one of

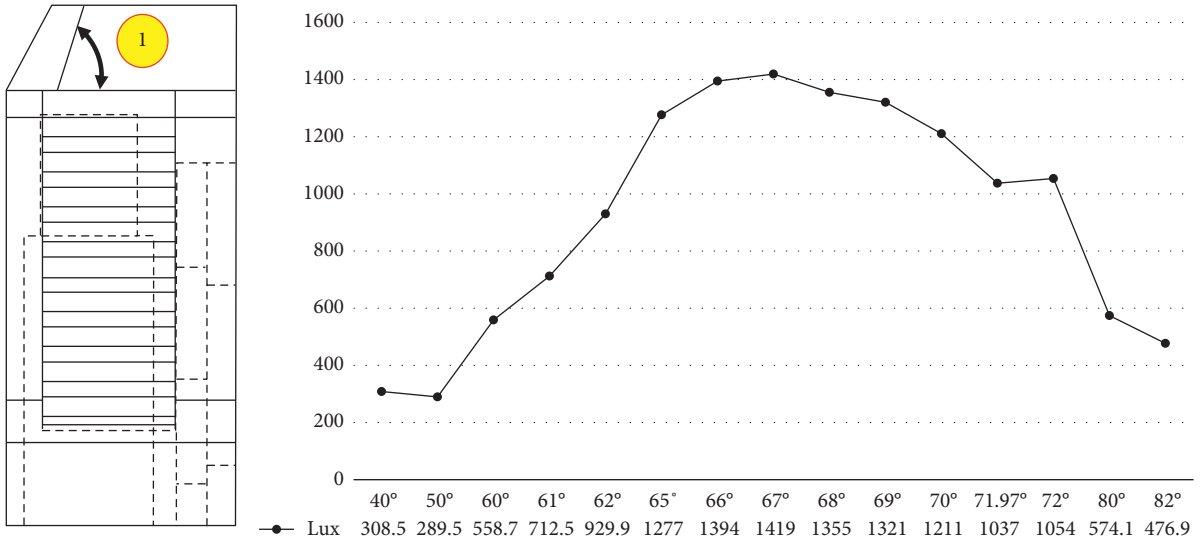

Figure 8: Schematic diagram of geometric bevel angle 1 and optical simulation results.

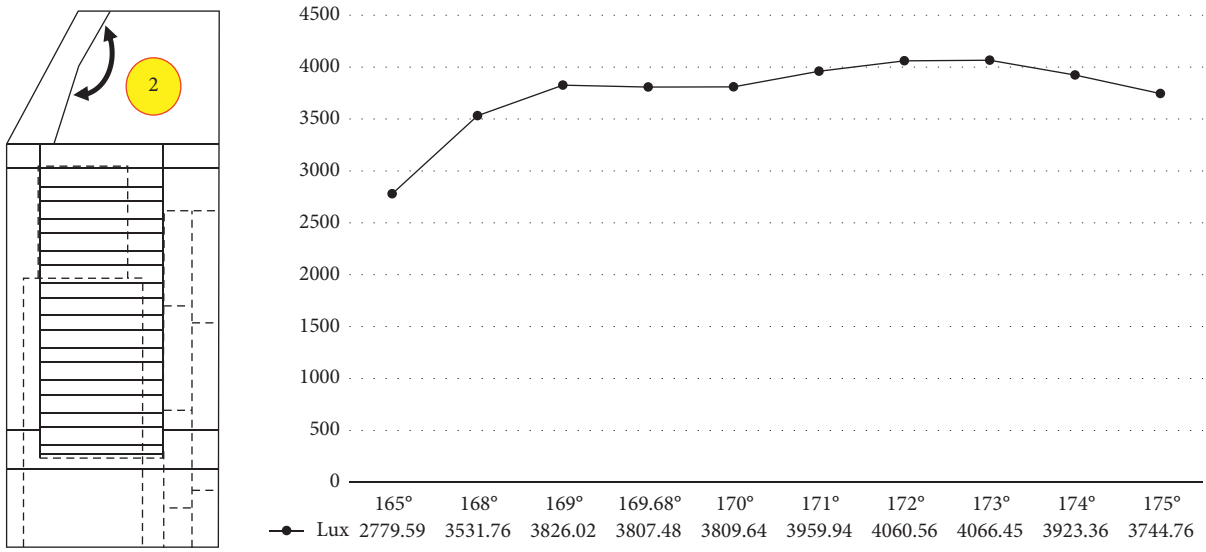

Figure 9: Schematic diagram of geometric bevel angle 2 and optical simulation results.

Table 1: Optical analog measurement value of geometric bevel angle 3.

Area	Shape	Parameters	Magnitude	Measure	Value
Area_1	Rectangle	(0; 0) (5; 5)	Illuminance	Average	5029.19 lx

the advantages of 3D printing. The parting line is the maximum appearance of the product in the drafting direction. The parting surface is the contact surface of the male and female mold blocks which can be produced by the mold. The relationship between the parting line and the parting surface can be stated as follows: the contour line which is the intersection of the parting surface and the product surface is a parting line. In the design of the mold, the parting line is judged to be completed, and the next step is to form the parting surface by extending the parting line in the most suitable direction (see Figure 15). The parting surface is judged by the drawing direction of the molding product. Assuming that a plane perpendicular to the direction is the judgment basic plane, the maximum range of the appearance surface of the molding product projected onto the plane is its parting line. According to the parting line, the appropriate extension is the parting surface. The parting surface can be simple on only one plane, that is, the parting line of the molded product is on the same plane; it can also be complex, irregular, or stepped.

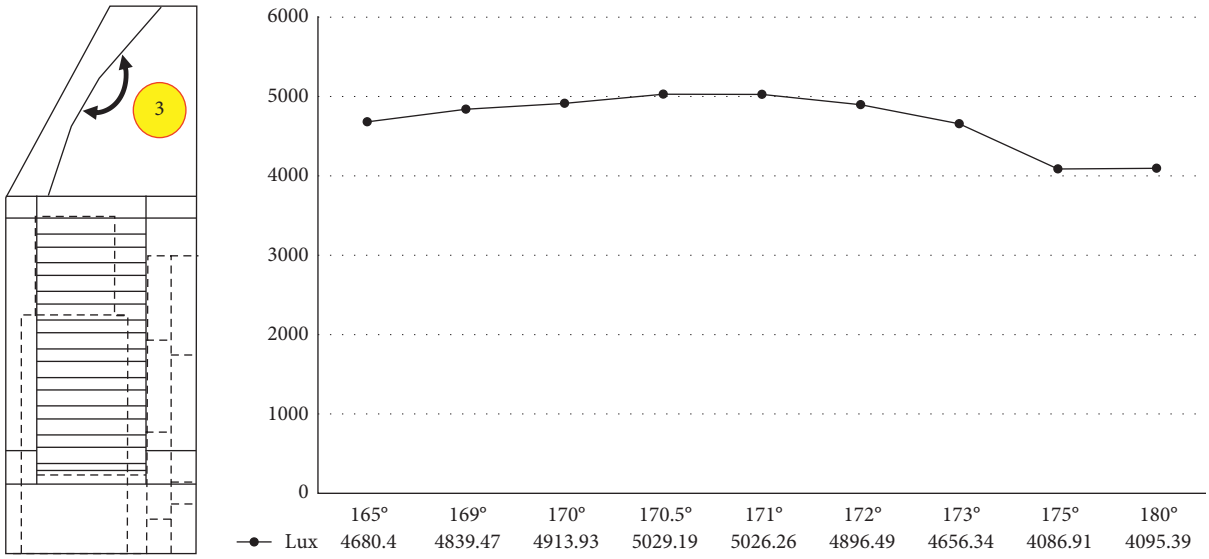

Figure 10: Schematic diagram of geometric bevel angle 3 and optical simulation results.

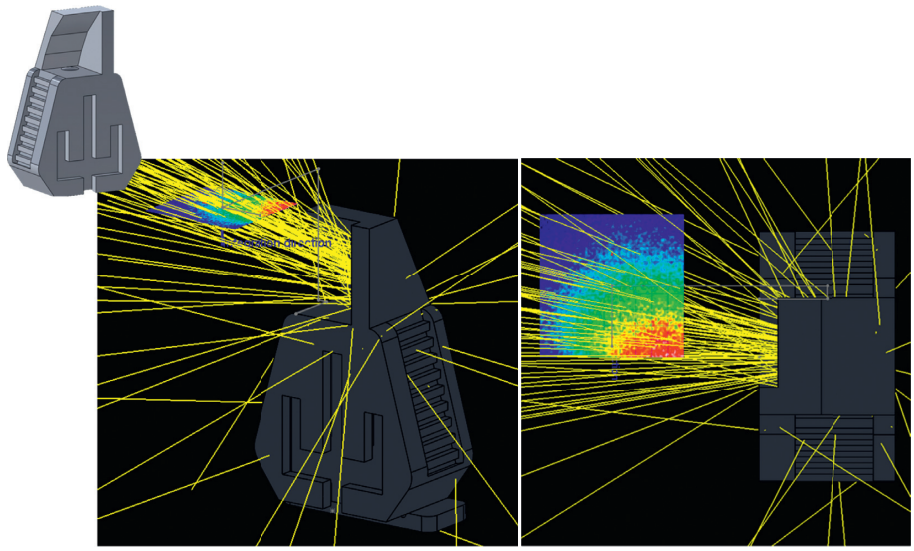

Figure 11: Optical analog light trace of geometric bevel angle 3.

In order to make the structure of the mold simple and reduce the manufacturing cost, the mold design surface is generally designed as a single plane, that is, a plane perpendicular to the drawing direction. In the mold design, the nonflat single-plane parting surface is chosen, that is, the design of the parting surface composed of several surfaces should be avoided. This is because there would be additional processing and appearance and dimensional tolerance problems for subsequent contact surfaces between the blocks. However, in the current industry, due to demand and saving subsequent processing costs, complex parting surface products account for a relatively large number. The mold of this study was split into three devices according to the parting line (plane) design (see Figure 16).

The 3D printing technology is based on the assistance of Computer Aided Design (CAD) software. The 3D CAD model is cut into thin layers, and the process of decomposing 3D data into 2D data is performed. According to the layered 2D data, the manufacturing method is used to produce the same thickness as the data layer. The process of each layer of sheets overlapping forms a 3D solid object. 3D printing mold has three-device finished products (see Figure 17).

4.2. Mold Casting Process. PDMS is the most widely used polymer biomedical material known at present. The cost of the material is much lower than that of strontium and quartz glass. The process is simple and rapid, the light transmittance and biocompatibility are good, and it is easy to combine with various materials at room temperature. It is a porous absorbent for oxygen and carbon dioxide and has been widely

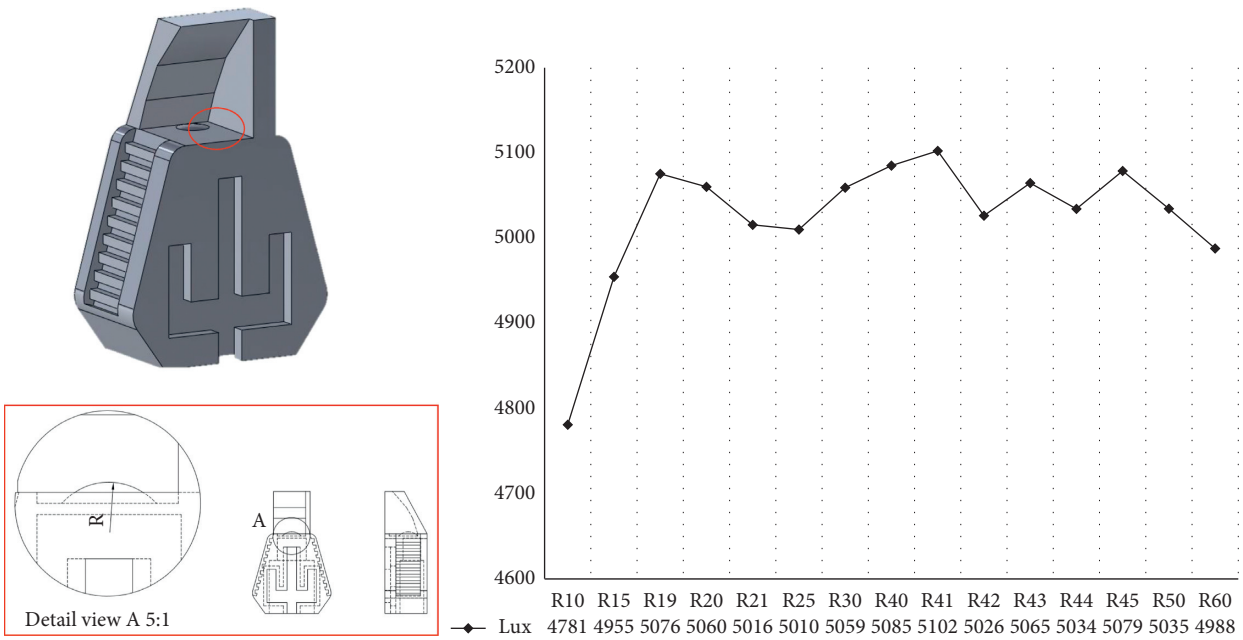

Figure 12: Simulation results of lens curvature radius design.

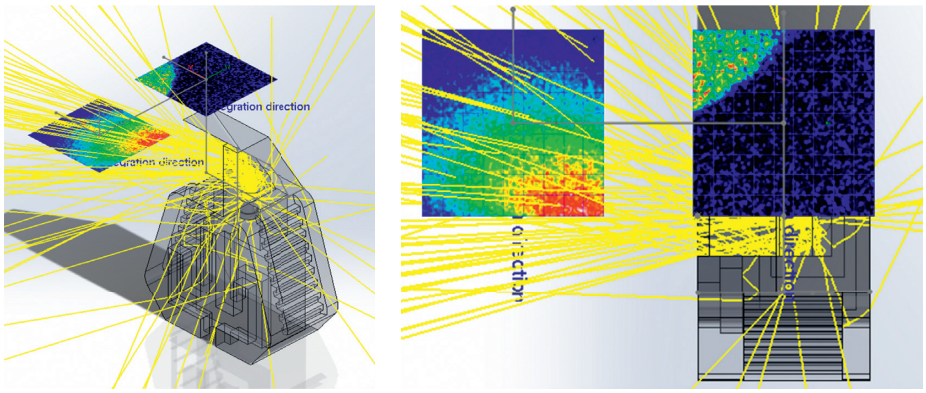

Figure 13: Simulation results of oral lighting optical microstructure device design.

used in various biomedical research. The polydimethylsiloxane (PDMS) used in this study was produced by Sil-More Industrial Ltd. The main agent SYLGUARD-184A and the hardener SYLGUARD-184B were uniformly mixed at a mass ratio of 10 : 1. Mixed by vacuuming, the bubbles in the liquid are deformed and then left to stand or heat to form.

The mold is made by using a 3D printing machine. When the two molds are combined, the positioning pins, and the clamps, bolts, and nuts are used to fix the four corners of the mold. The mold casting is used to complete the PDMS mold. During the mold casting, in order to smoothly let the air discharge so that it does not remain in the flow channel and affect the forming, a utility knife can be used at the bottom of the flow channel to scrape a little knife mark, and the air is discharged along the direction of the tool mark. The PDMS casting finished product is shown (see Figure 18).

4.3. Finished Product Measurement

4.3.1. Finished Product Shape Profile Inspection. Comparing the difference between the size of the mold and the 3D printing mold after PDMS mold casting, the completed PDMS finished product is measured under Computer Aided Verification (CAV) two-dimensional image measuring results (see Figure 19). The data shows the 3D printing finished product of the oral device structure, and the average error of the profile of the PDMS-finished product is about 1.4% and 16.9%, respectively. Contrasting the PDMS mold after casting with the 3D printing mold shows that there is shrinkage. The reason causing the results might be the shrinkage due to temperature of the wax mold. The further shrinkage occurs when contacting with the heated mold.

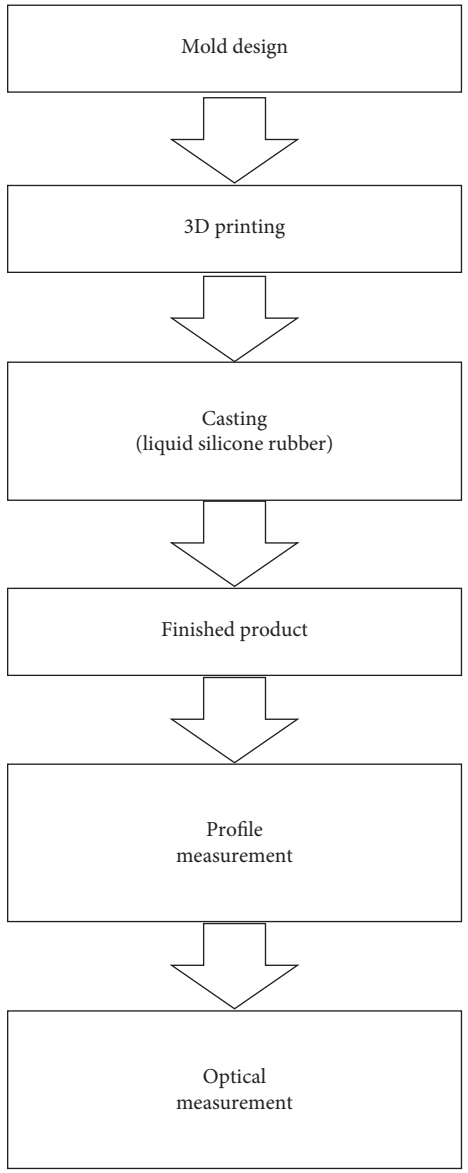

Figure 14: Schematic diagram of the mold structure production process.

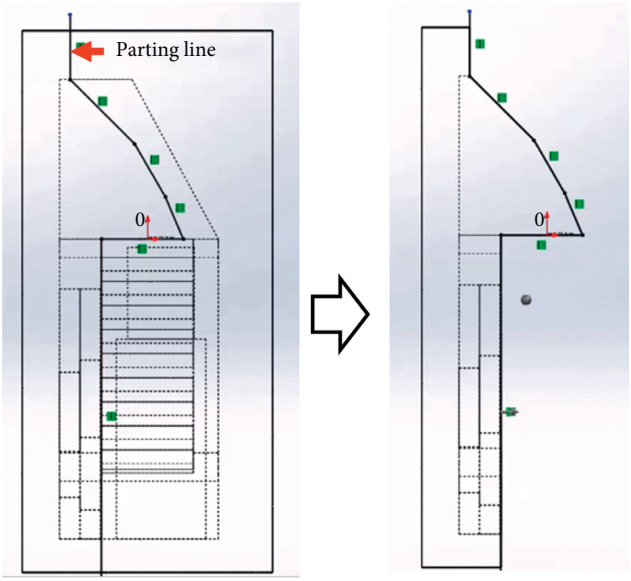

Figure 15: Schematic diagram of the parting line of the mold design.

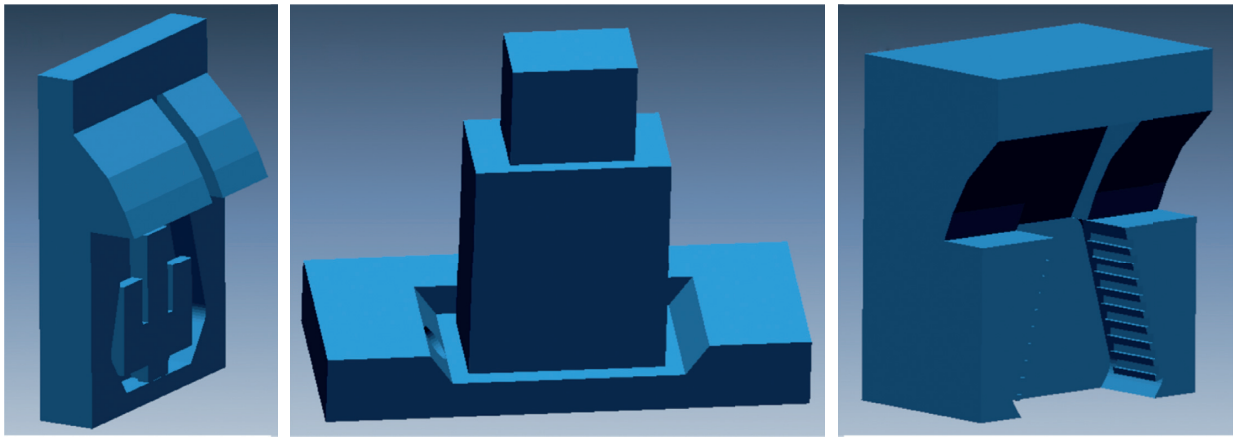

(a) (b) (c)

Figure 16: Computer aided mold design.

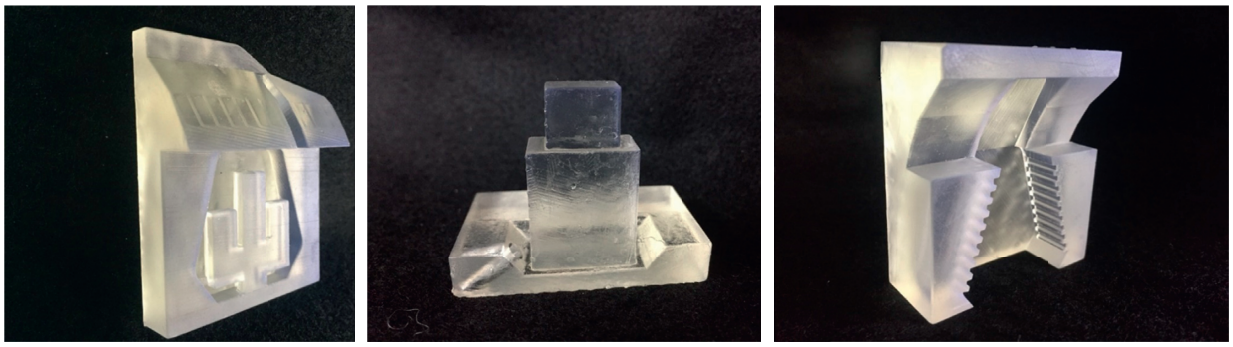

(a) (b) (c)

Figure 17: 3D printing finished product.

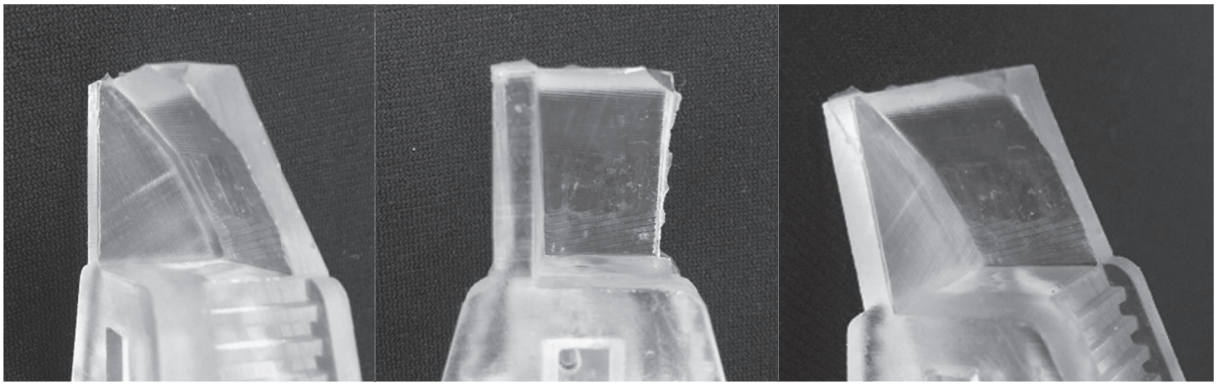

Figure 18: PDMS casting finished product.

4.3.2. Oral Lighting Optical Microstructure Device Light Distribution Detection. The luminance optical properties were measured by using a conoscope machine. Figure 20 shows the light distribution was attached to a micro-optical element. Light was scattered from the center to the left and right sides, thus proving that the optical element can generate one side perspectives. The distance of the measured light deviation is 0.5~3 mm due to the contour error of the finished PDMS (see Figure 20), but the light is still concentrated in the range of the tonsils. Therefore, this result can be defined as an acceptable range within 16.9% of the intra lighting error.

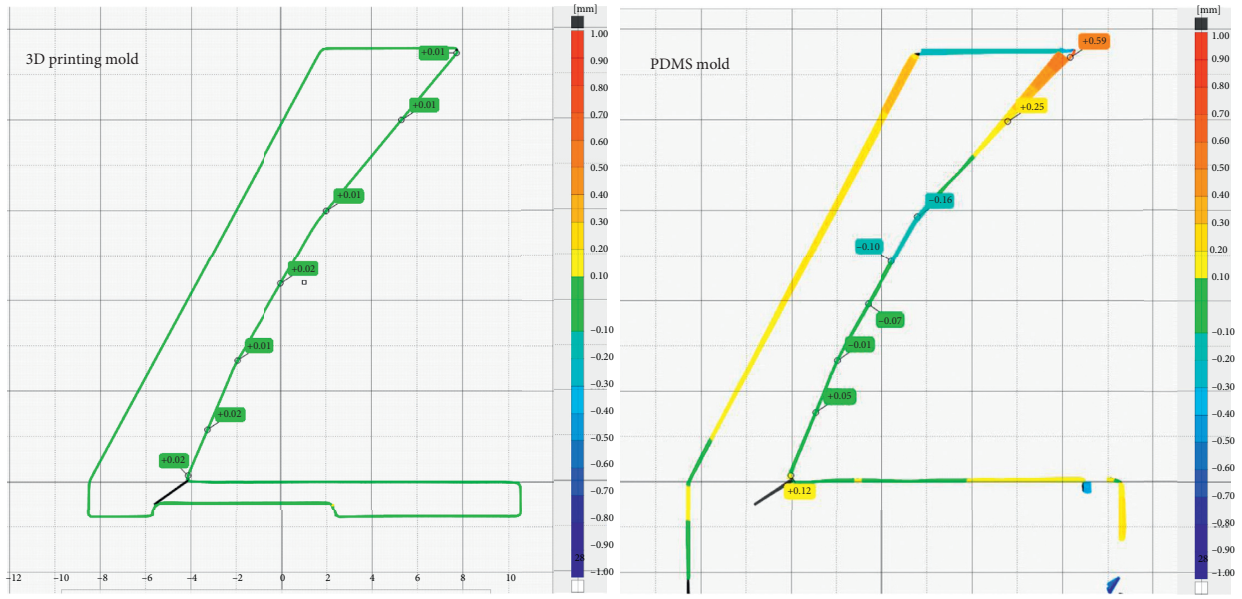

Figure 19: Finished product shape profile measurement.

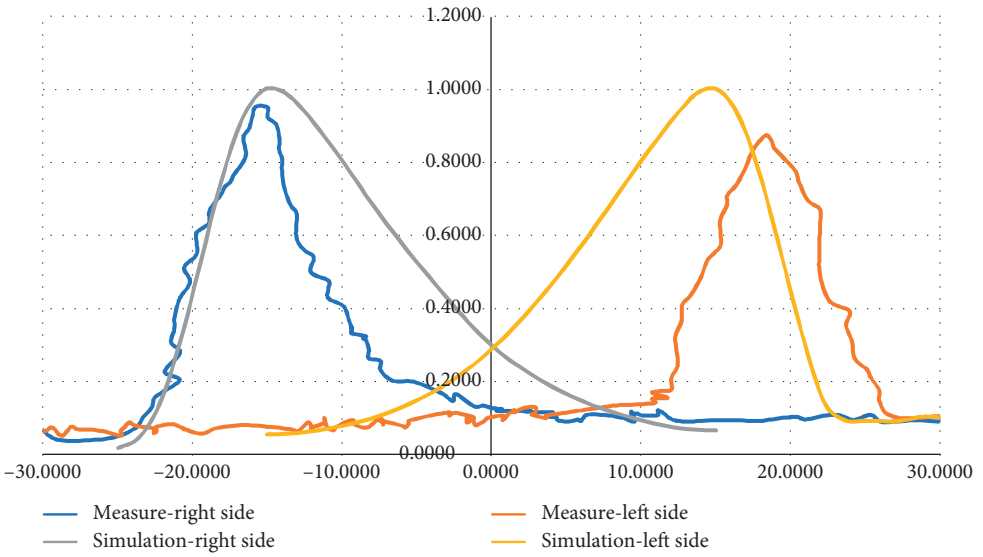

Figure 20: Distribution diagram of finished optical measurement.

5. Discussion and Conclusions

The development of oral lighting optical microstructure devices has undergone many modifications. From the beginning of the main body, a trapezoidal groove is dug down, and the optimal angle of the slope is obtained by optimization, but the actual light is reflected after the simulation. As expected, the measurement only received 150 lux illumination, and the subsequent improvement began to develop a bevel structure to the upper end of the main body as a plane where the light can be directly refracted. The illuminance is gradually improved after the main body is extended upward. A change from 538 lux to the highest illuminance of 2080 lux can be achieved with the change of the angle of the bevel, but still does not reach the set value of 5000 lux. The optical part encountered difficulties, but after many simulations and modifications, it is found that if a lens is added to collect light on the light source and the angle of refraction angle is divided into three geometric refractive surfaces, the optimal light intensity can be achieved, and the radius of curvature of the lens also affects the intensity of the light. It was found that the illuminance drop was from a minimum of 4955 lux to a maximum of 5100 lux, and this illuminance did achieve the set target value.

The purpose of this study was to develop an oral lighting device that has high illumination in the interior of the oral cavity. Firstly, the design of the lighting element is designed by making the oral lighting devices, discussing its

illumination by optical simulation analysis, and designing the illumination component with high illumination. The oral lighting device is produced for actual photometric measurement. The successful development of a low-cost and easy-to-assemble high-illumination oral lighting devices facilitates mass production in the future. The results of the study met the original design goals: (1) to open the mouth to facilitate the doctor's surgery; (2) to fix the tongue in order to avoid it interfering with the operation, because if the tongue is lifted, it will block the sight; (3) add lighting function to help the doctor during the operation to avoid the lack of light; and (4) reduce the number of tools required before surgery, such as oral spreaders, lighting equipment, tongue depressors, and other medical equipment. This study would solve the problem of clinicians having to wear a fiber-optic projection lamp due to poor head swing angle or visual field blindness, reduce the burden of physicians in nonprofessional fields, reduce the operation time of patients to maintain the health quality of doctors, and further advance the medical equipment standards to improve surgical safety.

Data Availability

The processed data required to reproduce these findings cannot be shared at this time as the data also form part of an ongoing study.

Conflicts of Interest

The authors declare that there are no conflicts of interest regarding the publication of this paper.

Acknowledgments

This study was supported by Ministry of Science and Technology, MOST 108-2221-E-029-019. The authors would like to thank Prof. Pin Han, The Graduate Institute of Precision Engineering, Chung Hsing University and Ms. Liu Meng Chieh, Ms. Liang Huai Yu, Ms. Liu Lo Yu, Mr. Kuo Chin Yu, Mr. Peng Yen Chieh, Mr. Ku Feng Jui, and Mr. Hsieh Yi Ching, The Department of Industrial Engineering and Enterprise Information, Tunghai University and Taichung Veterans General Hospital, for their support in this research.

References

[1] C. Canavesi, F. Fournier, W. J. Cassarly, T. H. Foster, and J. P. Rolland, "Illumination devices for photodynamic therapy of the oral cavity," *Biomedical Optics Express*, vol. 1, no. 5, pp. 1480–1490, 2010.

[2] B. Crohn, "Intraoral illumination device," US Patent US7153131B2, 2006.

[3] Z. Jason Geng, "Sanitary sleeve or tip for intra-oral three-dimensional camera," US Patent US7099732B2, 2006.

[4] S. S. Duplantis, "Apparatus and method for enhancing the images of intra-oral photography," US Patent US4921344A, 1990.

[5] D. Meyers and R. Burman, "Intraoral illumination device," US Patent US20040063060A1, 2004.

[6] Isolite system, http://www.isolitesystems.com/.

[7] eBite system, http://www.ebiteshop.com/.

[8] Y. Liu, P. Zhang, Y. Deng et al., "Polymeric microlens array fabricated with PDMS mold-based hot embossing," *Journal of Micromechanics and Microengineering*, vol. 24, no. 9, Article ID 095028, 2014.

[9] H. Yang, C. Y. Yang, and M. S. Yeh, "Fabrication of miniaturized variable-focus lens using liquid filling technique," in *Proceedings of the DTIP 2007*, Stresa, Italy, April 2007.

[10] H. Ren, D. Fox, P. A. Anderson, B. Wu, and S.-T. Wu, "Tunable-focus liquid lens controlled using a servo motor," *Optics Express*, vol. 14, no. 18, pp. 8031–8036, 2006.

[11] K.-H. Jeong, G. L. Liu, N. Chronis, and L. P. Lee, "Turnable microdoublet lens array," *Optics Express*, vol. 12, no. 11, p. 2494, 2004.

[12] N. Chronis, G. Liu, K.-H. Jeong, and L. Lee, "Tunable liquid-filled microlens array integrated with microfluidic network," *Optics Express*, vol. 11, no. 19, pp. 2370–2378, 2003.

[13] Heine ML4 LED Headlight, https://www.heine.com/en/products/loupes-and-headlights/headlights/detail/32125-heine-ml4-led-headlight.

Hindawi
International Journal of Optics
Volume 2019, Article ID 4270612, 10 pages
https://doi.org/10.1155/2019/4270612

Research Article

The Critical Adiabatic Linear Tapered Waveguide Combined with a Multimode Waveguide Coupler on an SOI Chip

C. L. Chiu and Yen-Hsun Liao

Department of Electronic Engineering, National Kaohsiung University of Science and Technology, No. 415 Jiangong Road, Kaohsiung 807, Taiwan

Correspondence should be addressed to C. L. Chiu; clchiu@nkust.edu.tw

Received 10 August 2019; Revised 12 October 2019; Accepted 17 October 2019; Published 11 November 2019

Guest Editor: Cheng-Mu Tsai

A multimode waveguide interference (MMI) coupler is combined with a critical linear tapered waveguide on a silicon-on-insulator (SOI) chip. When the TE_0 mode is a critical adiabatic mode conversion from a single-mode waveguide to an extreme linear tapered waveguide combined with an MMI, this linear tapered waveguide is achieved to the maximum divergence angle (i.e., the shortest length). The maximum divergence angle is expressed by $\theta \leq 2\tan^{-1}[(0.35W_{\mathrm{mmi}} - W_{\mathrm{s}})/(0.172L_{\mathrm{mmi}})]$ under a 1×1 MMI combined with this critical linear tapered waveguide. The expression formula is demonstrated by three different widths of a 1×1 MMI of $4\,\mu$m/$8\,\mu$m/$12\,\mu$m combined with the critical linear tapered waveguide. So, the maximum divergence angle is obtained at $\theta = 16^{\circ}/14^{\circ}/8^{\circ}$, with respect to this linear tapered waveguide loss of 0.022 dB/0.172 dB/0.158 dB, and this linear tapper length is reduced by 93.7%/92.9%/87.5% than the divergence angle $\theta = 1^{\circ}$. The output power of a 1×1 MMI combined with a critical linear tapered waveguide is enhanced at least 1.5 times under 0.95 above condition.

1. Introduction

In the last few years, there have been numerous advances in silicon photonics. Photonic devices on a silicon-on-insulator (SOI) chip with high-index contrast have high integration density. The main advantage of the optoelectronic component on an SOI structure is its good compatibilities [1]. Couplers and power dividers in photonic integrated circuits (PICs) are often implemented with multimode interference couplers (MMIs) for easy fabrication and broad bandwidth. The SOI platform is an area of interest in integrated optics at present and enables a size reduction of PICs. Therefore, their CMOS compatibility can provide optoelectronic integration on a chip in future applications [2]. MMIs are based on the expansion of a fundamental mode of the access waveguide into multiple modes of the wider width of a multimode waveguide, which interfere as they propagate and form images of the excitation. Ridge waveguides are widely used in SOI, as they offer a single-mode behaviour at micrometre scale [3]. MMIs depend on multimode waveguides, utilizing bends for higher order mode filtering. They generally propagate well, and the weak lateral confinement of narrow ridge waveguides makes it difficult to achieve high-performance devices [4].

In 2010, Thomson et al. proposed a method to achieve a reduction of optical loss through the use of linear tapers with input and output ports. The taper loss is reduced to below 1 dB without affecting static extinction [5]. In 2012, Sheng et al. proposed the compact and low-loss MMI coupler fabricated with CMOS technology. This tapered waveguide with a divergence angle θ of 1° combined with an MMI is fabricated on SOI with 0.13 μm CMOS technology to obtain an excess loss of only 0.06 dB [6]. Researchers have adopted the widest and longest linear tapered waveguide to be combined with an MMI coupler on an SOI chip in recent devices. This critical problem will increase manufacturing costs, so it is necessary to design an adiabatic tapered waveguide.

The losses inherent to a mode propagating waveguide must be reduced on the cross-sectional boundary between the single-mode waveguide and multimode waveguide. Because a tapered waveguide can change the spot size and

the shape of the optical mode to achieve high coupling efficiency in the cross section boundary [7], a tapered waveguide is necessary to achieve an adiabatic state [7–10]. That is, as the TE_0 mode from a single-mode waveguide is transmitted to the tapered waveguide, the other higher order TE modes are reduced to excited modes [11–17].

In this article, we propose an expression formula to design a terminal linear tapered waveguide to enhance the coupling efficiency output power of an MMI coupler to two times above. The low-loss and maximum divergence angle linear tapered waveguide combined with a 1×1 MMI on an SOI chip is achieved to an output power of above 0.95. The TE_0 mode component ratio is necessary to be above 97.85% in order to achieve a critical adiabatic mode conversion.

2. Device Structure

The cross section of an SOI structure is shown in Figure 1. The thickness of the upper cladding SiO_2 layer is 2 μm, and the Si layer is deposited at a height h_{co} of 220 nm on a 2 -μm-thick buried oxide layer based on a Si substrate. The refractive indices of Si and SiO_2 are $n_{Si} = 3.475$ and $n_{SiO2} = 1.444$, respectively. The ridge waveguide has a depth of 2.22 μm, and the effective core refractive index n_r of 2.509 and cladding refractive index n_c of 2.372 at an operating wavelength λ_0 of 1550 nm in a slab waveguide [18].

MMI couplers have higher tolerance to dimensional changes in the fabrication process, an easier fabrication process than other couplers, lower inherent loss, large optical bandwidth, and low polarization dependence [19]. Multimode waveguides excite numerous modes depending on their width and depth. The width of a fixed step index multimode waveguide W_{mmi} is generally referred to as $N\times M$ MMI coupler, where N and M indicate input and output ports. For high-index contrast waveguides, the penetration depth is very small so that $W_e \approx W_{mmi}$. However, the effective width W_e can correspond to the fundamental mode [18]:

$$W_e = W_{mmi} + \left(\frac{\lambda_0}{\pi}\right)\left(\frac{n_c}{n_r}\right)^{2\sigma}\left(n_r^2 - n_c^2\right)^{-1/2}, \quad (1)$$

where λ_0 is an operating wavelength and n_r and n_c are the effective core and cladding refractive indices, respectively. The term $\sigma = 0$ represents transverse electric (TE) mode and $\sigma = 1$ is for transverse magnetic (TM) mode. L_π is defined as the beat length of the two lowest order modes [19], as follows:

$$L_\pi = \frac{\pi}{\beta_0 - \beta_1} \cong \frac{4n_r W_e^2}{3\lambda_0}, \quad (2)$$

where β_0 and β_1 are individual zero-order and first-order propagation constant. The term n_r is the effective core refractive index of the slab waveguide from which a 1×1 MMI coupler is made. W_e is the effective width of the MMI waveguide, and L_{mmi} is the exact imaging length [20]:

$$L_{mmi} = \frac{3}{4}L_\pi. \quad (3)$$

The geometric shape of a basic 1×1 MMI coupler is shown in Figure 2(a). A single-mode ridge waveguide with width W_s of 0.4 μm, length L_s of 100 μm, and a depth of 2.22 μm is calculated by the effective core refractive index n_r of 2.509 and the effective cladding refractive index n_c of 2.372 [17]. An MMI width adapted to 10/20/30 times the single waveguide of 0.4 um as an inspecting standard case. The widths of a 1×1 MMI W_{mmi} are choice of 4 μm/8 μm/12 μm respect to the beat lengths L_π of 45.7 μm/159.8 μm/342.9 μm from equation (2) at an operating wavelength of $\lambda_0 = 1550$ nm. Therefore, the exact image length of a 1×1 MMI L_{mmi} achieves 34.3 μm/119.8 μm/257.1 μm, respectively, by equation (3). A linear tapered waveguide combined with a 1×1 MMI is shown in Figure 2(b). The input/output port of this 1×1 MMI is a single-mode waveguide linked with a linear tapered waveguide. W_t is the width and L_t the length of a linear tapered waveguide. The divergence angle θ of a linear tapered waveguide is a taper angle. A half angle of the divergence angle is defined by the following equation:

$$\tan\left(\frac{\theta}{2}\right) = \frac{W_t - W_s}{2L_t}. \quad (4)$$

The simulation analysis utilizes the film mode matching method (FMM) solver in FIMMWAVE software [21,22]. The output power of a basic 1×1 MMI with the exact length L_{mmi} is shown in Figure 3. Figure 3(a) is the length L_{mmi} of a 1×1 MMI scanning the range from 26.7 μm to 30.7 μm with a step of 0.2 μm at MMI width $W_{mmi} = 4$ μm. The maximum output power is 0.62 at $L_{mmi} = 28.7$ μm. Figure 3(b) is the length L_{mmi} of a 1×1 MMI scanning the range from 111.0 μm to 115.0 μm with a step of 0.2 μm at MMI width $W_{mmi} = 8$ μm. Here, the maximum output power is 0.51 at $L_{mmi} = 113.0$ μm. Figure 3(c) is the same method at MMI width $W_{mmi} = 12$ μm for L_{mmi} scanning the range from 255.2 μm to 259.2 μm. Maximum output power is 0.41 at $L_{mmi} = 257.2$ μm. Accordingly, L_{mmi} at MMI width $W_{mmi} = 4$ μm/8 μm/12 μm is 28.7 μm/113.0 μm/257.2 μm, respectively. The device loss of a 1×1 MMI is 2.08 dB/2.92 dB/3.87 dB, respectively, which is very significant.

3. Linear Tapered Waveguide Analysis

When the divergence angle of a linear tapered waveguide is set at $\theta = 1^\circ$ with a width W_t of 4.2 μm and a length L_t of 217.7 μm as an experimental standard result from reference 6, this pair of tapered waveguide loss of almost 0.004 (0.018 dB) can be ignored. This linear tapered waveguide with a divergence angle of 1° is combined with the three different widths of 1×1 MMI W_{mmi} of 4 μm/8 μm/12 μm with respect to the exact imaging lengths L_{mmi} of 28.7 μm/113.0 μm/257.2 μm. When the ratio of W_t/W_{mmi} is increased from 0.1 to 1 at a step of 0.05, the range of the output power increases from 0.68 to 1, as shown in Figure 4. The output power of a 1×1 MMI combined with the linear tapered waveguide is necessary to be above 0.95 as the ratio of W_t/W_{mmi} is set to above 0.35.

Figure 5 shows the effective refractive index n_{eff} for eight TE eigenmodes, including TE_0, TE_1, TE_2, TE_3, TE_4, TE_5, TE_6, and TE_7 distributed with the width of a linear tapered

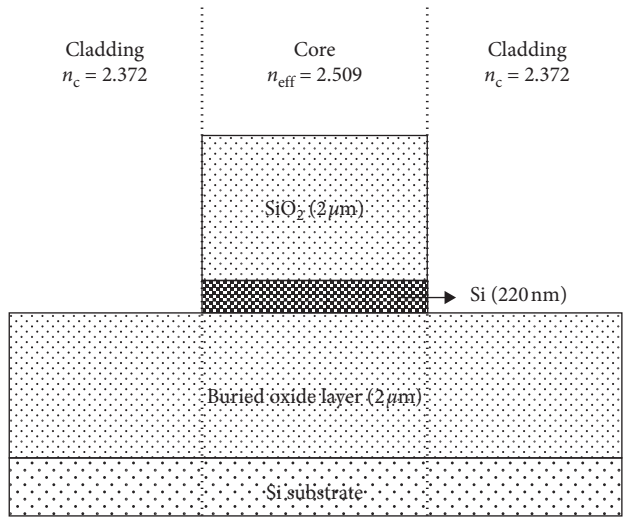

Figure 1: Schematic diagram showing the cross section of a ridge waveguide on an SOI structure.

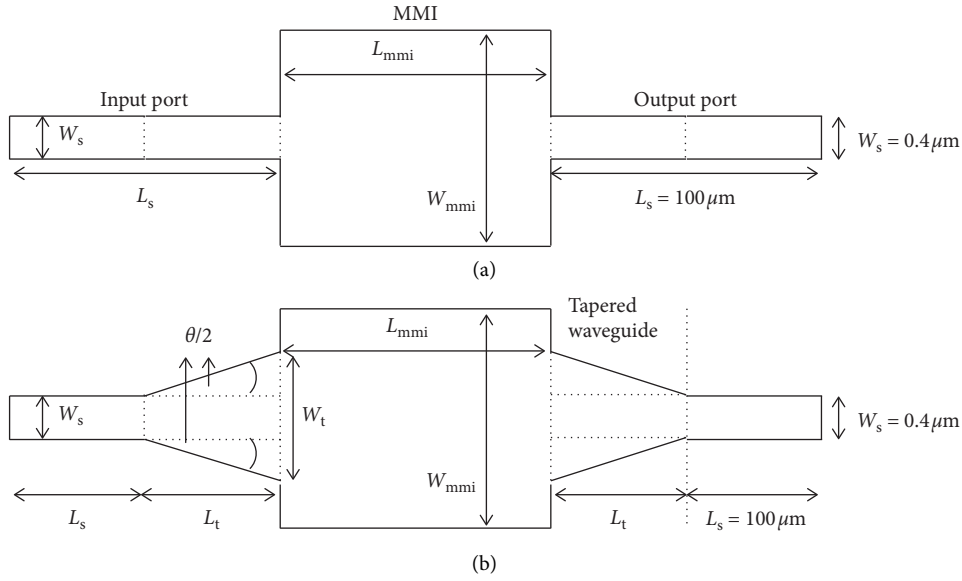

Figure 2: (a) A basic 1×1 MMI combined with the input/output single-mode waveguide for width $W_s = 0.4\,\mu$m and length $L_s = 100\,\mu$m. (b) A linear tapered waveguide is inserted between the single-mode waveguide and MMI coupler. Width W_t, length L_t, and divergence angle θ describe the linear tapered waveguide.

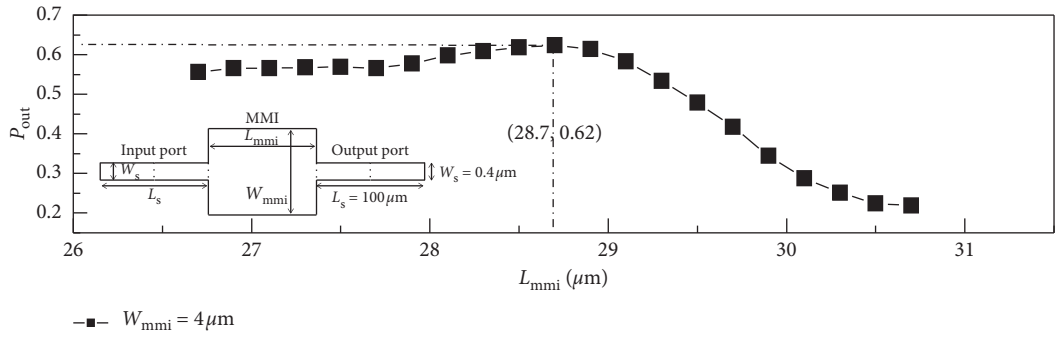

(a)

Figure 3: Continued.

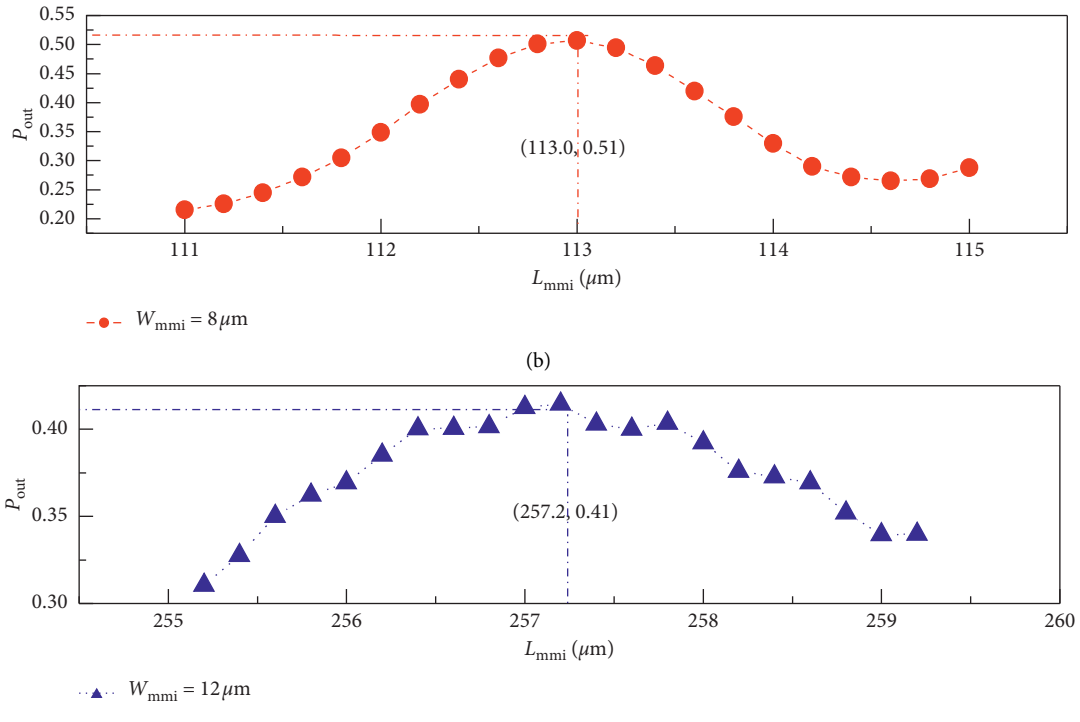

FIGURE 3: (a) The maximum output power is 0.62 at MMI length $L_{mmi} = 28.7\,\mu$m with a 1×1 MMI width $W_{mmi} = 4\,\mu$m. (b) Maximum output power is 0.51 at $L_{mmi} = 113.0\,\mu$m and $W_{mmi} = 8\,\mu$m. (c) Maximum output power is 0.41 at $L_{mmi} = 257.2\,\mu$m and $W_{mmi} = 12\,\mu$m.

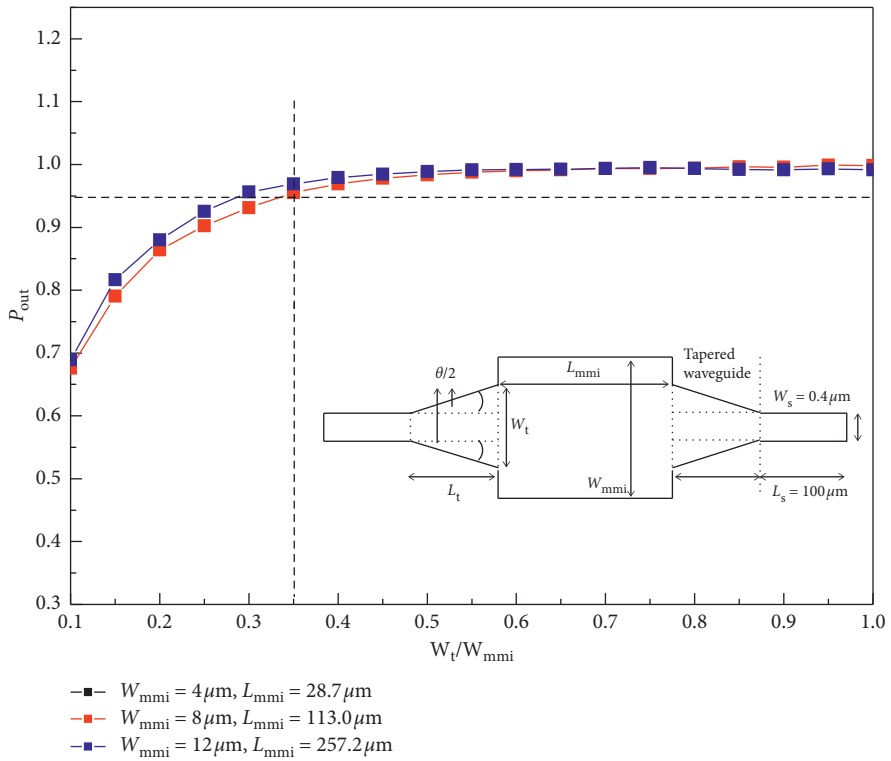

FIGURE 4: This linear tapered waveguide with a divergence angle of 1° is combined with the three different widths of a 1×1 MMI coupler W_{mmi} of $4\,\mu$m/$8\,\mu$m/$12\,\mu$m with respect to the exact imaging lengths L_{mmi} of $28.7\,\mu$m/$113.0\,\mu$m/$257.2\,\mu$m. When W_t/W_{mmi} is set at above 0.35, the output power P_{out} of a 1×1 MMI coupler combined with a linear tapered waveguide achieves above 0.95.

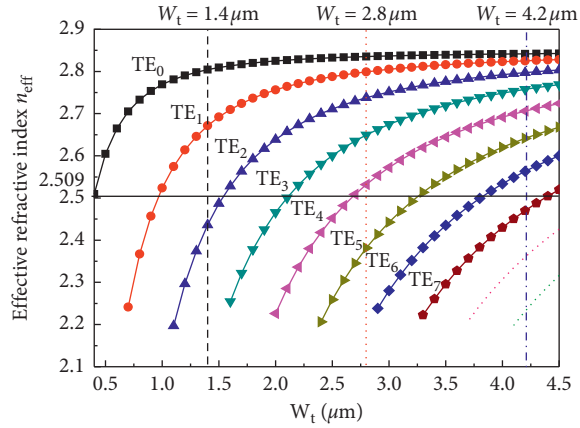

FIGURE 5: The effective refractive index of the distributed state of eight TE modes with the width of a linear tapered waveguide is ranging from 0.4 μm to 4.5 μm. The effective refractive index n_{eff} of the slab waveguide on an SOI chip is 2.509 and the thickness of this linear tapered waveguide h_{co} is 220 nm at an operating wavelength of 1550 nm.

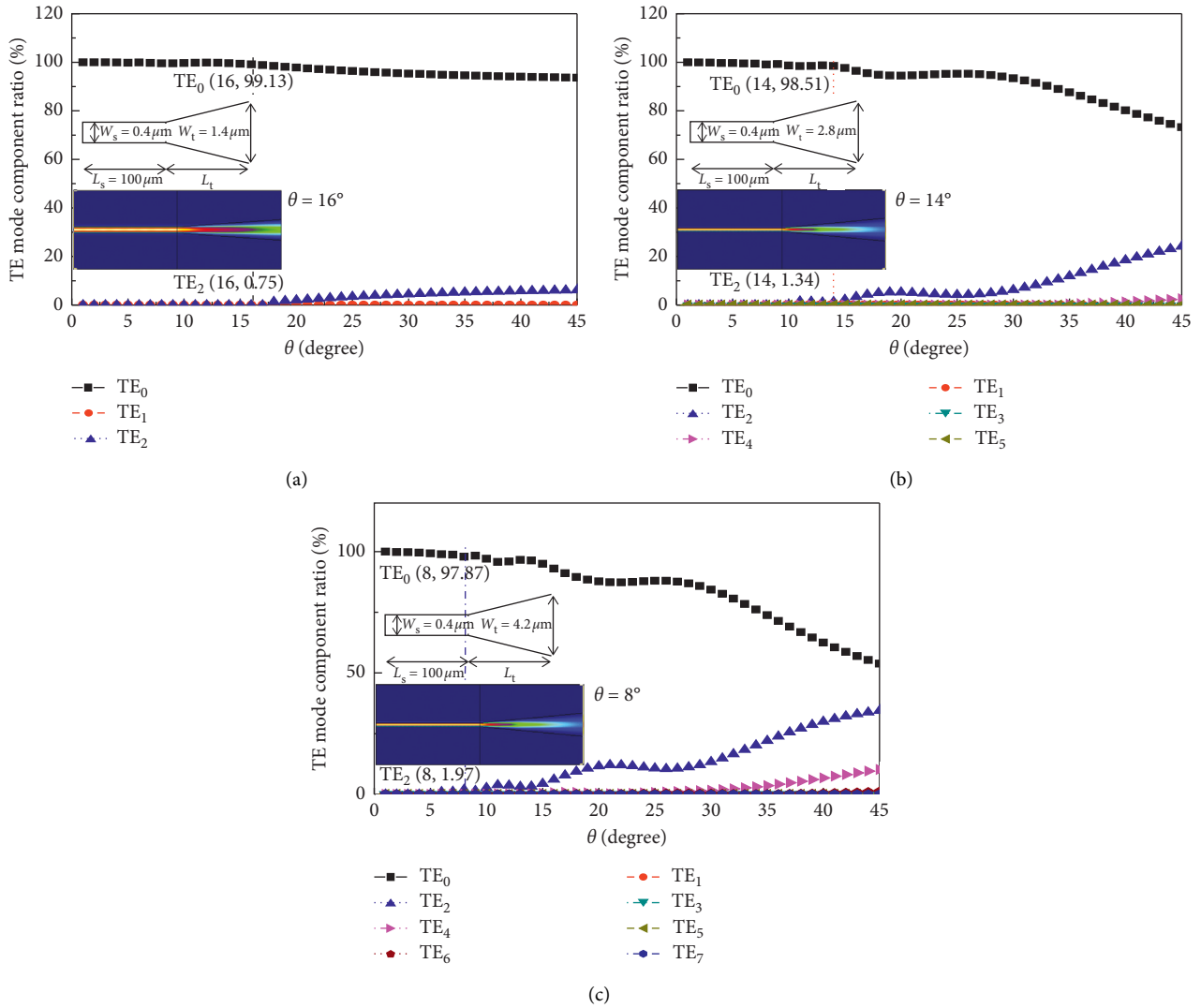

FIGURE 6: The width of a linear tapered waveguide (a) $W_t = 1.4\,\mu m$, $W_{mmi} = 4\,\mu m$; (b) $W_t = 2.8\,\mu m$, $W_{mmi} = 8\,\mu m$; (c) $W_t = 4.2\,\mu m$, $W_{mmi} = 12\,\mu m$; with divergence angle θ of a linear tapered waveguide ranging from 1° to 45°. The maximum divergence angle for linear tapered waveguide is achieved at $\theta = 16°/14°/8°$ for $W_t = 1.4\,\mu m/2.8\,\mu m/4.2\,\mu m$, respectively.

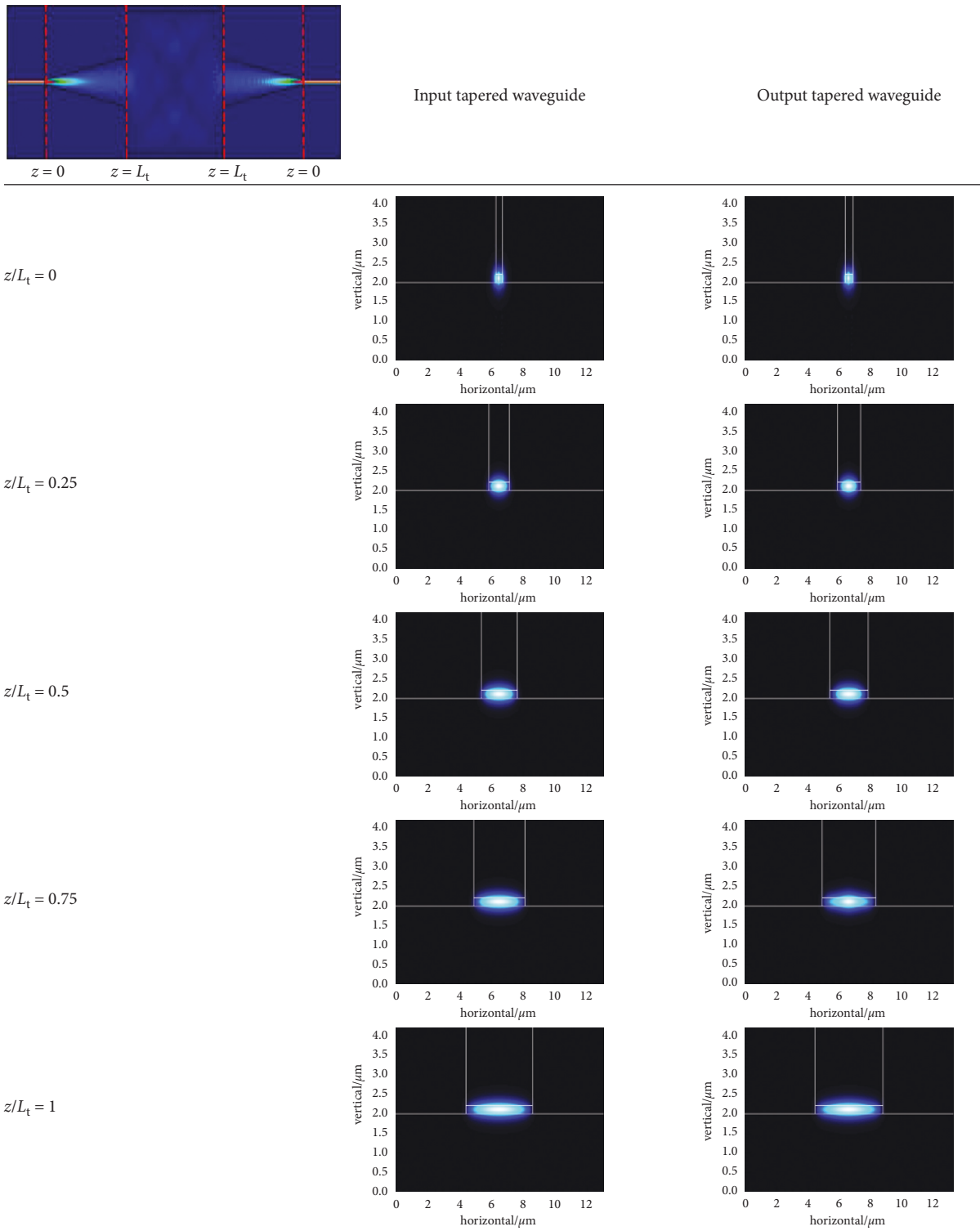

FIGURE 7: A 1 × 1 MMI in width of 12 μm and in length of 257.2 μm is combined with the linear tapered waveguide in width W_t of 4.2 μm and in length L_t of 217.7 μm. When the location of input/output linear tapered waveguide is z/L_t of 0/0.25/0.5/0.75/1, the fundamental mode TE_0 shape of input/output port is simulated to change the mode shape size from small to larger mode shape under TE_0 adiabatic mode conversion.

waveguide from 0.4 μm to 4.5 μm. As the effective refractive index n_{eff} of a slab waveguide on an SOI chip is 2.509, the eight TE eigenmodes, including TE_0 to TE_7, correspond to the widths of the linear tapered waveguide W_t. Three different widths of 1 × 1 MMI W_{mmi} of 4 μm/8 μm/12 μm obtain a minimum width for a linear tapered waveguide W_t of 1.4 μm/

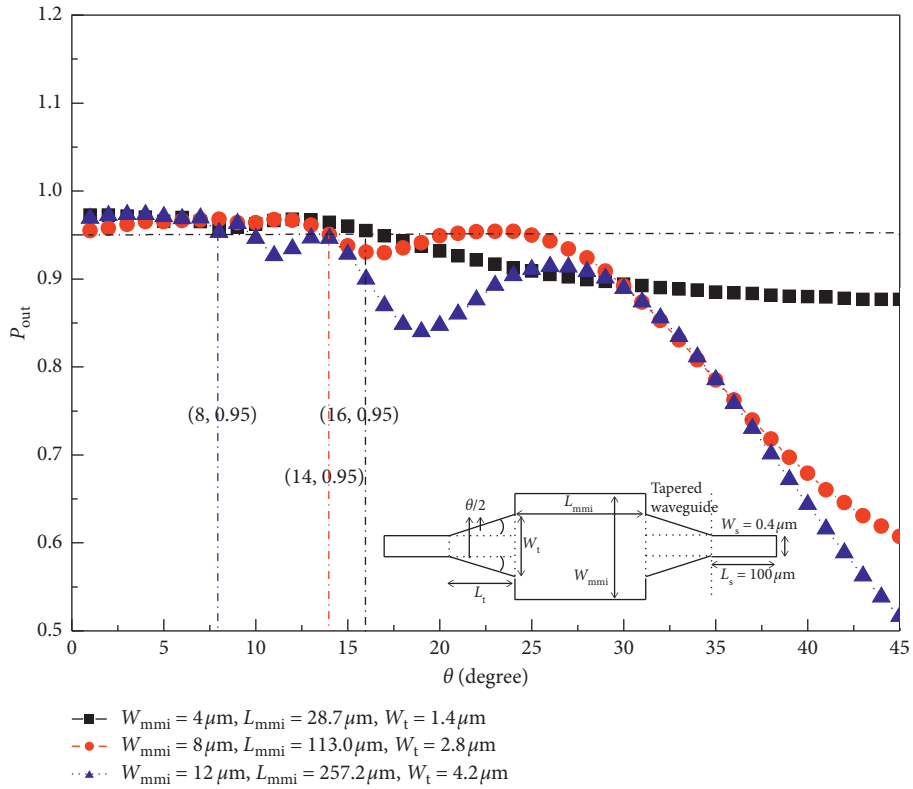

FIGURE 8: When W_t/W_{mmi} is set at 0.35, the 1×1 MMI coupler with $W_{mmi} = 4\,\mu m/8\,\mu m/12\,\mu m$ achieves a minimum width of linear tapered waveguide at $W_t = 1.4\,\mu m/2.8\,\mu m/4.2\,\mu m$, respectively. As the divergence angle θ of a linear tapered waveguide is scanning the range from 1° to 45° at a step of 1°, a maximum divergence angle $\theta = 16°/14°/8°$ is obtained under the constraint of $P_{out} \geq 0.95$, respectively.

$2.8\,\mu m/4.2\,\mu m$, respectively. As the TE_0 mode is transmitted from a single-mode waveguide with a width of $0.4\,\mu m$ into a linear tapered waveguide with a width W_t of $1.4\,\mu m$, TE_0 and TE_1 are excited. The taper width W_t of $2.8\,\mu m$ is excited for TE_0, TE_1, TE_2, TE_3, and TE_4 modes. The taper width W_t of $4.2\,\mu m$ is excited for TE_0, TE_1, TE_2, TE_3, TE_4, TE_5, and TE_6 modes. As the geometric shape of the device is symmetrical structure, the odd modes are suppressed and inexistent.

The single-mode waveguide with width W_s of $0.4\,\mu m$ is combined with the width of the linear tapered waveguide W_t of $1.4\,\mu m/2.8\,\mu m/4.2\,\mu m$, respectively. TE mode component ratio is distributed with the divergence angle of a linear tapered waveguide ranging from 1° to 45°, as shown in Figure 6. When the even modes of TE_2, TE_4, and TE_6 and the odd modes of TE_1, TE_3, TE_5, and TE_7 except TE_0 are suppressed in the linear tapered waveguide, the maximum divergence angle θ of the linear tapered waveguide is 16°/14°/8° with respect to a 1×1 MMI with width W_{mmi} of $4\,\mu m/8\,\mu m/12\,\mu m$. The TE_0 mode component ratio obtains individual 99.13%/98.51%/97.87%. So, this linear tapered waveguide achieves the TE_0 mode adiabatic mode conversion when the TE_0 mode component ratio is at least 97.87% and TE_2 mode and the other modes component ratio is below 2.13%.

For a standard adiabatic mode conversion analysis, a 1×1 MMI in width of $12\,\mu m$ and in length of $257.2\,\mu m$ is combined with the divergence angle $\theta = 1°$ of linear tapered waveguide in width W_t of $4.2\,\mu m$ and in length L_t of $217.7\,\mu m$. When the location of input/output linear tapered waveguide is z/L_t of 0/0.25/0.5/0.75/1, the fundamental mode TE_0 shape of input/output port is simulated to change the mode shape size from smaller to larger mode shape under TE_0 adiabatic mode conversion as shown in Figure 7. The coupling efficiency of this device between the single-mode waveguide and the multimode waveguide is enhanced from 0.41 to 0.95.

The 1×1 MMI with width W_{mmi} of $4\,\mu m/8\,\mu m/12\,\mu m$ is combined with the width of the linear tapered waveguide W_t of $1.4\,\mu m/2.8\,\mu m/4.2\,\mu m$, respectively, as the input and output port with the divergence angle θ of a linear tapered waveguide scanning the range from 1° to 45° at a step of 1°. The maximum divergence angle θ is achieved at 16°/14°/8°, respectively, under the condition of output power of a 1×1 MMI combined with a linear tapered waveguide of at least 0.95, as shown in Figure 8. Figure 9 shows that the spectral responses are insensitivity for the wavelength from 1546 to 1554 nm with the step of 1 nm under the condition of this linear tapered waveguide with a maximum divergence angle θ of 16°/14°/8° combined with the three different widths of a 1×1 MMI of $4\,\mu m/8\,\mu m/12\,\mu m$, respectively. The output power of three different widths of a 1×1 MMI linked with the maximum divergence angle θ of 16°/14°/8° of a linear tapered waveguide is 0.95 when the ratio of W_t/W_{mmi} is equal to 0.35. Three different divergence angles θ of the linear tapered waveguide of 16°/14°/8° with respect to three different widths of a 1×1 MMI width W_{mmi} of $4\,\mu m/8\,\mu m/12\,\mu m$ are taken into equation (4).

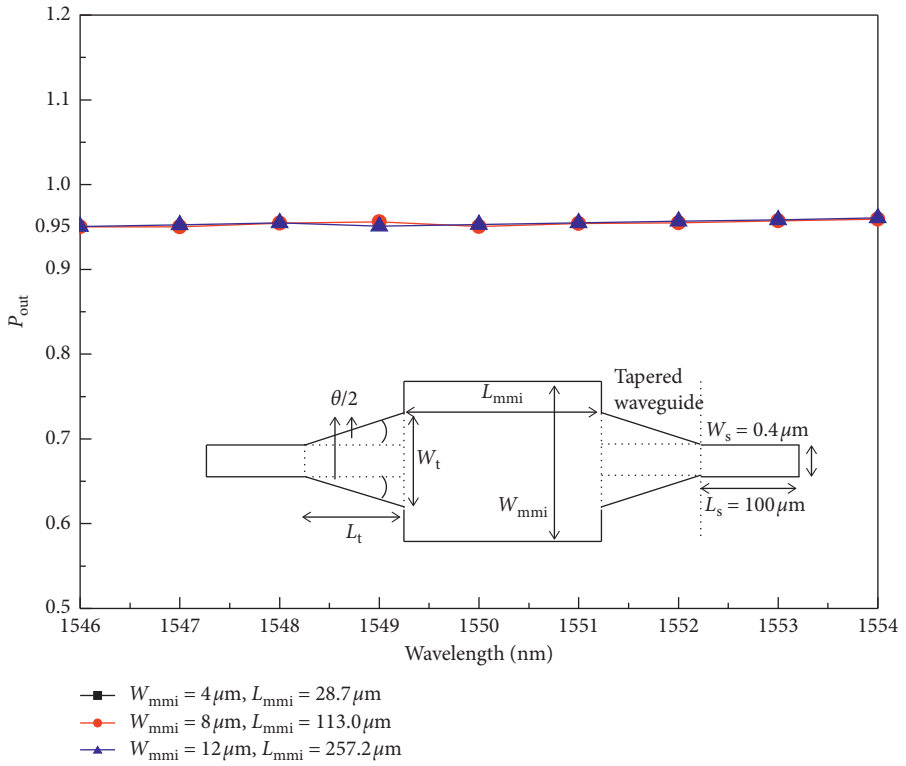

Figure 9: The spectral responses are insensitivity for the wavelength from 1546 to 1554 nm with the step of 1 nm under the condition of this linear tapered waveguide with a maximum divergence angle θ of 16°/14°/8° combined with the three different widths of a 1×1 MMI of 4 μm/8 μm/12 μm, respectively.

Table 1: A basic 1×1 MMI device loss.

W_{mmi} (μm)	L_{mmi} (μm)	Pout (device loss (dB))
4	28.7	0.62(2.08 dB)
8	113.0	0.51(2.92 dB)
12	257.2	0.41(3.87 dB)

The length of a linear tapered waveguide L_t is calculated by 3.6 μm/9.8 μm/27.2 μm, respectively. The ratio of the length of a linear tapered waveguide to the length of a 1×1 MMI is expressed as $L_t/L_{mmi} \geqq 0.086$.

The expressions of equations (5) and (6) are demonstrated under three different widths of a 1×1 MMI coupler combined with a designed linear tapered waveguide:

$$W_t \geq 0.35 W_{mmi}, \tag{5}$$

$$L_t \geq 0.086 L_{mmi}, \tag{6}$$

where W_t is the width of the linear tapered waveguide, L_t is the length of the linear tapered waveguide, and W_{mmi} is the width of a 1×1 MMI and L_{mmi} of the exact imaging length of a 1×1 MMI. When the width of the single-mode waveguide W_s of 0.4 μm and equations (5) and (6) are taken into equation (4), the maximum divergence angle, θ, is expressed as equation (7).

$$\theta \leq 2 \tan^{-1}\left(\frac{0.35 W_{mmi} - W_s}{0.172 L_{mmi}}\right). \tag{7}$$

Comparison of basic 1×1 MMI device loss with a 1×1 MMI combined with a linear tapered waveguide device loss is shown in Tables 1 and 2. When 1×1 MMI with width W_{mmi} of 4 μm/8 μm/12 μm is combined with a maximum divergence angle $\theta = 16°/14°/8°$ in a linear tapered waveguide with a width W_t of 1.4 μm/2.8 μm/4.2 μm and length L_t of 3.6 μm/9.8 μm/27.2 μm, the loss of this linear tapered waveguide is 0.022 dB/0.172 dB/0.158 dB. The length of a maximum divergence angle $\theta = 16°/14°/8°$ in this linear tapered waveguide is reduced to 93.7%/92.9%/87.5% than the length of the divergence angle $\theta = 1°$ combined a 1×1 MMI with width of 4 μm/8 μm/12 μm. The output power of a 1×1 MMI combined with the maximum divergence angle of a linear tapered waveguide is 0.95 (0.22 dB). A 1×1 MMI device loss with a linear tapered waveguide reduces 1.86 dB/2.70 dB/3.65 dB than a 1×1 MMI device loss without a linear

Table 2: A 1 × 1 MMI combined with a linear tapered waveguide device loss.

Pout (Device loss (dB))	W_t (μm)	Max. divergence angle (degree)	Linear tapered waveguide loss (dB)
0.95 (0.22 dB)	1.4	16°	0.022
0.95 (0.22 dB)	2.8	14°	0.172
0.95 (0.22 dB)	4.2	8°	0.158

tapered waveguide. This device loss represents a significant reduction.

4. Conclusion

A 1 × 1 MMI is combined with a symmetrical linear tapered waveguide on an SOI chip. When TE_0 mode from a single-mode waveguide is transmitted to this critical linear tapered waveguide linked with a 1 × 1 MMI, the TE_0 mode component ratio is necessary to be at least 97.87% and the TE_2 mode and the other modes' component ratios are to be below 2.13%. So, the TE_0 mode presents a critical adiabatic mode conversion. The designed linear tapered waveguide is achieved to the shortest length and the maximum divergence angle.

Under the condition of a 1 × 1 MMI coupler combined with the designed linear tapered waveguide, the maximum divergence angle is demonstrated by $\theta \leq 2 \tan^{-1}[(0.35W_{mmi} - W_s)/(0.172 L_{mmi})]$. When the width of a 1 × 1 MMI W_{mmi} is 4 μm/8 μm/12 μm with respect to the length L_{mmi} of 28.7 μm/113.0 μm/257.2 μm, the maximum divergence angle θ is achieved to 16°/14°/8°, respectively.

A 1 × 1 MMI width W_{mmi} of 4 μm/8 μm/12 μm combined with a maximum divergence angle $\theta = 16°/14°/8°$ linear tapered waveguide to a 1 × 1 MMI without linear tapered waveguide. The simulation result shows that the device loss is reduced by 1.86 dB/2.70 dB/3.65 dB, respectively, with respect to an extreme linear tapered waveguide loss of 0.022 dB/0.172 dB/0.158 dB. The length of a maximum divergence angle $\theta = 16°/14°/8°$ linear tapered waveguide is reduced to 93.7%/92.9%/87.5% than the length of the divergence angle $\theta = 1°$ linear tapered waveguide combined with a 1 × 1 MMI with width of 4 μm/8 μm/12 μm. The output power of a 1 × 1 MMI combined with a critical linear tapered waveguide is at least 0.95, which enhanced the coupling efficiency by 1.5 times.

Data Availability

The data used to support the findings of this study are included within the article files.

Conflicts of Interest

The authors declare that they have no conflicts of interest.

Acknowledgments

This work was supported in part by the Ministry of Science and Technology, Taiwan, Republic of China, under the grant no. MOST 108-2221-E-992-080.

References

[1] R. Soref, "The past, present, and future of silicon photonics," *IEEE Journal of Selected Topics in Quantum Electronics*, vol. 12, no. 6, pp. 1678–1687, 2006.

[2] M. Lipson, "Guiding, modulating, and emitting light on silicon-challenges and opportunities," *Journal of Lightwave Technology*, vol. 23, no. 12, pp. 4222–4238, 2005.

[3] K. Kruse and C. T. Middlebrook, "Polymer taper bridge for silicon waveguide to single mode waveguide coupling," *Optics Communications*, vol. 362, pp. 87–95, 2016.

[4] J. Guo and Y. Zhao, "Analysis of mode hybridization in tapered waveguides," *IEEE Photonics Technology Letters*, vol. 27, no. 23, pp. 2441–2444, 2015.

[5] D. J. Thomson, Y. Hu, G. T. Reed, and J.-M. Fedeli, "Low loss MMI couplers for high performance MZI modulators," *IEEE Photonics Technology Letters*, vol. 22, no. 20, pp. 1485–1487, 2010.

[6] Z. Sheng, Z. Zhiqi Wang, C. Chao Qiu et al., "A compact and low-loss MMI coupler fabricated with CMOS technology," *IEEE Photonics Journal*, vol. 4, no. 6, pp. 2272–2277, 2012.

[7] P. Sethi, A. Haldar, and S. K. Selvaraja, "Ultra-compact low-loss broadband waveguide taper in silicon-on-insulator," *Optics Express*, vol. 25, no. 9, pp. 10196–10203, 2017.

[8] Y. Liu, W. Sun, H. Xie et al., "Adiabatic and ultra-compact waveguide tapers based on digital metamaterials," *IEEE Journal of Selected Topics in Quantum Electronics*, vol. 25, no. 3, pp. 1–6, 2018.

[9] J. Zhang, J. Yang, H. Xin, J. Huang, D. Chen, and Z. Zhaojian, "Ultrashort and efficient adiabatic waveguide taper based on thin flat focusing lenses," *Optics Express*, vol. 25, no. 17, pp. 19894–19903, 2017.

[10] Y. Fu, T. Ye, W. Tang, and T. Chu, "Efficient adiabatic silicon-on-insulator waveguide taper," *Photonics Research*, vol. 2, no. 3, pp. A41–A44, 2014.

[11] J. Wang, M. Qi, Y. Xuan et al., "Proposal for fabrication-tolerant SOI polarization splitter-rotator based on cascaded MMI couplers and an assisted bi-level taper," *Optics Express*, vol. 22, no. 23, pp. 27869–27879, 2014.

[12] Y. Zhang, S. Yang, A. E.-J. Lim et al., "A CMOS-compatible, low-loss, and low-crosstalk silicon waveguide crossing," *IEEE Photonics Technology Letters*, vol. 25, no. 5, pp. 422–425, 2013.

[13] D. Dai, Y. Tang, and J. E. Bowers, "Mode conversion in tapered submicron silicon ridge optical waveguides," *Optics Express*, vol. 20, no. 12, pp. 13425–13439, 2012.

[14] L. He, Y. He, A. Pomerene et al., "Ultrathin silicon-on-insulator grating couplers," *IEEE Photonics Technology Letters*, vol. 24, no. 24, pp. 2247–2249, 2012.

[15] C.-H. Chen and C.-H. Chiu, "Taper-integrated multimode-interference based waveguide crossing design," *IEEE Journal of Quantum Electronics*, vol. 46, no. 11, pp. 1656–1661, 2010.

[16] W. Bogaerts, P. Dumon, D. V. Thourhout, and R. Baets, "Low-loss, low-cross-talk crossings for silicon-on-insulator nano-photonic waveguides," *Optics Letters*, vol. 32, no. 19, pp. 2801–2803, 2007.

[17] J. J. Wu, B. R. Shi, and M. Kong, "Exponentially tapered multimode interference couplers," *Chinese Optics Letters*, vol. 4, no. 3, pp. 167–169, 2006.
[18] P. K. Bhattacharya, *Semiconductor Optoelectronic Devices*, Prentice-Hall, Englewood Cliffs, NJ, USA, 1998.
[19] L. B. Soldano and E. C. M. Pennings, "Optical multi-mode interference devices based on self-imaging: principles and applications," *Journal of Lightwave Technology*, vol. 13, no. 4, pp. 615–627, 1995.
[20] M. Bachmann, P. A. Besse, and H. Melchior, "Overlapping-image multimode interference couplers with a reduced number of self-images for uniform and nonuniform power splitting," *Applied Optics*, vol. 34, no. 30, pp. 6898–6910, 1995.
[21] A. S. Sudbo, "Film mode matching: a versatile numerical method for vector mode field calculations in dielectric waveguides," *Pure and Applied Optics: Journal of the European Optical Society Part A*, vol. 2, no. 3, pp. 211–233, 1993.
[22] *Integrated Optics Software FIMMWAVE 5.2*, Photon Design, Oxford, U.K, 2015, http://www.photond.com.